University of London
Imperial College of Science, Technology and Medicine
Department of Physics

Modelling Disordered Foams Using the Vertex Ensemble

Jason M Turner

Submitted in part fulfilment of the requirements for the degree of
Doctor of Philosophy in Engineering of the University of London and
the Diploma of Imperial College, June 1, 1998

Abstract

Foams and emulsions (collectively 'foams') are ubiquitous materials, both technological and commonplace. From the froth on our cappucino to fire-fighting foam, shaving foam to crude oil emulsions — we are almost always interested in the forces which the foam can sustain, or the way in which it will flow, and the way in which the foam absorbs fluid, maintains a level of liquid content, or dries out.

Previous work has largely focussed on either high-powered simulations of small samples of foam, involving considerable computing time, or analytical work on the unit cells of ordered periodic foams, which whilst instructive contain many artefacts caused by the regularity of the system. Recently more effort has been devoted to trying to create simple models of disordered foams to gain a basic understanding of the processes at work.

Foams can be characterized in a variety of different ways — one can regard a foam as a random network of films, as approximated by a random tesselation, a collection of squashed bubbles, or a set of vertices connected together rather sparsely. Then one can attempt to model it with mechanics, statistical mechanics, fluid dynamics, stochastic geometry or topology.

Here we have developed a new model for two-dimensional disordered foams, regarding them as built up from objects we call vertices. These vertices consist of three half-films and their junction. Mechanics tells us that these are the only stable element of this type. We accept that we cannot model the foam completely, and invoke the fairly homogeneous nature of the foam to remove the spatial details and model the foam as a probability distribution over the configuration space of these vertices. We term this model a 'Vertex Ensemble Model' (VEM), as the crucial feature is this use of the vertex distribution. We obtain numerical results for the properties of interest by taking expected values over this distribution.

Now we can model the rheology and osmotic/drainage behaviour of the disordered foam by studying the dynamics of single vertices during the relevant processes. We then use this dynamics to induce a map on the probability distribution. In this way we can calculate the rheological responses of dry and wet 2D foams to various deformations, their osmotic and drainage properties, and also to some extent the interaction between the two. We then attempt to reintroduce some notion of inhomogeneity, to improve our predictions. The predictions compare favourably with both experimental results and foam simulations. We also observe an interesting similarity in the power spectra of some of the predicted properties to those obtained from simulations, which are believed to involve self organized criticality (SOC). This model cannot display 'classical' SOC behaviour, and the source of the spectra is shown to be the fractal nature of the orbits of the map. To the best of our knowledge such a means of 'growing' a fractal, in an explicitly non-recursive manner, has not been demonstrated before. It is also of interest to note how a local map of a strange type duplicates closely behaviour normally associated with long length-scale correlations.

For the most part the solutions of the model have been achieved by numerical integration, as the equations are not easily amenable to analytical solution. However the work on osmotic pressure relied on deriving a whole new set of analytical results for 'semi-ordered' foams, although the final solution is only available numerically.

The model can be used and extended in many ways. One of the most interesting is to use it to study the rheology of three dimensional foams, and the creep behaviour of two dimensional foams. This work has been started and is discussed briefly in the last chapter.

Acknowledgements

First, and most of all, I would like to thank Madhu for all her support and love over the last six years. She has always put up with my habits and moods. I hope she'll continue to do so, and I'd like to wish her the best in her writing up.

I would also like to thank Étienne Hofstetter for putting up with constant pestering on the topics of LaTeXand Mathematica as well as his appetites for Indian food, squash and web-surfing.

I also owe a great debt of gratitude to Pavel Šmilauer for many different things. First for welcoming me to room 919 and encouraging me ceaselessly in my work through discussions, suggestions and honest opinions. He also put up with hundreds of silly questions about C and LaTeXand even how to use an Apple Mac. I am also grateful for his sense of humour, and his habit of creeping up behind me when dozing at my desk. I should also thank Renata and the children for brightening up many a day. I'm also very grateful to Harvey Dobbs for being a great office mate, always ready to chat and full of helpful advice.

My thanks go to Dimitri Vvedensky for taking up an unrequested student and for many discussions and helpful hints, also for his patience with my very slow writing up. I would also like to thank Matthew Foulkes for the interest he showed in my work, distant as it is from his own — and for reading my impractically long 1st year report.

Thanks are also due to Nick Rivier for discussions, for finding me piles of reading matter, and in his rôle as a member of the EC Network on the Physics of Foam (CHRXCT 940542) for enabling me to attend several interesting conferences, also last but not least for the gift of his fridge.

Many thanks also go to Souheil Khaddaj for helping me to get used to AVS and Unix, and for helping me to learn something about systems administration when he was far away. In this light I should also thank Angus MacKinnon for always having an open door, to questions however dumb or irrelevant. I would also like to say a big thankyou to Theresa for all her help, and bearing with me when I was absent-minded. Thanks also to all the other members of 919 and the CMTh group for interesting chats.

I also owe a large debt to Andy Kraynik, who unwittingly convinced me that rheology was the most interesting aspect of foams to study, and whose own work was a constant inspiration.

I would also like to acknowledge the funding I received from the SERC/EPSRC, and their assistance in attending conferences.

Last but not least I would like to thank my parents for their support over many years through ups and downs.

This thesis is dedicated to my parents.

Contents

1 Introduction **1**

1.1 Foams & Emulsions 1

1.2 Motivation 1

1.3 Outline of thesis 3

2 Foam Rheology **5**

2.1 Foams and Emulsions 5

2.1.1 Basic Rheology 6

2.1.2 Applications 7

2.2 Basic Form and Behaviour 9

2.3 Dry 2D Foams 11

2.4 Wet 2D Foams 18

2.5 3D Foams 22

2.6 Foam Coarsening 24

2.7 Foam Rheology 28

2.7.1 Rheological Quantities 28

2.7.2 Experiments 29

2.7.3 Models 33

2.8 Foam Osmotic Pressure 47

2.9 Foam Drainage 51

2.10 Conclusions 53

3 Voronoi Diagrams and Foam **55**

3.1 Voronoi Diagrams 57

3.2 Distribution Functions 58

3.3 Area-Neighbours Distribution 60

4 Vertex Ensemble Model **69**

4.1 Basic motivation 69

4.2 Vertex map 72
4.2.1 Quasistatic Vertex Map 74
4.2.2 Vertex Map with Viscosity 74
4.2.3 Wet Vertex Map 75
4.3 Calculations and Quantities 76

5 2D Foam VEM **77**
5.1 General Comments 77
5.2 Dry Foam under Simple Deformations 77
5.2.1 Simple Shear 77
5.3 Extensional Shear of Dry Foam 81
5.4 Experimental Calculations 84
5.4.1 Rotary Rheometer 85
5.4.2 Oscillatory Shears 86
5.5 Self Organized Criticality 86
5.6 VEM with Viscous Forces 94

6 Osmotic Pressure **99**
6.1 Osmotic Pressure of Ordered Foam 99
6.2 Extended Ordered Foam 100
6.2.1 Two distinct film lengths 101
6.2.2 Three distinct film lengths 118
6.3 VEM for Osmotic Pressure 121
6.4 Stationary State of Drained Foam 123

7 Conclusions **129**
7.1 Conclusions 129
7.1.1 Rheological Behaviour 129
7.1.2 Osmotic Behaviour 131
7.2 Future Work 132
7.2.1 Further Use of the VEM 132
7.2.2 Extending the VEM 133
7.2.3 Using the VEM 133

A Voronoi ID Algorithm **135**
A.1 Algorithms for Voronoi Diagram Generation 136
A.2 Convex Hull Insertion Algorithm 136
A.3 Insertion Deletion Algorithm 138
A.4 Generalisation to n-manifolds 145

B 2D VEM details **147**

B.1 Equilibrium Vertex Configuration 147

B.1.1 Equilibrium Configuration with Viscous Forces 149

B.2 T1 rules 152

B.3 Bulk Stress Tensor Calculations 152

C 3 Equal Films Osmotic Pressure Calculation **155**

D 3 Film Osmotic Pressure Calculations **159**

D.1 Phase I 159

D.2 Phase II 160

D.3 Phase III 161

List of Figures

1.1 Some dry foam 2
1.2 Some wet foam 2

2.1 Basic rheology of foam 7
2.2 Structure of soap film 10
2.3 Local configurations of films 11
2.4 T1 catastrophe 12
2.5 Topology constrains geometry 13
2.6 Pressure difference over film 14
2.7 Topological correlations 16
2.8 Topology → curvature 16
2.9 Too much positive curvature 17
2.10 Cell disappearance 18
2.11 Skeleton and fluid 19
2.12 Geometry unchanged 19
2.13 Wet T1 event 20
2.14 Wet catastrophes 21
2.15 Foam in a container with pressure applied on moving semi-permeable membrane 22
2.16 3D vertex 23
2.17 Simple Shear 29
2.18 Extensional Shear 29
2.19 Results of Prud'homme and Yoshimura — slip correction 31
2.20 Schematic diagram of rotary rheometer 32
2.21 Results of Prud'homme and Yoshimura — phase difference 32
2.22 Results of Prud'homme and Yoshimura — nonlinear responses 33
2.23 Results of Princen — Cells 35
2.24 Results of Princen — Stress vs Strain 35
2.25 Periodic behaviour for $\theta = \pi/6$ under simple shear - stress vs strain 36
2.26 Periodic behaviour for $\theta = \pi/6$ under simple shear - cell motions 37

2.27 Aperiodic behaviour for $\theta = \pi/12$ under simple shear - stress vs strain 37
2.28 Periodic behaviour for $\theta = \pi/12$ under extensional shear - cell motions 38
2.29 Aperiodic behaviour for $\theta = 0$ under extensional shear - stress vs strain 38
2.30 Aperiodic behaviour for $\theta = 0$ under extensional shear - cell motions 38
2.31 Periodic behaviour for wet $\theta = 0$ foam under simple shear 39
2.32 Periodic behaviour for wet $\theta = \pi/6$ foam under simple shear 39
2.33 Periodic behaviour for wet $\theta = \pi/12$ foam under extensional shear 40
2.34 Strain cycling 41
2.35 Stress affecting topology — extensional shear 41
2.36 Stress affecting μ_2 — simple shear 42
2.37 Stress affecting μ_2 — extensional shear 42
2.38 Creep 43
2.39 Elastic shear modulus against $(1 - \Phi)$ 43
2.40 Stress affecting topology — simple shear 44
2.41 Stress-strain relation from vertex simulation 45
2.42 Episodic rearrangements under simple shear 46
2.43 Flow simulation 47
2.44 Various results from Durian's bubble based simulation 48
2.45 Bingham plastic behaviour of yield stress 48
2.46 The osmotic pressure Π^* for an ordered hexagonal foam 49
2.47 The osmotic pressure Π^* for ordered and disordered 2D foams 50
2.48 The osmotic pressure Π^* close to the rigidity loss transition fitted to a quadratic 51
2.49 Experimental study of steady drainage 52

3.1 A Voronoi diagram 56
3.2 Delaunay triangles and sites 56
3.3 Active zones of sites 58
3.4 Plot of ϕ_n against n 60
3.5 Plot of $F(A)\,dA$ and $f_n(A)\,dA$ against A 61
3.6 Regular neighbourhoods 62
3.7 Approximate areas 63
3.8 Initial cell 64
3.9 Cell topology results compared 65
3.10 Irregular cell compared 65
3.11 Cell area results compared 66
3.12 Average cell area vs. topology 67
3.13 Cell area results by topology 67

4.1 Constructing an irregular hexagonal foam from a vertex 70
4.2 Foam sample 70
4.3 A vertex 71
4.4 Full vertex map 72
4.5 Embedded vertex undergoing T1 event 73
4.6 Behaviour under vertex map 74
4.7 Vertex orbit — dry simple shear 75
4.8 Behaviour under viscous vertex map 75

5.1 Calculation for simple shear of dry foam 78
5.2 Vertex hopping under simple shear 80
5.3 Vertices individual stress orbits 81
5.4 Motions of a vertex in a simple shear cascade 81
5.5 Extensional shear prediction 82
5.6 Simulational sample under extensional shear 82
5.7 Zipper structure evolving 83
5.8 Exponential contributions 84
5.9 Small ensemble under extensional shear 85
5.10 Predictions for dry foam in a rotary rheometer 86
5.11 Calculated τ_{xy} for oscillating simple shear 87
5.12 Individual orbits under oscillating simple shear 87
5.13 Scaling power spectrum from ensemble model 90
5.14 Stress orbit for $\theta = 0.9817$ $0 < \gamma < 10$ 91
5.15 Stress orbit for $\theta = 0.9817$ $0 < \gamma < 100$ 91
5.16 Length orbit for $\theta = 0.9817$ 92
5.17 Naive viscous contribution in simple shear 95
5.18 Naive viscous contribution in extensional shear 95
5.19 Total stress against strain rate in simple shear 96
5.20 Viscous term for oscillating simple shear 96
5.21 Different rates of oscillation 97

6.1 Constructing an ordered foam with unit cell 100
6.2 Constructing a symmetric ordered foam 101
6.3 Vertex with fluid 103
6.4 Φ_c against α 104
6.5 Π^* against Φ for $\alpha > 1$ 105
6.6 Π^* against Φ for $\alpha < 1$ 106
6.7 Vertex with one thick film 106

6.8 Definition of the box-cell . . . 107
6.9 Border diagram . . . 108
6.10 Border diagram for foam with small α . . . 108
6.11 Behaviour of foam with $\beta = 1.732$ . . . 110
6.12 Behaviour of foam with $\beta = 1$ . . . 111
6.13 Behaviour of foam with $\beta = 1.01$ . . . 112
6.14 Border diagram for foam with large α . . . 113
6.15 Φ_d against α . . . 114
6.16 Π against Φ for a few $\alpha > 1$ . . . 116
6.17 Vertex with two thick films . . . 116
6.18 Disintegration of two thick film foam . . . 116
6.19 Φ_d against α . . . 117
6.20 Development of a foam with $\alpha < 1$ . . . 118
6.21 Π against Φ for a few $\alpha < 1$ . . . 118
6.22 Constructing a disordered foam with box-cells . . . 119
6.23 Foam at Phase II $\rightarrow$ Phase III . . . 120
6.24 Border diagram for Phase II . . . 121
6.25 Foam in Phase III . . . 122
6.26 Π against Φ for a few $\beta\&\gamma$ . . . 122
6.27 Π for ordered & disordered foams . . . 123
6.28 Fitted tail of Π . . . 123
6.29 z against $\Phi_l(z)$ for regular and irregular foams . . . 125
6.30 $\Phi_l(z)$ against z for a disordered foam . . . 127

A.1 Voronoi diagram of sites in the plane . . . 135
A.2 Convex hull of sites in the plane . . . 137
A.3 Extra sites for torus . . . 139
A.4 Triangulated basic set of sites . . . 140
A.5 Environs of sites 1 & 6 . . . 140
A.6 Remove triangles *abc* and *acd* . . . 141
A.7 An incorrect re-triangulation . . . 142
A.8 Insertion of site 1 . . . 142
A.9 Remove triangles *a1d*, *adf* and *def* . . . 143
A.10 Insertion of site 6 . . . 143
A.11 All inserted . . . 144
A.12 Environs of extra site a . . . 144
A.13 Deletion of extra site a . . . 145
A.14 Triangulation of 'hole' . . . 145

A.15 Finished Delaunay triangulation on torus 146
A.16 Voronoi diagram on torus — from duality 146

B.1 Vertex and cell 147
B.2 Vertex and cell 149
B.3 Viscous flow geometry 149
B.4 Rules for T1 events 152

C.1 Regular hexagonal dry foam 155
C.2 Regular hexagonal foam as fluid fraction increases 156
C.3 Cell corner containing fluid 157
C.4 Border coalescence in hexagonal ordered foam 157

D.1 Ordered foam with three film lengths 159

'Does this path have a heart ? All paths are the same: they lead nowhere. They are paths going through the bush, or into the bush. In my own life I could say that I have traversed long, long paths, but I am not anywhere. My benefactor's question has meaning now. Does this path have a heart ? If it does, the path is good; if it doesn't, it is of no use. Both paths lead nowhere; but one has a heart, the other doesn't.'

don Juan Matus quoted by Carlos Castaneda in 'Teachings of don Juan'

'I do not know what effect my accusers have had upon you, gentlemen, but for my own part I was almost carried away by them; their arguments were so convincing. On the other hand, scarcely a word of what they said was true.'

Plato, 'Apologia'

A student asked Joshu, 'If I haven't anything in my mind, what shall I do ?'
Joshu replied, 'Throw it out.'
'But if I haven't anything, how can I throw it out ?' continued the student.
'Well,' said Joshu, 'then carry it out.'

Zen koan

Chapter 1

Introduction

1.1 Foams & Emulsions

Foams and emulsions are materials where one phase is dispersed in another, and the disperse phase makes up about 90% of the bulk. The essential properties of the two types of material are very closely related and in this thesis we cover both with the term 'foam'. These materials are interesting because they have a complex geometrical and topological structure which largely determines their properties.

1.2 Motivation

The aims of this research are to

- Develop a simple model to describe the structure and behaviour of two-dimensional (2D) disordered foams
- Solve the model by calculation - i.e. numerically or analytically
- Use this model to study
  - The quasistatic rheological properties of dry foam
  - The viscous rheological properties of dry foam
  - The osmotic properties of foam
  - The coarsening of foam
  - The interaction between structure, history and properties
- Compare these predicitions to experiment

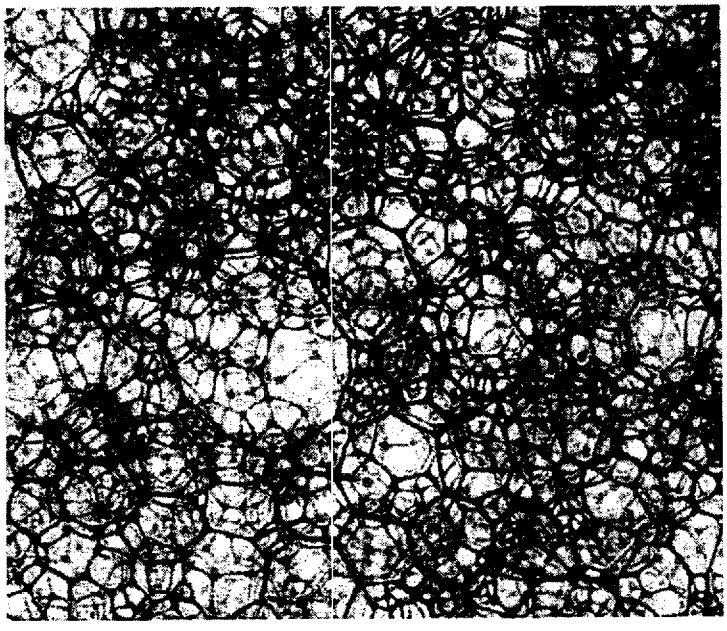

Figure 1.1: Some dry foam

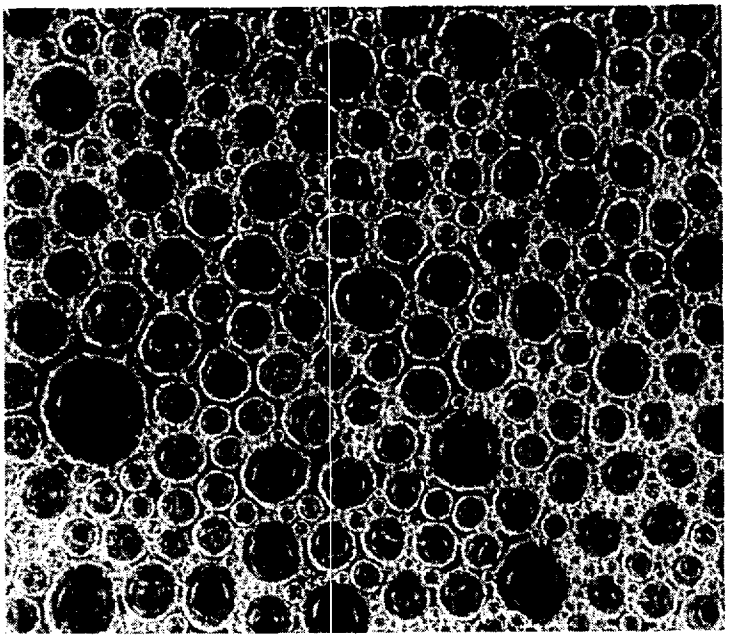

Figure 1.2: Some wet foam

1.3 Outline of thesis

Chapter 2 discusses previous experimental and theoretical work which has been done on the rheometry and rheology of foams. We discuss which properties are experimentally accessible for measurement and what kind of apparatus is used to make the measurements. We also review the previous simulations and theoretical models of foams, to see what areas are still open to question or improvement. Finally brief introductions are given to some concepts we shall use during the rest of the thesis; self-organized criticality, catastrophe theory, and fractal orbits.

Chapter 3 Voronoi diagrams share several structural features with foams, and are thus a good starting point for foam modelling. We first reproduce the work of Mulheran [1] by way of introduction. We then derive some distributions for different parts of Voronoi diagrams. The description of the algorithm used to generate Voronoi diagrams numerically, and comparison to other algorithms, are left to Appendix A.

Chapter 4 gives the motivations and basic arguments supporting the Vertex Ensemble Model (VEM). The details of the dynamics of the various rheological models of single vertices are then discussed. Here we also discuss the features of the map and its orbits which lead to SOC-like spectral behaviour.

Chapter 5 presents the results of the use of the VEM for modelling 2D foams. We discuss these results and go on to apply the model to several interesting situations. We also note the effects of crudely reintroducing inhomogeneity into the problem.

Chapter 6 extends the VEM to calculate various osmotic properties of the 2D foam. We use an argument related to that of Princen [2], the details of which are given in Appendix C. We then need to generalize this argument to derive the dependence of the osmotic pressure on liquid volume fraction for regular foams with unequal film lengths, which we do analytically. The details of these arguments are given in Appendix D. Subsequently we use the VEM to obtain predictions for disordered foams, by averaging over different ordered systems. Then we can numerically examine the effects of stress on osmotic pressure in a similar manner, by changing the averaging distributions for those of stressed foam. We also examine the predictions we can make for the bulk modulus.

Appendix A gives the details on the algorithm used to generate Poisson-Voronoi diagrams on a torus of some general dimension. This algorithm is somewhat novel, but is related to the Convex Hull Insertion Algorithm, and has an expected $\mathcal{O}(\mathcal{N})$ performance.

Appendix B provides some of the background working for the work in Chapter 4.

Appendix C presents the revised argument of Princen [2], adapted to go from dry to wet foam rather than vice-versa.

Appendix D provides the details for some of the analytical work used in Chapter 6 on the osmotic pressure of regular hexagonal foams with three different film lengths.

Chapter 2

Foam Rheology

2.1 Foams and Emulsions

Foams and emulsions are all around us, even inside us, and yet their marvellous structure eludes our notice for the most part, perhaps because of their commonness. The proceedings of a foam conference can read like a summary of the largest industries — foams in food (champagne, beer, coffee, bread, even chocolate), in toiletries (soap, shaving cream, skin), in oil (firefighting, spillage recovery, well-cleaning), emulsions too abound in the chemical trade (paints, greases, oils) and also in food (soup, milk, dressings).

As well as being eminently practical foams have an abstract beauty and interest of their own. In fact much of the original fascination with foams arose from the sense that they were accessible models for a host of other geometrically disordered systems. Foams were first studied seriously in the nineteenth century from two fundamental points of view; one was the question of the ether, the other the structure of living beings. Kelvin was interested in solving the problems associated with Maxwell's laws and the concept of the all-pervading ether — what was required was a material model of space which could support transverse but not longitudinal waves. Kelvin [3, 4] believed that a regular three-dimensional (3D) ethereal foam could explain this feature of electromagnetism. At the same time D'Arcy Thompson [5] was studying foams in connection with his interest in the structure of life-forms, especially their cellular composition. He noted that the structure of foam is the result of competition between a minimization process and both global and local geometrical constraints. He also noticed the similarity with many other 'growth' processes, one famous product of which is the Giants' Causeway [6]. This type of growth in the context of metals was the source of the second incentive to study foam; it was the desire to find a simple system behaving in the same way as coarsening metal grains which led Smith [7] to suggest the concentrated study of foam at a metallurgy conference in Cleveland. John von Neumann was attending the conference in search of materials for use in

his first computer's memory, and immediately derived the well-known von Neumann's law [8]. Despite this foundation much of the behaviour of foams has yet to find a thorough theoretical explanation. Since this time new areas have been linked to foam research, many related to its role as a simple yet troublesome instance of a topological solid [9] (a solid where the disorder is more than a geometrical disruption and is inherent in the very nature of the substance), among which are the theory of glasses [10], differentiation and organization in embryos [11], and cosmology on a supra-galactic scale [12].

It is this interaction of topology and physics which lends foam its true fascination, the physical basis of the substance could hardly be simpler — a collection of thin films which behave quite predictably with surface tension and fluid flow; yet whilst throwing together a large number of these films geometro-topological constraints arrive with the space-filling requirement and give the whole system a range of diverse behaviours. This central rôle of topology makes the study of foam enjoyable but problematic, it seems to bar us from approaching the problem gently via a kind of perturbation theory, because topology is essentially a discrete presence which cannot be added little by little, so that

$$Foam \neq Geometry + \epsilon\, Topology.$$

However we shall see in Chapter 4 that a similar approach is in fact possible, but by using simple elements which embody the topological aspects directly and trying to slowly add the geometrical aspect, so that we can say

$$Foam \simeq Topology + \epsilon\, Geometry.$$

2.1.1 Basic Rheology

Rheology is the study of the flow properties of materials. Here we shall give a brief summary of the rheological properties of foam, from an empirical perspective. Foams combine three distinct elasto-plastic regimes — almost pure elastic, plastic deformation and plastic flow (liquid). We shall see that the existence of these regimes is due to cell motions. For a small stress the foam deforms and resists. On removing the stress the foam 'body' returns to its initial shape. Thus, it is elastic for small stress (the almost comes in because the microstructure will alter for any finite stress). This regime is characterised by an elastic modulus. For a larger stress the foam deforms and resists, but when the stress is released the microstructural changes are too large to allow a return to the previous conformation. This is termed plastic deformation. There is a critical stress termed the 'yield stress' at which the foam is no longer able to resist the stress, but yields and flows. This liquid, or plastic, flow regime is characterised by a viscosity. The left-hand graph in Fig. 2.1 shows these properties schematically.

Naturally these properties depend on the parameters of the foam. There are only three major physical parameters of the foam we can set. These are the bubble size, the disorder of

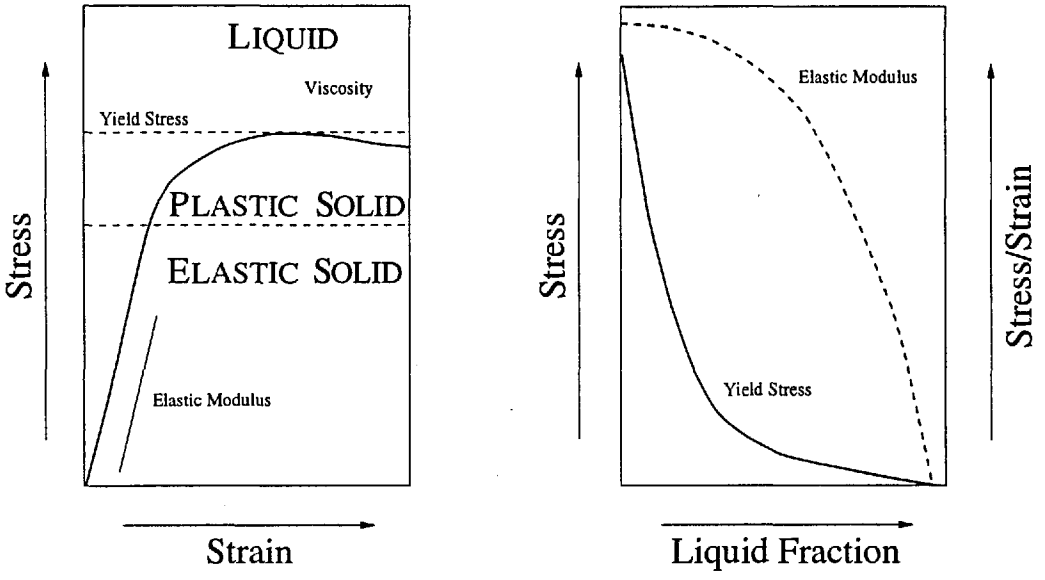

Figure 2.1: Basic rheology of foam

the bubble sizes and arrangement, and the amount of liquid in the foam. In the right-hand graph in Fig. 2.1 is shown the dependence of the yield stress and elastic modulus on the liquid content. The dependence on bubble size is of the form $1/R$ where R is the bubble radius. The dependence on disorder is not yet well established.

2.1.2 Applications

We have already noted that foams and emulsions are replete with applications, but it is of interest to note a few of these technological uses in more detail and to see the questions which they will lead us to ask.

First, we shall look at using foams for containing explosions. To contain an explosion three things are required; a material which can fit itself closely to the explosive, which can maintain its position for some time, and which can absorb large amounts of energy. Foams offer an effective solution to these requirements because

- they can be made on site,
- they are plastic enough to conform to the explosive,
- they can be stiff enough to hold this position,
- the combined process of destroying the foam and evaporating the constituents can absorb a lot of energy,
- they also effectively trap dust and small debris (especially useful for explosives in mining).

However, there are some problems to be solved. For example the wetter the foam the more energy absorbed, and to some extent the more plastic the foam, but at the same time the foam loses stiffness and may not maintain position. Thus this leads us to ask several questions :

- How can a wet foam be made efficiently ?
- How can we stabilise a foam?
- How long does it take the foam to drain and dry out?
- How dry must it be to keep its shape and position?
- On what time-scale does coarsening occur?

The second use we consider is that of oil recovery in oil wells. When oil is first found it is generally under pressure which makes extraction from the reservoir easy. However as the oil is used, the pressure inevitably falls leading to stage where it is insufficient to force the oil out. At this stage there is normally a considerable fraction of the reservoir's total contents remaining underground, so some other means of extraction is necessary. Previously, the solution has been to pump water into the well to push the oil cut. This is not ideal because the resulting mixture of oil and water is not easy to separate and, at the same time, the imiscibility of the two substances means that water is inefficient at moving the oil from the rock. A possible solution is to use foam to push out oil. The advantages are that

- foam can have a substantial yield stress and therefore can push oil out directly,
- foam can be made easily under the correct circumstances, so that it need not be piped to the reservoir as foam, but as separate foamants,
- the mechanism is physical rather than chemical, so that the quantities of surfactants etc, are proportional to the cross-sectional area, rather than the volume, of the oil.

This application leads us to ask several more questions :

- How can a dry foam be made efficiently ?
- How does foam flow through porous media?
- What is the yield stress of some (specific) foam?
- How can we maximise this yield stress?
- How can foam be collapsed efficiently ?

As yet the questions of foam creation have not received much attention from theorists. This is because they presuppose some kind of solution to the questions of the structure and stability

of foam. Likewise the factors affecting the stability of foam have not been given a theoretical basis because they, in turn, presuppose some understanding of the forces which act inside the foam during its history, which is yet to be fully achieved. The state of our understanding of the mechanisms of anti-foamants (foam destabilizing materials) is similar. However, as questions of technological import, these aspects have received a lot of experimental attention, and have been modelled empirically to quite high standards. The study of foam flow in porous media is also in its infancy, [13].

Meanwhile the questions of coarsening, rheology, structure, and drainage have been much more in the limelight, although none of them have been definitively settled. In subsequent sections we will summarize the state of these fields and find that much of the work has concentrated on simulations or highly idealized models. The rest of the thesis will be devoted to developing a simple model which tries to fill some of the gaps and present a clearer picture of foam behaviour.

2.2 Basic Form and Behaviour

Before discussing the behaviour of foam in different circumstances, it is best to fix a picture of a foam in our minds and to choose a vocabulary with which to describe it. We shall call the disperse phase the 'cells' or 'bubbles' of the foam, and will refer to the disperse phase as 'gas' (remembering that emulsions are also covered, where the disperse phase is liquid). The cells are separated by thin films of the continuous phase which we shall also refer to as 'edges' in two dimensions and 'faces' in three dimensions, these terms arising from regarding the foam as a tessellation. We also refer to the continuous phase as the 'liquid phase'. In two dimensions these films meet at 'vertices' which we also term 'Plateau borders'. In three dimensions we use the term Plateau border to refer to both the edges where two faces meet and also the vertices where four edges meet. We shall find that the picture of a foam as a tessellation is important to our work; in this context we call the number of sides of a cell its 'topology', and when referring to the number of films meeting at a vertex we will use the term 'coordination number'. We shall often wish to refer to the local surrounds of a cell or vertex, we shall term this its 'neighbourhood' or 'locality'. Most of the forces acting in the foam will result from surface tension, so that the relevant energy will be the surface free energy, we will interchangeably refer to the total energy, length and area of the foam in this context in both two and three dimensions. Finally we shall occasionally refer to foam as froth for a little variety.

Before continuing it is best to briefly mention the topic of dimensions; the work which has been done on foams to date is split into two distinct halves — two-dimensional (2D) and three-dimensional (3D). Unfortunately this split mostly lines up with the experimental vs theoretical divide, though with some notable exceptions. Experimental work is most effectively

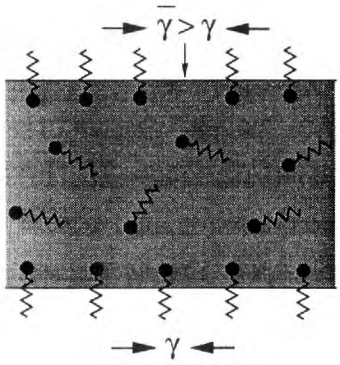

Figure 2.2: Structure of soap film

done in three dimensions where foams are naturally observed. Experiments can be performed on two dimensional foams, by confining a 3D foam between two close plates so that there is only one layer of bubbles in the gap (Hele-Shaw cell), however this confinement restricts the range of experiments possible (for example rheometrics is impossible in 2D) and also introduces such strong perturbations to the foam's behaviour as to cast doubts on the applicability of the theorists' models of 'pure 2D' foam [14]. On the other hand modelling is mostly only achievable in two dimensions for a variety of reasons which will become apparent — in addition to the inevitable (and normal) increase in complexity and computational cost involved in moving to three dimensions, 2D foam is a special case which, due to geometrical chance, simplifies considerably from the general case. As a result we shall be considering two dimensional foams for the most part, but all the while hoping that the basic conclusions will apply to three dimensional foams, which at the present time appears to be justified. For example we know that the dynamics of coarsening 3D foams are more complex to solve than that of 2D foams. However, from a casual observers perspective, the behaviour is very similar.

Perhaps the most common way to speak about foams is as cellular materials. The foams we shall deal with generally have between 90% and 99% gas content by volume, so that the cells are certainly the most visible feature. We fix a particular type of foam in this range by specifying the liquid volume fraction Φ_l or the gas volume fraction $\Phi_g = 1 - \Phi_l$; these are defined by $\Phi_x = V_x/V$ where V_x is the volume of the phase x in the sample and V is the total sample volume.

However, in a sense the majority of the physics going on in foams is in the films which separate the cells; in two dimensions these films are circular arcs and in three dimensions they are bounded surfaces with constant mean curvature. These films have the structure shown in Fig. 2.2, with surfactant molecules sitting on the outside of the film, and a solution of surfactant in the liquid phase inside. The surfactant is necessary to stabilise the foam, which it does by lowering the surface tension and via the Marangoni and Gibbs effects which stabilise the films with respect to stretching and thinning, by causing a small increase in surface

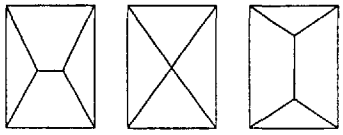

Figure 2.3: Local configurations of films

tension in response to a fluctuation in length. This increase is caused by a minute drop in the concentration of surfactant molecules as the surface stretches, as shown at the top of Fig. 2.2. A pure liquid can form a foam, as water does when falling from a height into a pool, but the films are unstable to any thinning, so that the foam decays instantaneously.

We will subdivide our discussion of the basic properties of foam into three parts, dealing separately with dry, wet and three dimensional foams. In Section 2.3 we will examine carefully the structure and behaviour of dry two dimensional foams. The word 'dry' refers to the fact that there is negligible liquid content $\Phi_l \simeq 0$, so that the films are ideal arcs composed of two surfactant interfaces (a sandwich with no filling). In Section 2.4 we will extend this discussion to cover the additional features of foams with $\Phi_l \geq 0$. Finally, in Section 2.5, we will talk a little about the somewhat more daunting question of three-dimensional foams.

2.3 Dry 2D Foams

The dominant force in any foam, wet, dry, or three-dimensional, is surface tension. This force sets the topological stage of the foam, the local geometry, and drives all other processes. In fact as we saw above this force strives to destroy the foam, and indeed the other forces in the foam can only stave it off, not prevent it — eventually the foam collapses.

Like all systems the foam is stable only whilst in the lowest accessible energy configuration, which in a foam means with the lowest accessible surface area. The accessibility of different states of surface area and structure depends very much on the questions of space-filling and local geometry which we shall consider soon [15]. However the surface tension forces determine the local topology of the foam immediately. Every local neighbourhood of the foam must be stable to small perturbations which implies that centermost configuration in Fig. 2.3 is not admissible. Fig. 2.3 also shows that local minima are quite possible — in fact, they are very common — and indeed crucial to the foam's behaviour. The right-hand configuration is the lowest energy one, the left-hand one is trapped in a higher energy state (we shall see this is closely related to stress).

Thus stability requires that all vertices connect exactly three films, vertices with higher coordination numbers being unstable. We assume that the surface tension in each film in the foam is equal, which is a good approximation, so that therefore the films must meet at common angles of $2\pi/3$ radians. These two observations enable us to solve most of the problems of local

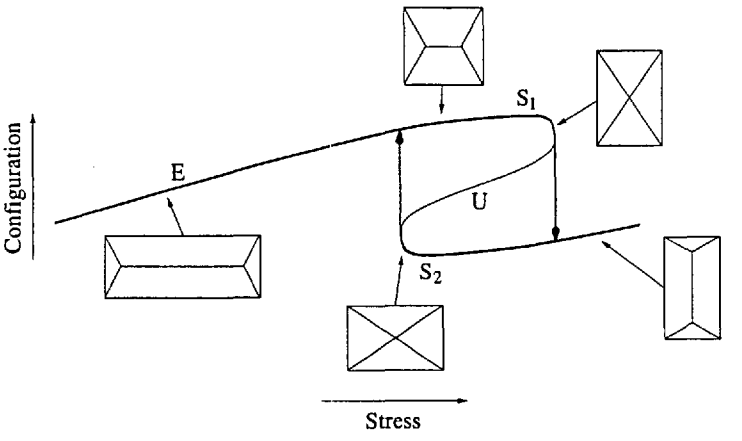

Figure 2.4: T1 catastrophe

foam structure, and even behaviour, but the global properties are less simply derived.

The first implication of these two facts is that if we make the left-most box in Fig. 2.3 taller and thinner then the films inside will be forced towards a configuration like the center box, because they must have two vertices with $2\pi/3$ radian angles. Finally on arriving at the center box's state the system can lose energy (surface area) by switching orientation to the configuration in the right-most box. This switch of orientations is known as the 'T1' event, because it is the most primitive and most important topological event that takes place in the system. The net effect of the T1 is to release stored local stress energy, and it is the ultimate source of the yield stress and plasticity of foam.

The T1 event can be nicely visualised in terms of catastrophe theory, which we will find useful later on in understanding the range of T1 event types and their timing. Catastrophe theory (CT) seeks to understand the origin of discontinuities which occur in generally continuous physical systems. A full description is beyond our scope here, and may be found in Refs. [16, 17, 18, 19] amongst other texts. To describe a system using CT one first seeks a set of variables characterising it, then one splits the variables into two groups, control variables C and state variables S. Here the control variable is stress, and the configuration actually consists of four variables (three lengths and an orientation) which we represent by the single variable configuration. The system is governed by a potential V which is a function of these variables, which in a mechanical system would be the actual potential energy, in an optical system is the path length (much of catastrophe theory was developed to understand caustics) and here is the total film area. The system moves on an 'equilibrium surface' which is determined by the equation $\tilde{d}_S V = 0$, where $\tilde{d}_S$ is the differential with respect to the state variables S. It turns out, see Fig. 2.4 and Fig. 6.18, that for systems with discontinuous behaviour the equilibrium surface has a folded shape (or even more convoluted). This shape leads to a discontinuity, as we adjust the control we take the system along the upper half-sheet (E in Fig. 2.4). However,

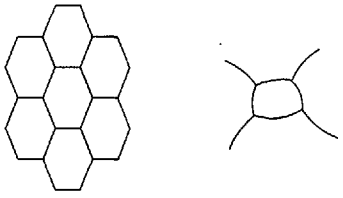

Figure 2.5: Topology constrains geometry

at S_1, the only way the system can obey the control is to jump discontinuously to the lower sheet. Likewise if we move along the lower sheet to S_2. The portion of the equilibrium curve U is unstable and is never reached, by cycling we have a hysteresis effect. The real triumph of catastrophe theory is to classify the elementary catastrophes, of which there are seven, and to prove that all others can be constructed from them. The catastrophe we see here is very similar to the best known of the elementary catastrophes, the cusp catastrophe. We will find this picture useful later on.

The second implication of three-fold vertices is the famous von Neumann's Law, which states that the rate of growth of a cell in a 2D dry foam depends only on the topology of the cell. It is evident (Fig. 2.5) that if all vertex angles are $2\pi/3$ radians then one of two alternatives must hold : either all cells have six sides, so that the internal angles are all $2\pi/3$ radians and the films are all straight, or else the cells have a range of topologies and some films are curved.

Let us consider the second possibility. In this case there are a range of cell topologies in the system, and some films are curved. However, these films must obey Laplace's equation so that there will be a pressure difference ΔP across the films, with (Fig. 2.6)

$$rlP_1 - rlP_2 = \gamma \Rightarrow \Delta P = P_1 - P_2 = \frac{l\gamma}{r} \tag{2.1}$$

where P_1, P_2 are the pressures in the cells, r is the radius of curvature of the film separating them, and γ is the surface tension coefficient. The thin films have a gas permeability κ and thus the pressure difference causes a flow of gas from one cell to its neighbour, which will lead the cells to change size, as the gas is effectively incompressible ($\gamma \simeq 0.1 Nm^{-1}$ is a typical value, so for cells of size more than 0.1mm the pressure differences implied by Eq. 2.1 are of the order of 0.01% of atmospheric pressure and this leads to changes in cell size due to compression of order less than 0.1%). The flow of gas through a film is governed by the Young-Laplace Law

$$dA = -\kappa l \Delta P dt \tag{2.2}$$

where l is the length of the film interface, ΔP is the pressure difference across the interface and dA is the amount of gas (area) transferred in time dt. Thus for some cell the net change of area due to gas flow is

$$\dot{A} = -\kappa\gamma \sum_{s \in S} \frac{l_s}{r_s} = -\kappa\gamma \sum_{s \in S} \theta_s \tag{2.3}$$

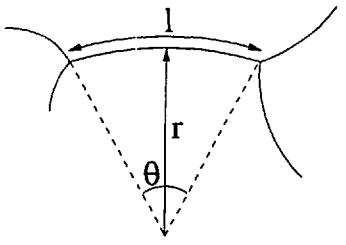

Figure 2.6: Pressure difference over film

where s runs over the set S of all edges of the cell, and l_s, r_s and θ_s are the length, radius of curvature and angle subtended by the film, as illustrated in Fig. 2.6. However, it is evident that the angles θ_s are set by the fact that the vertices have $2\pi/3$ radian angles, and the topology (number of sides) n of the cell, so that

$$\sum_{s\in S}\left(\theta_s + \frac{\pi}{3}\right) = \sum_{s\in S}\theta_s + \frac{n\pi}{3} = 2\pi \tag{2.4}$$

Thus we obtain for the rate of change of area of an n sided cell

$$\dot{A_n} = v(n-6) \tag{2.5}$$

with

$$v = \frac{\kappa\gamma\pi}{3} \tag{2.6}$$

This implies that cells with 6 sides are stable to growth (we shall use the term growth occasionally to cover growth and shrinkage), that cells with 7 and more sides will grow, and that cells with 3, 4 or 5 sides will shrink. It also implies that the rate of growth is directly dependent on the topology; 7 sided cells grow as fast as 5 sided cells shrink, and 3 sided cells shrink three times as fast as 5 sided cells. This link between topology and growth can be extended to apply to any part of the foam. If we define the topological charge of a cell to be $q = 6 - n$ where is n is its topology, then the rate of growth of a cell is, from Eq. 2.5,

$$\dot{A} = -vq \tag{2.7}$$

We can extend the concept of topological charge; the charge of a region is the sum of the charges of its constituent bubbles. Now we find that the rate of growth of a region is proportional to its topological charge. The foam as a whole has a fixed size, so that it neither grows nor shrinks, which implies that the average cell topology $\bar{n} = 6$, or that the foam has zero topological charge.

This is consistent with another topological constraint the foam must obey: Euler's Law. This law states that a polygonal tesselation of a two dimensional manifold must have

$$F - E + V = \chi \tag{2.8}$$

where F, E and V are the total numbers of faces, edges and vertices respectively, and χ is the Euler characteristic of the surface. For a plane χ equals 1, for a torus 0, and for a sphere

2. Now if we use the fact that $F = N$, the number of cells, $E = N\hat{n}/2$ because every edge separates two cells, and $V = N\hat{n}/3$ because every vertex touches 3 cells, we have for a planar foam,

$$N - \frac{N\hat{n}}{2} + \frac{N\hat{n}}{3} = 1 \tag{2.9}$$

so that as we go to the limit of a large foam $\hat{n} \to 6$. Note also that foams on tori, such as those we will use subsequently with toroidal boundary conditions, automatically satisfy the same constraint as a planar (everyday) foam, however small our model system.

Thus we find that the distribution of the topologies of the cells in the foam is the crucial factor in determining the coarsening of the foam, and that there are constraints on the topologies of the cells. Because the distribution is so important to the behaviour of the foam we often characterise the foam by describing the distribution. The mean is already set by Eq. 2.8 so $\hat{n} = 6$. Thus we use the variance μ_2 of the distribution to characterise the state of the foam. As the distribution typically has only one fairly sharp peak, this is generally sufficient. In essence μ_2 specifies the disorder present in the foam, which is the only variable we can control excepting the bubble size. A typical value of μ_2 for a common disordered foam is $\simeq 1.5$.

In fact there are many more constraints than Eq. 2.8 for the whole foam; every convex subset (subgraph) of the foam must obey Euler's Eq. 2.8 for $\chi = 1$. We can get a better understanding of this point by using a mapping between foam tesselations and two dimensional manifolds which has been very useful in the field, and has been set out very well in Ref. [20](for more information in this area Refs. [21, 22, 23] are also useful). Because a foam, regarded as a tesselation, is a 3-valent graph (all vertices three-fold), it is dual to a triangulation. Duality means that we can define a second graph which is in one-to-one correspondence with the first graph. The correspondence here is defined as follows: for each face of graph A (the foam) put a vertex in graph B (the triangulation), and connect these vertices with an edge when the faces had a common edge. A natural consequence is that each vertex of graph A defines a face in graph B. Thus, carrying out this procedure for our 3-valent foam we get a graph whose faces all have three sides, a triangulation. This immediately highlights the rôle of local correlations between cell topologies. Consider the dual triangulation in Fig. 2.7. If we wish to increase the topology of cell A, we must do so by adding another link to node A, which necessitates adding a link to node B. When we have added the extra link the triangulation is no longer planar, which means that this cannot represent a planar foam. To restore the planarity we must remove another link from the system (CD), thus decreasing the topologies of both C and D, so any adjustment of topologies occurs in a correlated manner.

Let us make this argument clearer by introducing the mapping between triangulations and curved two dimensional manifolds. We can define a smooth map h with a parameter α which maps the planar triangulation to a triangulation of another 2D manifold, by changing the length of the edges. When acting on a particular edge $h(\alpha = 0)$ returns the original edge, and

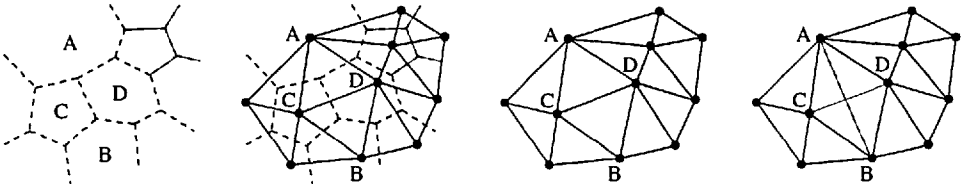

Figure 2.7: Topological correlations

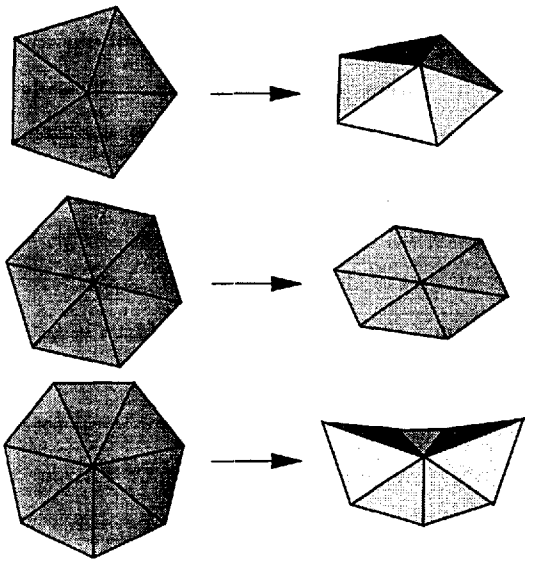

Figure 2.8: Topology → curvature

$h(\alpha = 1)$ returns an edge with unit length. Such a continuous map defined for $0 < \alpha < 1$ defines a homotopy between the the original triangulation $\mathcal{T}$ and a curved 2D (triangulated) manifold $\mathcal{M} = h(1)[\mathcal{T}]$. Under such a homotopy [24] many topological properties are conserved, among which are the genus of the surface, which determines χ, and the lack of self-intersections. Thus we know that the surface $\mathcal{M}$ is of the same genus as the foam and does not intersect itself. We can see that the topology of the original triangulation is transformed into curvature of the surface $\mathcal{M}$ in the manner shown in Fig. 2.8. A more physical picture is provided by imagining that each strut of the triangulation is a piston, thus the homotopy h corresponds to moving the pistons smoothly to a fixed length.

This procedure makes the constraints on the triangulation, or equivalently the foam, apparent, either through our knowledge about curvature fields [20], or through a more direct picture. We can see from Fig. 2.8 that the topological charge q of some cell is related to the curvature about the corresponding node by

$$\int_S R\, da = -\frac{1}{3}\pi q \tag{2.10}$$

where S is the surface composed of the triangles meeting at the node, as shown in Fig. 2.8, and R is the Riemann curvature. Now we know that if the surface is to remain non-self-intersecting

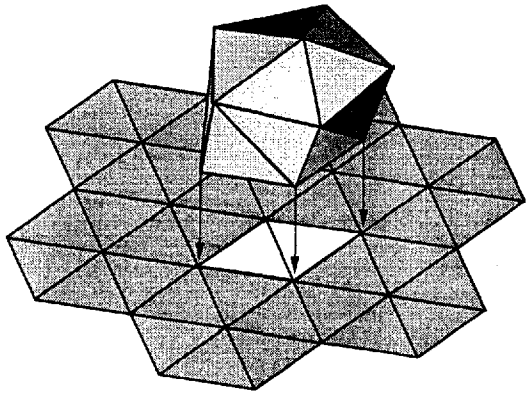

Figure 2.9: Too much positive curvature

the curvature inside a convex contour must be less than 4π, otherwise a spherical bud will detach from the surface, thus $\sum_S q$ can never be in excess of -11 for a convex region S. A piece of surface which is approaching this point is shown in Fig. 2.9.

Thus we see that there must be correlations among the cells in the foam, regardless of any correlations caused by the dynamics or preparation. This makes the exact analytical modelling of foam a difficult task and has yet to be achieved.

Returning to our discussion of the coarsening of the system, we note that after some time has passed cells will begin to reach zero area, and to disappear. The process by which a cell disappears is known as the 'T2' event, and is the second most significant topological event in the foam. The total topological charge of the foam must remain zero, so that these cell disappearance processes must conserve topological charge. Thus these T2 events must redistribute the topological charge associated with the disappearing bubble, so that these processes will have a large effect on the evolution of the cell topology distribution, and thus the way in which the foam coarsens (Eq. 2.5). There are many ways of modelling these T2s, which as Flyvbjerg notes [25], have a great impact on the predictions of the model. There has also been some question as to the fundamental mechanism of the processes. Early work assumed that in the process of shrinking to zero size a bubble would inevitably shed its sides via T1 events until it had only 3, the lowest permissible, so that all T2 events would involve 3 sided cells. Subsequent more careful analysis of the shrinking process [26] has revealed that in certain situations, which are not rare, cells of 4 and 5 sides can also reach zero area without side shedding, so that a whole range of T2 events is possible. A rough portrayal of these T2 events is given in Fig. 2.10, with the right hand side showing the change in the number of sides of the neighbouring cells. It is easy to see that correlations existing in the T2 process will lead to much stronger effects in the topology distribution. For this reason there has been great uncertainty over the years about the asymptotic behaviour of coarsening foam. It is conceivable that correlations in the T2 could lessen μ_2 leading to a foam with most cells 6-sided and stable. Alternatively [27],

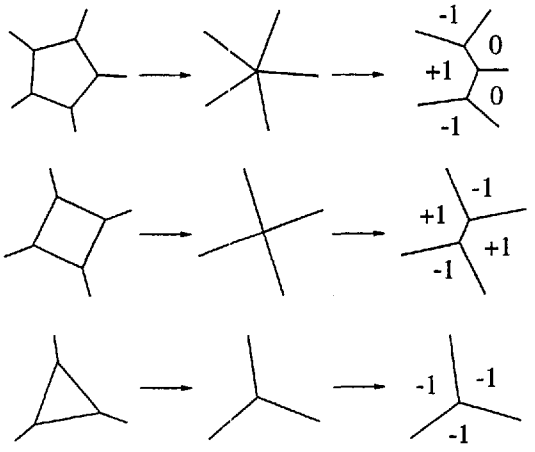

Figure 2.10: Cell disappearance

perhaps the T2s are such that no universal asymptotic state exists, or perhaps the conjecture of Smith [7] is correct and there is a single well defined coarsening asymptotic state.

Now we briefly consider the first possibility mentioned above; if all cells have six sides then all edges will be line segments, all cells will have the same internal pressure, and the configuration will remain fixed, as far as concerns coarsening. We shall call this fortuitous configuration an ordered hexagonal foam, it will be our main tool in understanding disordered foams. This ordered foam is the only one which has thus far been well understood because it has so many pleasing properties. Because of its stability and symmetry we can solve its osmotic and rheological behaviour, though they are not trivial like its coarsening behaviour.

The term 'ordered' is used because the measure of order in the foam distribution of topologies, μ_2, is evidently zero in the hexagonal foam. However, topological disorder is not the only kind of disorder in foam, so we shall need to distinguish different types of hexagonal foam. The first kind we call 'regular'. This is a hexagonal foam with all cells identical regular hexagons, that is a mono-disperse system with all film lengths equal. A second type we shall term 'irregular', with all cells identical, but not regular, hexagons; this system has some films longer than others. A third kind we call 'poly-disperse' this foam has cells which are not identical, some being larger and some smaller (and thus the films are likewise different). It is interesting to note that we can change a regular hexagonal foam to either an irregular or a poly-disperse hexagonal foam by moving vertices around without changing the total length of the films, or the average area of the cells.

2.4 Wet 2D Foams

For the most part wet foams are very similar to dry foams, with a little extra baggage. Thus, we often characterise the wet foam as being a dry foam skeleton (and dual triangulation) with the

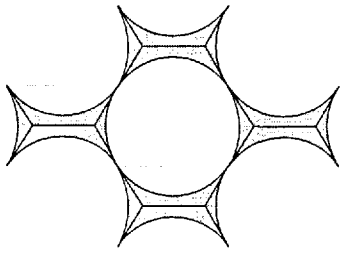

Figure 2.11: Skeleton and fluid

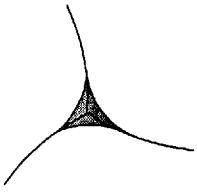

Figure 2.12: Geometry unchanged

fluid 'decorating' it, as shown in Fig. 2.11. This idea has been formalized in the Bolton-Weaire decoration lemma [28], which states that for small fluid content the geometry of a foam is unchanged. This is because the fluid originally accumulates at the vertices, forming triangular Plateau borders like the one shown in Fig. 2.12. This means that for a foam with a small fluid content the behaviour is the same as for a dry foam. In fact, this only holds for a foam with an infinitesimal fluid content, but is a good approximation for a slightly wet foam. When the level of fluid is such that neighbouring Plateau borders begin to touch and coalesce across the short films separating them the lemma breaks down. In this case we have Plateau borders somewhat like those in Fig. 2.11.

The lemma can also break down in a foam with an infinitesimal fluid content, but these break downs have to be manufactured by symmetry. However, these symmetrical structures might arise naturally in slightly wet foams. In recent work Weaire has shown that vertices with coordination number greater than three are stable when there are fluid Plateau borders present. Nevertheless the work has been concerned with experiments and models of vertices and borders formed inside wire frames, with only up to six or seven cells present, so that it seems unlikely that the conclusions will have a big relevance to real foams. In addition to being stable to the small perturbations considered previously a local configuration should also be stable with respect to the background 'temperature' of the foam in order to be a long-lasting feature. That is, if we consider the foam to be a small statistical-mechanical system (using a maximum entropy interpretation of statistical mechanics) the background energy fluxes associated with ongoing events will generate an effective temperature, an availability of stray energies, which any configuration will be bathed in, and must therefore be able to withstand. This implies that highly symmetric localities are likely to be short-lived.

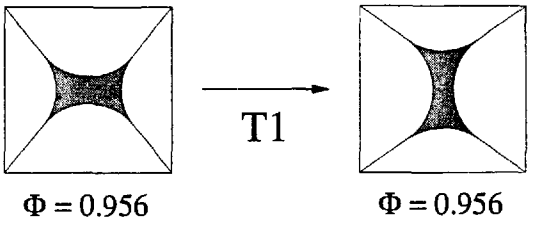

Figure 2.13: Wet T1 event

In the context of wet foams we shall use the term vertex to refer to the vertices of the dry skeleton, and the term Plateau border to refer to the fluid filled vertices of the real foam. As we noted above as the fluid fraction Φ_l increases the Plateau borders can touch and coalesce. In this case we have a foam with some Plateau borders of coordination number greater than three. We can still use the concept of the skeleton, but the geometry is altered. Looking at Fig. 2.11 we see that a highly coordinated Plateau border is effectively one or more connected thick films. The thick films have an effective surface tension which is a function of their thickness (see Appendix B), so the skeleton is no longer a dry foam with all vertex angles being $2\pi/3$ radians. Despite this change of geometry the basic structure of the skeleton, and therefore of the wet foam, is very similar to that of a dry foam. The topology of the foam is almost unaltered, because the skeleton is still trivalent almost everywhere (some higher coordination number vertices are stable but unlikely as mentioned above) and, thus, so are the constraints and correlations related to space-filling.

However, the addition of fluid does have a significant effect on the dynamics of the foam. As the liquid content of a foam is increased it becomes less resistant to stresses, because the cells can more easily slip past each other. The fluid effectively lubricates the movements of the bubbles, the presence of curved Plateau borders lessens the changes of cell shape, and therefore energy, required for motion. It is evident that if the liquid content continues to rise eventually the foam will become a collection of separate bubbles in the fluid phase, and will lose almost all resistance. This is called the rigidity loss transition and we will consider it in Section 2.7. At some intermediate stage, however, the dynamics is still similar to that of the dry foam, with T1 events releasing local stress energy, although the mechanism is somewhat different. Fig. 2.13 shows a stress induced T1 occurring at a vertex-pair with $\Phi = 0.956$, note that the skeleton does not reach the stage where the film length is zero. As the vertex-pair is stressed it reaches a point where it is unstable and it moves rapidly at this stage to a new stable equilibrium. We can use catastrophe theory again to provide a simple picture of the behaviour, as shown in Fig. 2.14.

Now that we are varying liquid content, as well as the strain imposed, we have a true equilibrium surface, rather than the equilibrium curve we had before. At the front edge of the surface (Fig. 2.14) we have the dry foam curve. As we increase the liquid fraction the size of

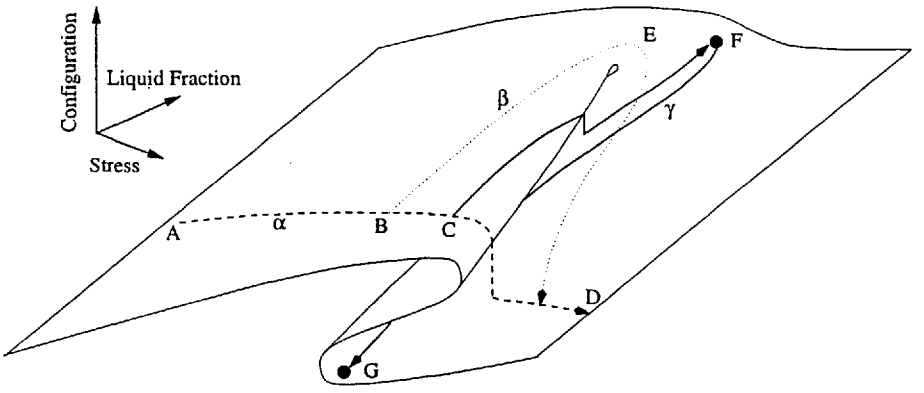

Figure 2.14: Wet catastrophes

the fold decreases, until near E it disappears entirely. This surface is for one vertex only, but if all vertices in the foam are near E then we are close to the rigidity loss transition. A path like $ABCD$ has a T1 event, such as the one in Fig. 2.13,. As we move towards E the size of the jump decreases. It is important to note that the axes are oriented so that the liquid fraction axis is not parallel to the fold 'lip' (the line along which points jump from the upper to the lower part of the sheet). Thus, if we have a vertex at C and we increase the fluid content it undergoes a T1. As the fluid content increases the configuration of the vertex changes, until it can release local stress energy by jumping. It is interesting that by increasing the fluid fraction to take the system to F and then draining the foam back to G along path γ we can relax the local stress. This is a good way to prepare an unstressed foam. By taking path β we can avoid a T1 event entirely by moving around the cusp.

The osmotic pressure of a system is defined as the pressure which must be applied in order to maintain a certain state of phase volume fractions, against the process of osmosis. For example water seeps into dry wood by osmosis, but the application of a sufficient compressive stress can expel the water and maintain some fixed level of water content.

Foams have some interesting osmotic behaviour, consisting as they do of thin liquid films contained by surfactant walls, they can increase or decrease the thickness of the films by absorbing fluid from the continuous phase reservoir. The interesting features lie in the differences between ordered and disordered foams' osmotic pressures, and in the interactions between rheology and osmosis. We have already noted how the level of film thickness, i.e. fluid content, affects the stress-strain relations for foam. Likewise stress affects the structure of the foam and thus changes its other material properties, such as osmotic pressure dependence on liquid volume fraction.

Osmotic pressure Π can be mathematically defined for foams as

$$\Pi = -\left(\frac{\partial F}{\partial V}\right)_{V_g} = -\sigma\left(\frac{\partial A}{\partial V}\right)_{V_g} \tag{2.11}$$

in three dimensions, with F the Helmholtz free energy of the foam, which equals σA, V the

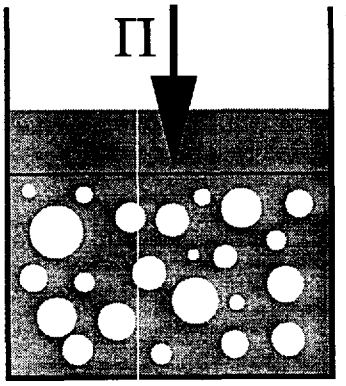

Figure 2.15: Foam in a container with pressure applied on moving semi-permeable membrane

total volume of the sample and V_g the volume of the disperse phase (gas for foams). In two dimensions (which we consider in this model) this becomes

$$\Pi = -\left(\frac{\partial F}{\partial A}\right)_{A_g} = -\sigma\left(\frac{\partial L}{\partial A}\right)_{A_g} \tag{2.12}$$

with $V \to A$ and $V_g \to A_g$. Fig. 2.15 shows the system considered, and the way in which osmotic pressure manifests itself in the wild.

2.5 3D Foams

As was stated above the three dimensional foam has all the problems associated with two dimensional foams, but unfortunately not many of the simplifying features. First of all we consider dry three dimensional foams. We still have convex cells, separated by thin films, but now the films are governed by Laplace's law for a surface

$$\Delta P = P_1 - P_2 = \gamma\left(\frac{1}{r_1} + \frac{1}{r_2}\right) \tag{2.13}$$

where P_1, P_2 are the pressures in the cells, r_1 and r_2 are the two principal curvatures of the film separating them. Thus, the films are now surfaces of constant mean curvature, which unfortunately are not generally portions of a sphere. Three films meet at each edge (line Plateau border), and four edges meet at each vertex (and their corresponding four films) (Fig. 2.16). The vertex angles between meeting edges are now tetrahedral angles of 1.91 radians. Alas, the total 'curvature' of the cell, determined by the curvature of the films and the vertex angles is related to the Gaussian curvature, given by the product of the principal curvatures, whilst the gas flow (Eq. 2.13) is related to the mean curvature, the sum of the principal curvatures. This implies that there is no simple von Neumann's Law in three-dimensional foams.

Indeed the very structure of a 3D foam has only recently been understood. Three-dimensional foams are dual to tetrahedral simplicial complexes, which leads to similar correlations as discussed before, so that the local structure is again well known. However the global structure

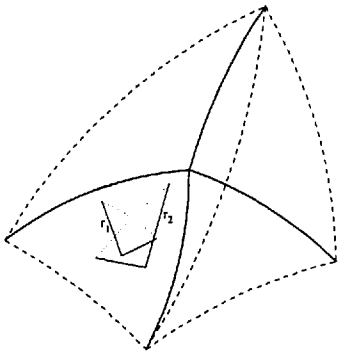

Figure 2.16: 3D vertex

of a disordered foam is always hard to grasp, and there was for a long time uncertainty about the structure of an ordered 3D foam. Kelvin [3] was the first to propose a structure, the tetrakaidecahedral foam. This cell is almost like its polyhedral namesake: the films have zero mean curvature and are slightly curved to give correct vertex angles. This structure was thought to be optimal for almost 100 years, until it was replaced by the Weaire-Phelan cell in 1993 [29]. Recently the structural modelling of 3D foam has been improved by using a minimal surface evolving program of Brakke [30]. This has enabled the modelling of small ($\sim$ 20 cells) disordered systems with periodic boundary conditions.

The dynamics of a 3D foam is also more complex because the family of topological events increases considerably from 2D. Naturally the whole situation is made more difficult by adding fluid to the foam; now in addition to Plateau borders sitting, initially disconnected, at the vertices, we have line Plateau borders along the edges. These have a similar effect on the dynamics as for 2D foams.

The 3D foam adds one very interesting new phenomena for consideration. If we make a wet foam, and allow it to sit (in a gravitational field) the fluid slowly drains out. For example a glass of newly poured lager is mostly froth, which over a couple of minutes drains to fill the glass [31]. This drainage is an interesting and complex phenomena, but is generally explained by the motion of fluid down the line Plateau borders. It is interesting to ask what the rate of drainage is, and the final equilibrium dependence of fluid fraction on height.

Due to the exceptional difficulty of studying 3D foams the general approach is to model 2D foams and hope that they are very similar. Some 3D modelling is done, but for very small systems. On the whole the similarity between two and three-dimensional foams is close, although in some areas it is necessary to model 3D foams directly. The most important are drainage and coarsening where the differing correlations may be significant.

2.6 Foam Coarsening

The first work on foam coarsening was done by Smith [7], when Smith urged metallurgists to take an interest in the mechanics of foam coarsening as a simpler model of the growth of metal grains. In this section we review previous work done on both systems. As the work in this thesis concentrates on rheology, and coarsening behaviour is only related through the problem of creep, we shall not give a detailed background to the work on coarsening to be found in the literature, however a good review is given in Ref. [32]. Coarsening was, as mentioned above, the original spur to studying foam and as such has received much attention. The work done can be split into three main areas — Monte Carlo Potts model simulations which are close to grain growth, simulations concentrating on elements of the foam, and several interesting theories which have been applied to grain growth and foam coarsening. We shall pay most attention to the latter, which go some way to motivating the vertex ensemble model.

The first models we consider are Monte Carlo simulations of coarsening, which are ideally suited to grain growth, where the rates associated with the surface tension dynamics and the diffusion between cells (grains) are identical. This of course limits their applicability to foams. However these models have been used to attack some of the asymptotic properties of the system [33]. The models are based on the use of the high-Q Potts model, similar to the Ising model but with Q instead of 2 states. The energy of the model is intended to give a surface free energy, so the joint energy contribution of two neighbours (the bond energy) is

$$E_{ij} = \sigma\delta_{S(i)S(j)} \tag{2.14}$$

where $S(k)$ is the state of site k. The initial state of the system is a set of cells, or grains, generated randomly, with each cell being composed of sites in one particular state. The system can then be evolved either using the Metropolis algorithm [34] or a more physical activated energy algorithm [35]. A high value of Q is required to avoid the spurious coalescence of cells as they grow (cells of the same state when they contact become one). This factor determines the speed of the simulation; although it can be overcome [35].

The first simulation done which was specific to foam was that of Weaire and Kermode, [36, 37, 38, 39]. This model [40] will be considered in more detail, as it is also used for rheological simulations. The simulation keeps track of two sets of entities, the cells and the vertices. The pressures, topologies and areas of the cells are tracked, and the vertex angles and positions. At each simulation step the areas need to change according to von Neumann's law, and the vertex angles must remain fixed at $2\pi/3$ radians. By writing down equations connecting the pressures, areas, angles and positions one can solve for the new positions and angles in a linear approximation. During each step one must check for the occurrence of cell disappearances and T1 events. The modellers later found that 3, 4 and 5 sided cells can disappear, but in this work, for simplicity, they assumed that cells lost sides as they shrank, so that only three-sided

cells disappeared via T2 events. Physical considerations imply that the foam can not generate 2-sided cells [36] and that any 2-sided cells in the foam disappear very rapidly, so that the simulation proscribes them.(The relative rapidity of cell disappearances is dealt with in [36] and also more generally in [41]. The latter is interesting as it conclusively rules out what had often been an intuitive assumption about the structure of foam, that foams may be fractal in a perfect case. Herdtle and Aref [42] show that while 3-sided cells disappear quickly, 2-sided cells beat them, and fractal inclusions are record-breakers.)

Using this model Weaire and Kermode produced many interesting results, not least because they were the first results in this area. They demonstrated that foams became more disordered as time passed, until they had a $\mu \simeq 1.5$; they produced evidence that Lewis' and Aboav-Weaire's laws held good; and they went on to study some of the elastic properties of the simulated foam which we shall return to below.

There are actually two different but similar ways of doing this kind of simulation. Weaire and Kermode adopted a simple but physically reasonable method, iterating their equation solving through the foam and assuming that the general behaviour would resemble the real system. Herdtle and Aref [42] solved the problem more rigorously by inverting the matrix equation which described the whole system simultaneously; this was aimed to remove any spurious correlations arising from the order in which cells were considered in the Weaire-Kermode model. In fact the results are almost indistinguishable qualitatively, the main difference arising in the way in which μ_2 converges to 1.5, its scaling value. The reason for this is presumed to be the more accurate description of the T1 events, which allows one event to affect bubbles at some distance from those directly involved.

Another approach to modelling the coarsening system is to borrow a method previously used on grain growth. Kawasaki et al. [43, 44] treat the vertices of the foam as the basic element, and simulate the foam's behaviour by defining a dynamics for these vertices. The vertices are free to move, and the films are defined as lines joining vertices, whilst the cells are those polygons formed by the network of lines. The motion of the vertices is governed by

$$\frac{\partial \mathcal{R}}{\partial v_i} + \frac{\partial \mathcal{F}}{\partial r_i} = 0 \tag{2.15}$$

where $\mathcal{R}$ is the dissipation function associated with vertex motion and $\mathcal{F}$ is the interfacial free energy. This method is somewhat unrealistic as it gives a similar rate for the minimisation of energy where vertices are unbalanced due to local deformations to the rate at which gas diffusion causes cells to grow. Nevertheless it provides another topologically correct model of the foam, and this method once again yields similar results to those of Weaire and Kermode, with average area going as t, and similar distributions over area and topology. The advantage of this somewhat simplified dynamic formulation is that it is easily extended to cover rheological behaviour including viscous film effects.

So far, however, the models considered have been simulations. They are interesting because they provide a true 2D foam to compare theory to, and because they show that the topological and geometrical features are the most important. They also make exact repetition of experiments easy, and allow more definitive measurements to be made. They do not though allow sufficient simplification to let us identify the source of various behaviours — they are too close a reproduction of the real system. We need to create a more abstract model to find out which features determine the foam behaviour. A good review covering these types of model is that of Fradkov and Udler [45], here we only introduce a few models which illustrate the important ideas.

The first work on grain coarsening was done by Smith and Herring [7, 46]. They both paid close attention to the exact configuration of the grain boundaries, which restricted their progress. Mullins advanced the study by showing [47] that, due to the curvature driven growth, von Neumann's law effectively held for grain growth, thus supporting Smith's analogy between the two. However, he also tried to use this result to study the boundary shapes accurately.

Simpler models relinquish exact descriptions of large areas of foam structure and opt for probabilistic models of the elements of the foam. The first model of this type was introduced by Burke who, by assuming that the surface tension drove growth (actually in the context of grain growth), developed a simple mean-field model, for a typical grain, which showed that $\overline{r} \sim t^{1/2}$. Subsequently Hillert [48] developed another mean-field model, but by using the distribution of cell areas. This model yielded $\overline{r} \sim t^{1/2}$, but also a form for the grain radius distribution, which unfortunately did not match experiment. Nevertheless the study of the distributions of cells properties had been started. Subsequently Mulheran [49] showed how Hillert's model could be improved by going beyond the mean-field approximation, by including a fitted cell area correlation.

Louat [50] proposed a model for the evolution of the distibution of radii, but by assuming a purely thermal jumping of grain boundaries. Such a model is evidently not well suited to foam modelling, but explains to some extent the lower value of α (in $\overline{r} \sim t^{\alpha}$) than $1/2$. Louat's model predicts a value of $\alpha = 1/4$, and a further development by Mulheran [51] shows how a realistic version of events interpolates between the two models, with $1/4 < \alpha < 1/2$ and closer to $1/2$.

In [52] Mulheran showed that Hillert's model was equivalent to a model based on von Neumann's law and a relative of Lewis' law (using radii); but that such a model is on shaky foundations. He showed that a similar model based on Lewis' law had a firmer footing and predicted the correct form for the area distribution and scaling.

Beenakker [53], suggested another mean-field model of a foam where he split the problem of the coarsening into two parts :

1. What is the relationship between the area and topology of cells in a disordered foam ?

2. How does the distribution of areas behave with time ?

This approach allows him to attack the problem because (2) is already partly answered by von Neumann's law. He tackles the first question by a rather involved argument invoking the correlation between increasing area and increasing topology. The mean-field assumption comes in because local correlations leading to irregular polygonal cells are ignored. Now by minimising the surface free energy he deduces a (peculiar) form for $P(A,n)$ where $P(A,n) = P(A)\delta_{n,n_c(A)}$, so that each topology is uniquely linked with an area range. Having obtained $P(A,n)$ he can use von Neumann's law to get the time behaviour of $P(A)$ numerically. This approach made a great contribution by showing how the system could be modelled, but itself has rather strange and unphysical behaviour. The foam described by this model periodically becomes more disordered and then suffers a catastrophic reordering, with the distribution $P(n)$ broadening and then collapsing to a delta function. At the time this result did not seem inconceivable because Aboav had recently tried to reproduce the experiments of Smith with insufficiently equilibriated foams and had found that right to the end of his measurements μ_2 was increasing without limit, rather than tending to a scaling limit as reported by Smith. Beenakker assumed that Aboav might be seeing the initial broadening of the distribution.

When new experimental results became available which vindicated Smith's first reports, a new model was required to explain the behaviour of μ_2. Marder [54] proposed a more simplistic approach to the distributions. He showed that local correlations prevent the cells from so easily assuming the lowest possible energy configuration (regular polygonal), and suggested an approach based solely on time evolution. The idea was that von Neumann's law gives the behaviour of $P(A,n,t)$,

$$\partial_t P(A,n,t) = -\kappa \partial_A (n-6) P(A,n,t) \tag{2.16}$$

All that is required is to supplement this equation with a description of the rates at which cells gain and lose sides. The experiments had already shown that isolated T1 events were of minute relevance, so that only cell disappearance ($A \to 0$) caused topology changes. Marder knew how many sides must be gained and lost with each type of T2 (Fig. 2.10) and assumed that the cells losing would be the smallest neighbours, whilst the cells gaining (five sided T2) would be the largest. This enabled him to close the equations and to solve them numerically. The results were in good agreement with the simulations of Weaire and Kermode with $\overline{A} \sim t$, and close to the experiments of Glazier et al. which gave a $\overline{A} \sim t^{0.6}$ due to small system size.

The next model proposed was an abstract simulation of Beenakker's [55], which was the first non mean-field model. He used von Neumann's law to get the growth of cells, and the rules set out by Marder (Fig. 2.10) for topology changes. However rather than apply them to a distribution in the form of a differential equation he used them to define a dynamics for a large collection of abstract cells. Thus each cell had an area, a topology and a set of neighbours. The area varies with time according to Eq. 2.16. If a cell area reaches zero then it disappears and

the topologies and neighbourhood information of its neighbours must be altered. Beenakker did this by choosing the affected neighbours at random from the set of neighbours. He solved the resulting model numerically, and achieved some interesting results. The model gave very similar predictions to Marder's with respect to the scaling state of coarsening foam. However it was also able to corroborate the experimental evidence leading to the Aboav-Weaire law.

The final model we consider here is that of Flyvbjerg [25]; another mean-field model of coarsening. Flybjerg also set out to derive a master equation for the distribution, in a very similar way to Marder. However he included the rules for T2 events in a different manner. Rather than use the size of neighbours to determine which would gain/lose sides he chose to use the topology. Of course Lewis' law tells us that they are closely related. The assumption was that any side in the foam had an equal probability of being the side which was gained or lost, thus the probability of a cell being affected was proportional to its number of sides. Once again the model was solved numerically and the results were in close agreement with Marder's.

2.7 Foam Rheology

We shall now discuss the previous work which has been done on foam rheology. Because of the technical interest of foams there is a considerable body of work of which we shall mention only a small fraction, those parts directly relevant to our work. A valuable review article on foam rheology is that of Weaire and Fortes [56].

However first we need to clarify the parameters and values which are used to quantify rheological behaviour.

2.7.1 Rheological Quantities

We shall expand only on those quantities which we study in this thesis, and only briefly, as these quantities are generally appreciated. These are primarily the yield stress, the viscosity and the several components of the stress tensor.

The stress tensor summarises the forces in a body, so that the components give the forces acting across unit areas perpendicular to the chosen coordinate axes. Thus full knowledge of the tensor implies full knowledge of the stress in the sample. For this reason we are generally interested in calculating the stress tensor. While the magnitude of the various components is a matter of calculation, often symmetry principles determine symmetries in the matrix and often zeroes in the matrix. This arises from the way in which infinitesimal deformations are acted on by the stress tensor to determine the total energy change of the foam. This term determines the physically relevant combinations of components. We will not look at the basis of such arguments further here [57], but the upshot is that we are interested in certain combinations of stress tensor components in different situations. We often know these are the only significant

Figure 2.17: Simple Shear

Figure 2.18: Extensional Shear

non-zero quantities. In this thesis we consider chiefly extensional and simple shears; both are constant area affine deformations.

Simple shear is well known simply as shear (Fig. 2.17). In this situation symmetry leads us to be interested only in the off-diagonal element of the stress tensor σ_{xy}, which symmetry again implies is equal to σ_{yx}.

Extensional shear is less well-known, and is illustrated in Fig. 2.18. In this situation the symmetry implies that the interesting quantities are the first and second normal stress differences $N_1 = \sigma_{xx} - \sigma_{yy}$ and $N_2 = \sigma_{xx} - \sigma_{zz}$ as the component σ_{xy} is zero.

All the quantities we are interested in can be obtained from the stress tensor. We are interested in the dependence of the important stress functions S (one of σ_{xy},N_1,N_2) on the strain. We are also interested in the yield stress of the foam sample, the stress at which the sample begins to fail and flow plastically. This failure point is however not well defined so that there are three popular choices:

1. S_y, which is the value of S when the sample first starts to flow plastically.

2. $S_{y,\max}$, which is the maximum value of S during a strain run.

3. $\langle S_y \rangle$, the expected value of S averaged over the plastic flow regime during the strain run.

Here, S represents the important stress function, normally σ_{xy} or N_1. Generally all three give similar, but not identical values. We shall show values of all three in our work.

The viscosity η may also be extracted from the stress tensor. It is the important stress function divided by the rate of strain γ. Because viscosity is only defined in the plastic flow regime it is subject to the same haziness as S_y.

2.7.2 Experiments

Whilst work on foam structure and coarsening has been in progress for almost a century, studies of foam rheology have only been undertaken in the last few decades. This work is split into two eras. The first era, in the 1960s and 1970s, was more effective at highlighting the interesting properties of foams and at uncovering the difficulties of measurements than at giving clean

confident results. The second era, from 1980 to the present day, has seen a resurgence of interest, with a lot more success.

We shall give a brief review of the first era, without going into details. One of the first researchers to study the rheology of large gas fraction foams was David [58, 59]. He used a capillary viscometer, and he found that wall slippage was a considerable problem. He corrected using Mooney's [60] method, and found foam to be shear thinning. Similar experiments were conducted by Wenzel et al. [61], and Patton et al. [62]. Patton and David both found that viscosity μ was proportional to the tube diameter, whilst Wenzel et al. noted some unquantified connection. Patton found that his results were also dependent on tube length, which would appear to suggest only partially developed flow in the apparatus. Wenzel continued with an experiment in the cone and plane geometry [63], which also indicated shear thinning behaviour. However all these experiments are open to question, as the bubble diameter was always of the same order as the apparatus. With regard to the correlation between gas volume fraction Φ and μ, Wenzel and David found no evidence for any connection, while Boyer et al. [64] found μ to increase with Φ. More contradictions arose in the study of the link between bubble size d and μ. Wenzel found in his cone and plate experiments that μ was independent of d, while in his tube experiments he found $\mu \simeq 1/d$. David observed a connection between μ and d but without a specific form.

All these studies indicated the existence of a yield stress τ_y, but only Wenzel and David attempted to measure it. Wenzel arrived at a value for τ_y by fitting his data to a Herschel-Bulkley model. He found $\tau_y \propto d^{-0.65}$, and found no correlation between τ_y and Φ. David, however, found $\tau_y \propto \Phi$. Boyer et al. did some indirect studies of yield stress by observing the particle lifting ability of rising foam, and found that τ_y increased with Φ.

Now we move on to the recent work, which has been more successful. Here we shall go into more detail. It is useful for the theorist to appreciate how experiments work, never more so than in a field where concrete predictions are the ultimate goal. Research into foam rheology continued with the work of Princen and Prud'homme. Both had developed similar simple models of foam rheology and carried out experiments to check their predictions. Princen's experiments used a Couette device with a rotating outer cylinder and with the torque being measured on the inner cylinder. His aim was to study both wall slip and yield stress. By using a model of the slip layer [65] similar to Mooney's [60] he was able to obtain the yield stress τ_y indirectly.

Prud'homme and Yoshimura [66] also developed a slip layer model similar to Mooney's [60], and were able to use it to get the viscosity directly. Their analyses showed that by running the same experiments twice at the same stress using viscometers of two different sizes (cylinders and plates with two separations, capillaries with two radii) the slip effect could be eliminated.

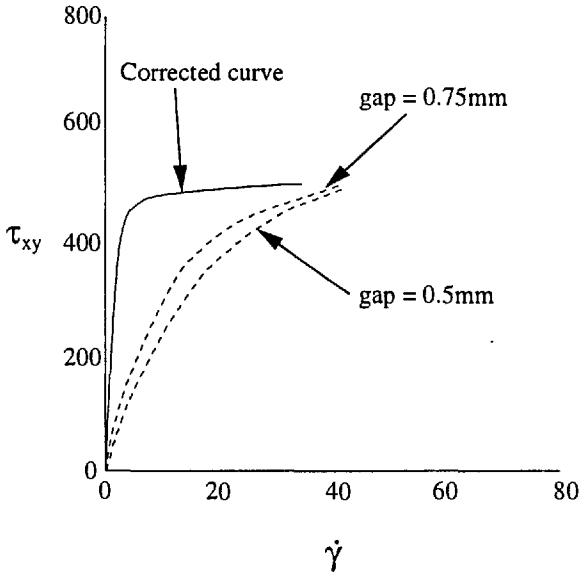

Figure 2.19: Results of Prud'homme and Yoshimura — slip correction

Thus in a parallel plate device (such as theirs) the true bulk shear rate $\dot{\gamma}$ is given by

$$\dot{\gamma} = \frac{\dot{\gamma}_2 h_2 - \dot{\gamma}_1 h_1}{h_2 - h_1} \tag{2.17}$$

where h_i and $\dot{\gamma}_i$ are the plate separation and apparent shear rate in each case. The viscosity can thus be obtained using the Rabinowitz correction. A plot of two experimental results and the corrected curve is shown in Fig. 2.19.

Subsequently Prud'homme and Yoshimura [67] measured the yield stress directly using a Couette device with eight-vanes on the inner cylinder with a stress rheometer. The rheometer applies a constant torque on the inner cylinder and monitors its position. The shear stress at the outer cylinder is known from the torque, and the lowest stress at which the vanes change position continuously is taken to be the yield stress. The last experiment done by Prud'homme and Yoshimura involved large strain oscillations and will be considered below.

Kraynik was another who worked both on a simple model and with experiments. He used a capillary viscometer to measure the viscosity of foam, eliminating cell size effects by using a capillary with diameter $\sim$ 1 inch. He also developed a new means of measuring the yield stress using this capillary tube. This method involves injecting as large bubble into the foam. From the relative motion of edge cells and the bubble the yield point can be deduced and the yield stress measured.

Finally we summarise the experimental results upon which we relied during this work. The most important part of the experimental work done on foams, as far as concerns us, is that done by Khan and Armstrong at MIT. This is because Khan's PhD thesis was available to the author, and contained detailed results. Khan and Armstrong did both experimental and theoretical work on foam rheology. Their experimental work involved the use of a rotary rheometer, a

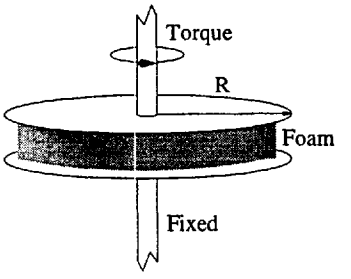

Figure 2.20: Schematic diagram of rotary rheometer

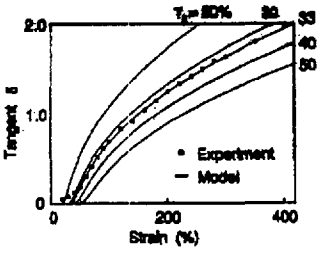

Figure 2.21: Results of Prud'homme and Yoshimura — phase difference

schematic diagram of which is shown in Fig. 2.20.

Without going into to details we briefly explain the setup of the rotary rheometer. The apparatus consists of two parallel disks of radius R a small distance apart. One of the disks is fixed and the other rotates relative to their common axis. The rotating disk is attached to a sensitive torque generator, and its position is carefully measured. The cavity is filled with the rheological material. By rotating the disk the sample is deformed. As the disk is rotated it is evident that material in a cylinder defined by a certain radius r is under simple shear to a good approximation. The magnitude of the shear depends on the radius we consider; at $r = 0$ the shear is always zero, at the rim the shear is termed the 'rim shear' γ_R. Between the rim and the centre the shear varies linearly with radius,

$$\gamma(r) = \gamma_R \left(\frac{r}{R}\right) \tag{2.18}$$

The torque on the moving disk is the integral of the stress acting from each sheared cylinder. The rim is evidently at the highest shear, when it reaches the yield strain of the material a yield surface is defined. This surface is a cylinder which separates the material which has yielded from that which has not. It is evident that such a surface is not truly defined and that the situation is more complex, however measurements using the rotary rheometer are useful as it has such a simple flow pattern and is easy to analyse.

The second body of experimental data used intensively in this thesis is that in Prud'homme and Yoshimura [66]. They used a rotary rheometer with fritted glass disks to avoid slippage. The sample was an oil-in-water emulsion with $\Phi = 0.92$ and the mean cell diameter $D = 17\mu m$. They applied sinusoidal strains of varying amplitude and frequency, with the upper amplitudes

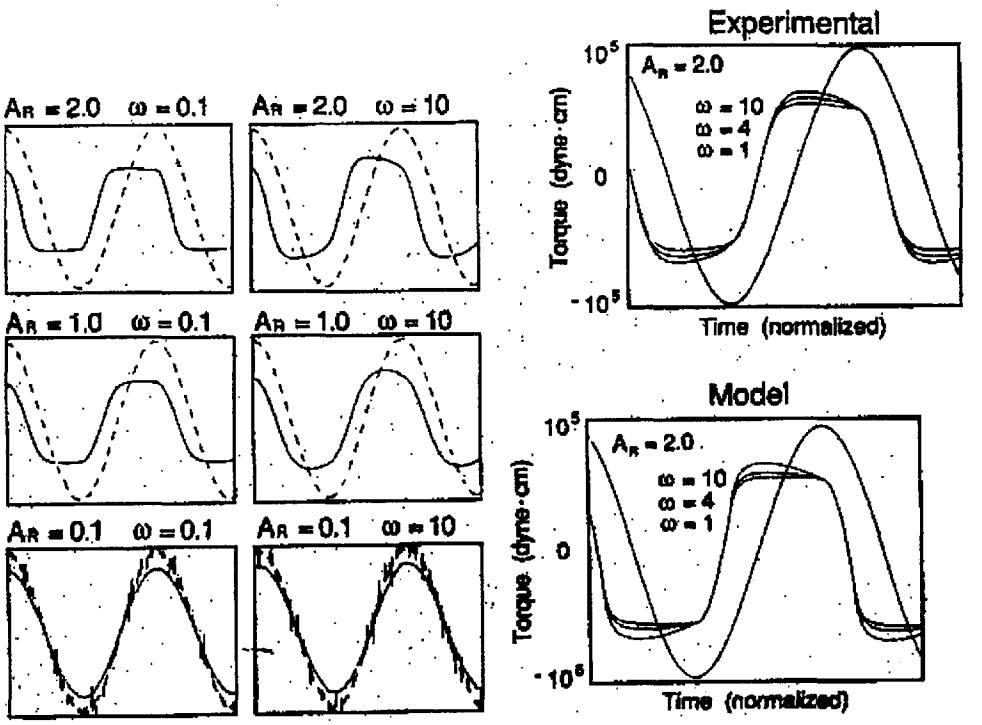

Figure 2.22: Results of Prud'homme and Yoshimura — nonlinear responses

chosen to go beyond the emulsion's yield stress. The result is a series of non-linear response curves. The response curves are shown in Fig. 2.22. The phase between deformation and response was also recorded and is shown in Fig. 2.21. They compared predictions from an empirical generalised Bingham fluid model, and found exceptionally good agreement.

2.7.3 Models

2 Dimensions

The first model used to explain the rheology of foam was that of Derjaguin [68], which shares more or less the same assumptions as Ref. [69]. The model took the collection of many films placed at differing orientations to be the most important feature of the foam, and was designed only to model the initial linear elastic regime. The model therefore contained a distribution over film orientations, which was assumed to be uniform, and each film was supposed to extend throughout the sample of foam. Then deformations would be applied to the sample volume, and felt affinely by the films. The total surface energy of the deforming films can be calculated simply and then used to develop the constitutive equation for the foam. The model of Stamenovic and Wilson [69] is quite successful, yielding the prediction for G the shear modulus

$$G = \frac{\gamma S}{6V} \tag{2.19}$$

for a dry 3D foam, where S and V are the surface area and volume of an average cell (throughout we shall use γ to denote the film surface tension). This agrees well with early results from 3D simulation work [70]. The model of Derjaguin gave a similar expression, but his assumption of affine motion makes the expression an over-estimate by approximately 60%.

This is a good point to introduce some other simple models which have been used. Perhaps the most simple possible was that due to Kelvin [4] which used the idea that the longitudinal modulus of a foam is zero [56], and the isotropy of elastic moduli (see Ref. [71] for details). For both two and three dimensional ordered foams the symmetries of the structures restrict the shear modulus to be isotropic. If the longitudinal modulus L and shear modulus G are isotropic then the material must be isotropic, and this implies that there are only two independent moduli (only two terms in the second order expansion of the energy) which are the bulk modulus K and the shear modulus G. This implies a relation between K and G if $L = 0$, which is

$$K + \frac{4}{3}G = 0 \tag{2.20}$$

in three dimensions. The bulk modulus is easily obtained as

$$K = -\frac{2\sigma S}{9V} \tag{2.21}$$

which leads us to the same expression for G as Eq. 2.19.

Edwards and Pithia [72], Section 2.6, have extended their Boltzmann equation model to deal with the behaviour of flowing foams. They build upon their modelling of the distribution of cell topologies by adding a distribution of film lengths and orientations. They find that they can eventually make a prediction for the foam viscosity, by dropping the topology dependence and constructing a Fokker-Planck equation. They assume independence of neighbouring films, and obtain

$$\eta_f \sim \eta_l \Phi^{-1/2} \tag{2.22}$$

Such a result is interesting, but it appears that it will be difficult to make more specific predictions about the stress-strain relation using this approach.

Princen and Prud'homme adopted an entirely different approach, and one which has almost defined work on foam structure and rheology, in a body of work [73, 74, 2, 75]. Their idea was to model the regular hexagonal foam, which can be done analytically due to its simpler structure, and to thus estimate the behaviour of disordered foams. We shall discuss this work at some length as it is the foundation of the work in this thesis, another good review can be found in Ref. [76].

Princen was interested in many different factors affecting foams; contact angles [74, 77] and finite thickness of films [75] amongst others, and wished to predict the osmotic pressure [2] and shear modulus [73] Prud'homme was likewise interested in the rheology of foam [78]. He calculated these two quantities for one specific orientation of the regular hexagonal foam, with

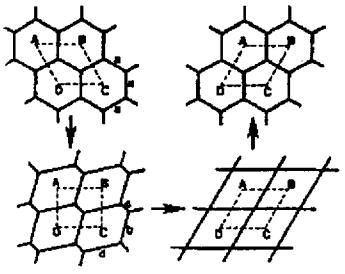

Figure 2.23: Results of Princen — Cells

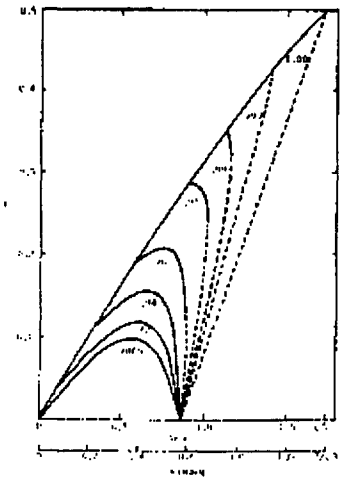

Figure 2.24: Results of Princen — Stress vs Strain

one film parallel to the shear direction. Because one is dealing with a spatially periodic structure one knows by symmetry that the cell centres and therefore the film mid-points must move affinely (a unit cell shares the same deformation as the whole sample) with the deformation. By using this fact, and the rules shown above (Section 2.3) for equilibrium configurations, Princen was able to determine the structure up to the first T1 event, for this single orientation, for all liquid fractions. From the structure it is easy to calculate the energy of the foam, which is just the total film length, and thus the stress tensor (or some components thereof). As shown in Fig. 2.23 in a regular hexagonal foam every unit cell undergoes T1 simultaneously, thus the stress-strain relation has discontinuities at the points at which T1 events occur, as shown in Fig. 2.24. The model was restricted to the first continuous segment of evolution because some new method is necessary to determine the configuration immediately after the T1, at the start of the next continuous segment. As noted above (Section 2.3), the size of the discontinuity diminishes as the liquid content increases, and disappears at some point.

Khan and Armstrong [57] extended this theory to cover all orientations of dry foam up to the first T1. They found that the elastic modulus of the foam is independent of the orientation for both extensional and simple shears, which must be so, but also that the non-linear behaviour is also independent of orientation. This means that the foam has the same behaviour up to the T1,

Figure 2.25: Periodic behaviour for $\theta = \pi/6$ under simple shear - stress vs strain

regardless of orientation, but the strain at which the T1 occurs does depend on the orientation. They denoted the orientation of the ordered hexagonal foam by the angle of rotation θ from Princen's original orientation (one film parallel to the shear axis). They noted that a foam with $\theta = 0$ jumps back to its original orientation at the first T1, so that its stress-strain relation will be periodic. In this way they made the first prediction for foam flow, by incorporating a simple expression for the film viscosity in their model.

This model was simplified by Weaire [79], who proves the isotropy of the stress-strain relation, even in the non-linear regime, for a dry foam. Weaire shows that for a regular hexagonal foam the energy is a quadratic function of $\sin\theta$ and $\cos\theta$ which implies that it must be isotropic by a well-known theorem of tensor algebra [80]. This in turn demonstrates that the stress-strain relation must be independent of orientation, up to the first T1.

The next step was taken by Kraynik and Hansen [81] who found a method to determine the orientation after a T1 event, for a foam of arbitrary initial orientation. In this way they can calculate the entire history of a sample of ordered foam under simple shear and extensional shear. The method they use to determine the orientation is simple, and will be explained in Chapter 4 where we use a similar method, and comes from inspection of the unit cell. During a T1 event, as we saw in Section 2.3, the foam jumps from a high energy state to one of lower energy, relaxing local stress energy. This implies that the film which reaches zero length is perpendicular to the local strain axis and that the new film is parallel to it. Thus by inspecting the unit cell just before the T1 we can see how to define a new unit cell (Fig. 2.23).

This method uncovered a wonderful collection of details hiding in the mechanics of regular hexagonal foam. We will term the path traced in configuration space by a regular ordered foam as strain varies its 'orbit', and we will also use the term X-orbit to refer to the projection of this orbit onto another space X, both these orbits thus being parametrized by the strain. So as calculating the stress of a foam projects from configuration space onto 'stress space' we shall term the stress-strain relation the stress-orbit of the foam. As noted before the orbit of a $\theta = 0$ foam has a simple periodicity. In Ref. [81] it is shown that many other orientations also have periodic orbits. However the periodicities of these orbits can be of almost arbitrary complexity, some examples are shown in Figs. 2.25, 2.27 and 2.28. These periodic orbits are however sparse in the set of initial configurations, they are related to sets of relatively prime integers (arising from a Diophantine equation), whilst the entire set is related to a real interval.

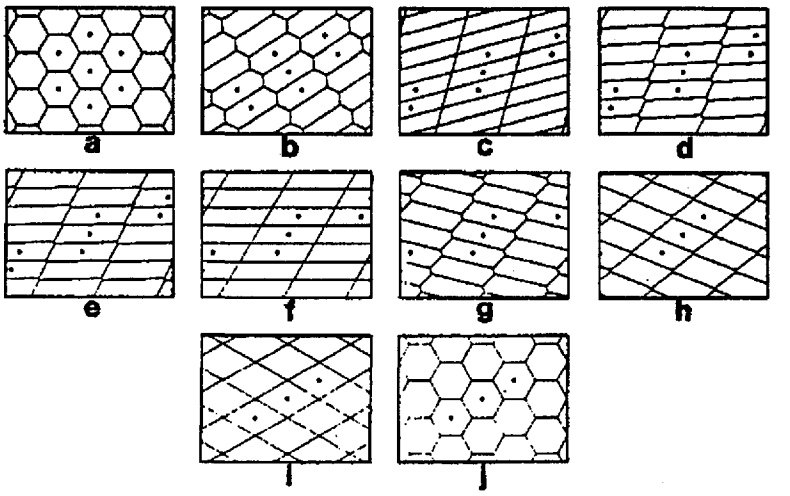

Figure 2.26: Periodic behaviour for $\theta = \pi/6$ under simple shear - cell motions

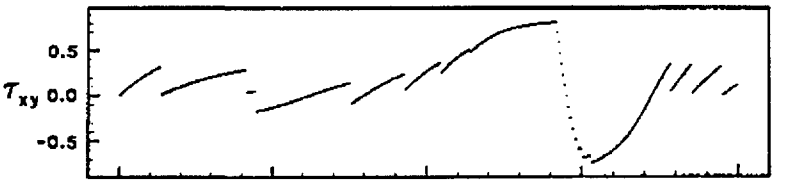

Figure 2.27: Aperiodic behaviour for $\theta = \pi/12$ under simple shear - stress vs strain

Thus the majority of orbits can be proven to be aperiodic [81] (Figs. 2.27 and 2.29). These different sets of orbits exist for both extensional and simple shear, however they can be proved to be mutually exclusive, that is no configurations can exist which are periodic under both simple and extensional shear.

In fact, there are even more wonders hidden in the regular foam orbits [82], which we shall see in Chapter 4. Now, being able to calculate the entire orbit for differing orientations, Kraynik and Hansen [81] were able to extend predictions of foam yield stress and steady flow stresses. They concluded that the best prediction of foam steady flow stresses could be made by averaging the calculated stress over some strain interval. As they noticed that some aperiodic orbits led to unbounded stress-orbits (e.g. Fig. 2.29) they restricted themselves to averaging periodic orbits. Such calculations lead to a value of $\hat{G} \simeq 0.5$ which is in rough agreement with other work mentioned above, and with simulations. When calculating the yield stress Kraynik and Hansen noted that there are several possibilities; either the stress at the first T1 (start of plastic flow), the maximum stress in the period (at some T1 but not necessarily the first) or the average steady flow stress $\langle\tau\rangle$ (corresponding to a flow situation). In the framework of their model, with its somewhat loose connection to real foams, it is impossible to favour one above another. Again such predictions give order of magnitude agreement with other models, but do not appear to offer very concrete physical predictions. As we noted above our model is close to

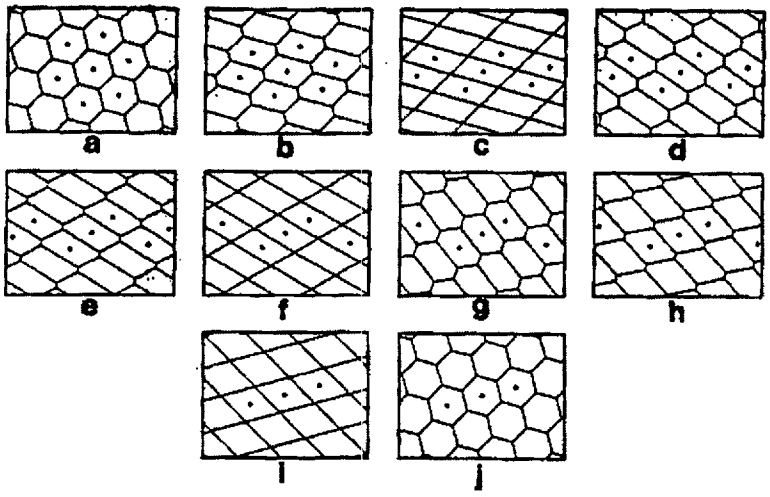

Figure 2.28: Periodic behaviour for $\theta = \pi/12$ under extensional shear - cell motions

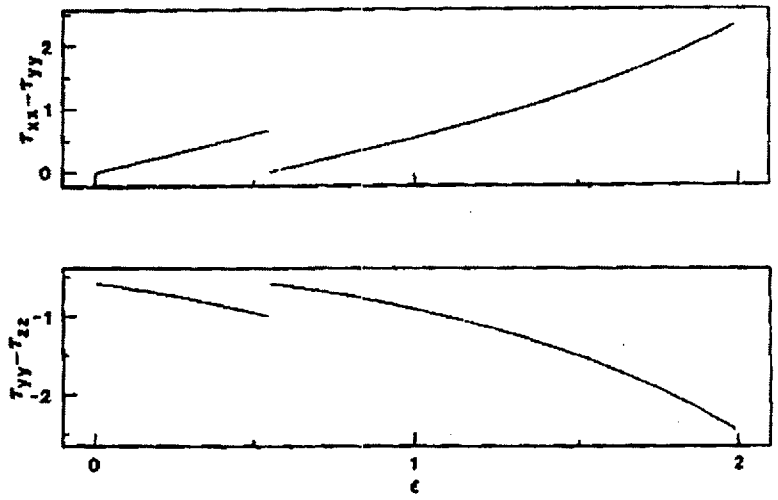

Figure 2.29: Aperiodic behaviour for $\theta = 0$ under extensional shear - stress vs strain

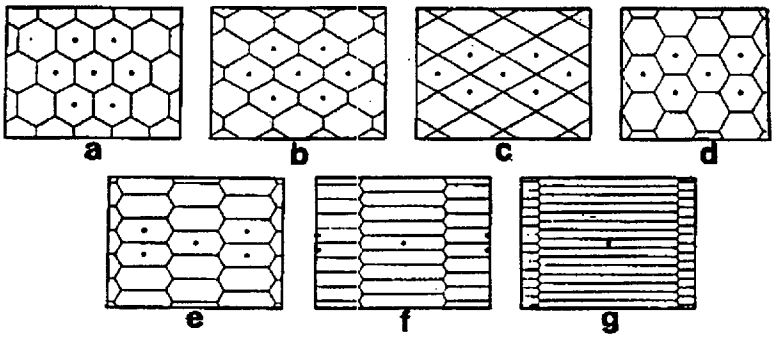

Figure 2.30: Aperiodic behaviour for $\theta = 0$ under extensional shear - cell motions

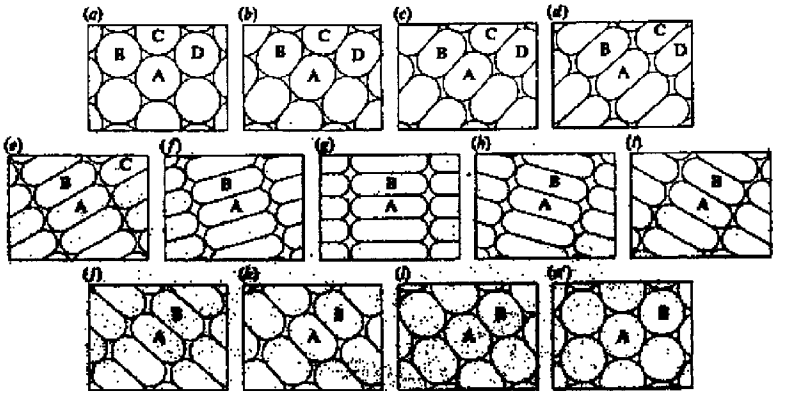

Figure 2.31: Periodic behaviour for wet $\theta = 0$ foam under simple shear

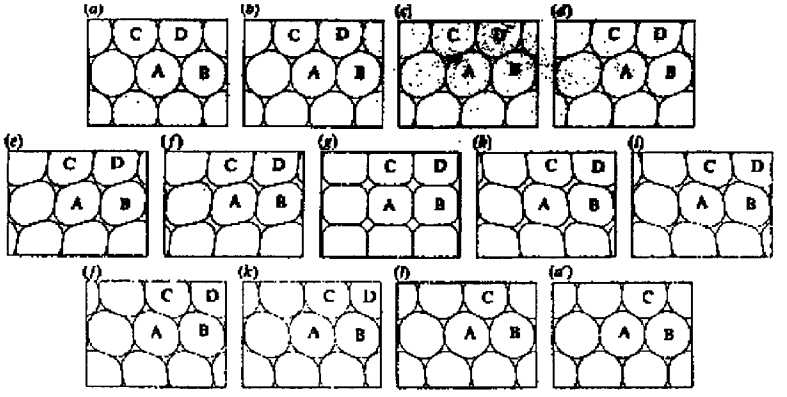

Figure 2.32: Periodic behaviour for wet $\theta = \pi/6$ foam under simple shear

this (Princen-Prud'homme) model of foams, and we shall return to these points in Chapter 4.

Subsequently the model was advanced further by incorporating finite liquid content and also improved modelling of the viscous forces acting inside the thin films and Plateau borders. Once again Khan and Armstrong [83] studied the mechanics for small deformations up to the first T1, and Kraynik and Hansen [84] pushed the analysis beyond the T1 into the longer term behaviour. Unfortunately these first attempts at modelling the viscous forces used a rather unrealistic model of the origin of the forces, wherein each film is supposed to undergo planar extension at constant volume. Subsequent models used an argument of Mysels et al. [85], adapted by Schwartz and Princen [86], which models closely the flow of fluid as it is withdrawn from the Plateau borders (this mechanism is given in detail in Appendix B, and used in Chapter 4). Nevertheless this model indicated that although the extra stress generated by the viscous forces was small, so that its direct impact was also small, its effects on the structure and thus on the total stress could be important. The presence of viscous forces also smoothed the orbits. The model of Kraynik and Hansen also incorporated a rough attempt at dealing with finite fluid content at the Plateau borders by invoking a T1 event when the opposing borders touched across the short film, rather than at zero length.

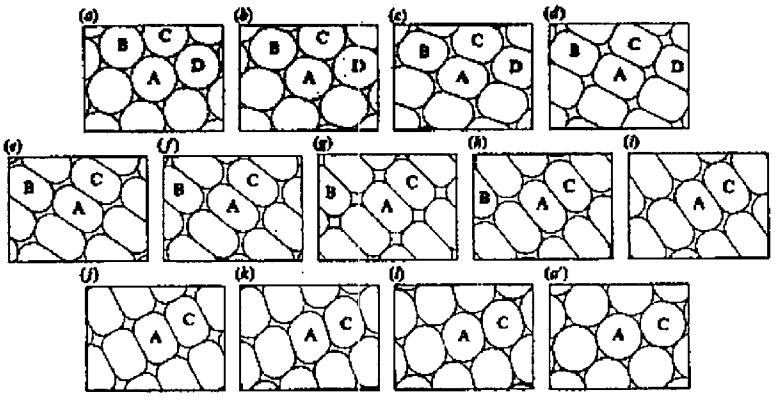

Figure 2.33: Periodic behaviour for wet $\theta = \pi/12$ foam under extensional shear

In Ref. [87] Reinelt and Kraynik extend the Princen-Prud'homme model to cover foams with finite fluid content properly, incorporating the Schwartz-Princen [86] model of film fluid flow.

So far we have reviewed work which either ignores disorder and concentrates on the mechanics of the foam, or which ignores the detailed mechanics and concentrates on the disorder. It is possible to include both in a model, up until now this has been done by using some form of simulation.

The first use of a simulation to study foam rheology was that of Kermode and Weaire [37], when they published the first results they obtained using their general foam simulator [39, 36], which was discussed in Section 2.6. We discuss here a selection of their results, many of which we hope to explain. In Fig. 2.35 is shown an example of a sample foam in the simulation [56].

The first thing that Weaire and Kermode [37] discovered was that the simulation had many similarities with the idealised Princen-Prud'homme model. The foam showed an initial elastic response, followed by plastic deformation, and then plastic flow [88]. The elastic modulus was shown to be below, but of the same order as, the modulus of the regular hexagonal foam. The dependence of the elastic modulus [89] on the disorder μ_2 was found to be close to linear, although the change is very small over the practically accessible range of μ_2. Later studies [88] led Weaire and Fu to propose the function

$$\hat{S} = \lambda \tanh\left(\frac{e^{\epsilon} - 1}{e^{\epsilon_1} - 1}\right) \tag{2.23}$$

as a fit for the observed stress-strain relation under extensional strain, where $\hat{S}$ is the dimensionless stress, ϵ the Hencky strain and λ and ϵ_1 are fitting parameters.

They also studied [37] the history dependence (or funeousity) of the foam by cycling the applied strain (Fig. 2.34). They found that the behaviour depended very much on the level of strain applied. The strain is applied in one direction up to a maximum strain, then the system is returned slowly to zero strain, then strained to the maximum in the other direction, and so on.

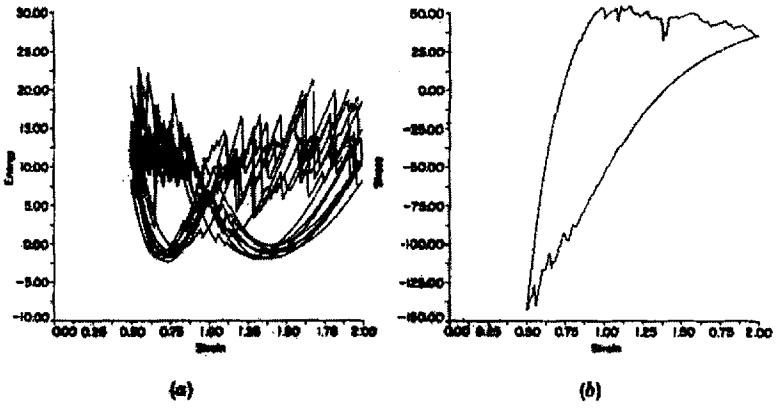

Figure 2.34: Strain cycling

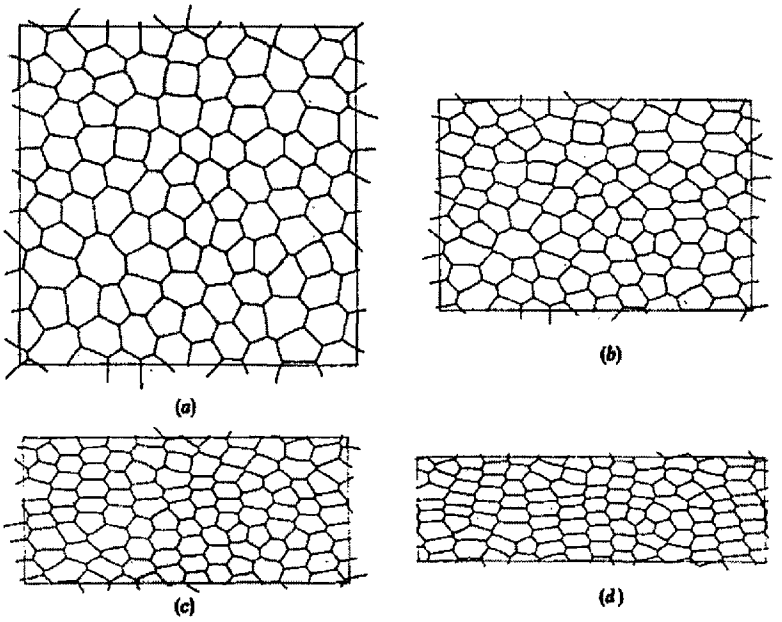

Figure 2.35: Stress affecting topology — extensional shear

For a maximum strain of $\epsilon = 1.7$ (Hencky strain ϵ) they found that only a small amount of T1 events occurred, that is, only a little plastic deformation, so that these reversed on the second half of the cycle, and the foam configuration changed periodically with the deformation. For a larger maximum strain ($\epsilon = 2.0$) they found that the plastic deformation is more pronounced and the foam does not behave periodically, although the orbits are close on each cycle. They hypothesised that as the system size increased the latter behaviour would become dominant, the periodicity resulting from small system size.

Weaire and Kermode also studied the phenomena of creep, and of the interaction between the foam's structural disorder and stress state. An initial sample is taken to be at zero strain, and thus stresses are only those dictated by the structure which are assumed isotropic (in a stochastic sense), applying strain defines some preferred directions which can lead to ordering.

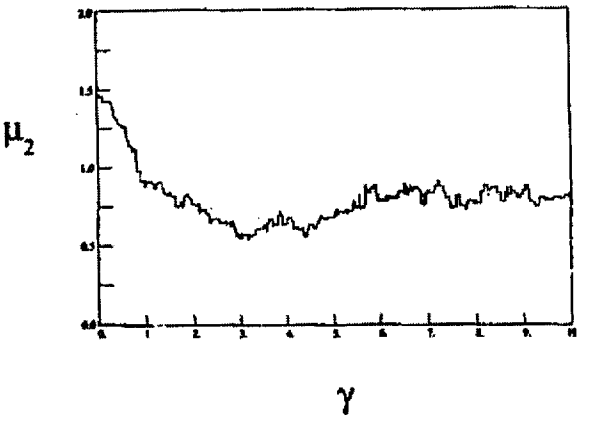

Figure 2.36: Stress affecting μ_2 — simple shear

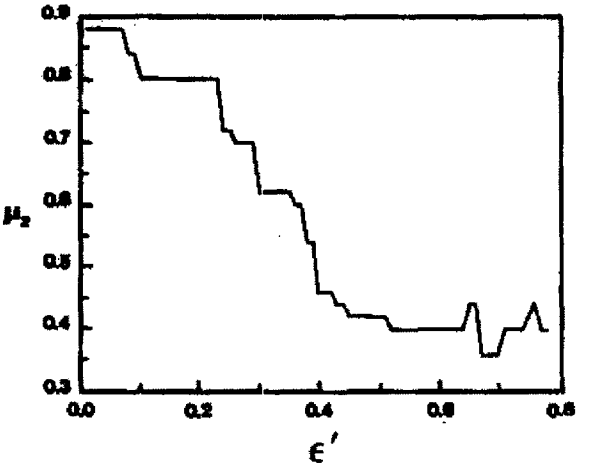

Figure 2.37: Stress affecting μ_2 — extensional shear

Indeed in Ref. [90] they observe considerable ordering during extensional shear, and almost as much in simple shear.

Thus strain leads to 'strain-induced ordering', moving the foam towards the hexagonal ideal. Coarsening as we know moves the foam distribution towards another asymptotic limit, the scaling distribution with $\mu_2 \simeq 1.5$. Thus we expect that a strained foam left to coarsen will lose its order slowly, and thus the stored stress energy as well. This phenomenon was noted in Ref. [37], and is shown in Fig. 2.38.

Finally the simulation was extended to deal with wet foams, and a variety of new interesting features discovered. These features will be mentioned in Section 2.8 below. The dependence of the elastic modulus on the liquid content is shown in Fig. 2.39.

Herdtle made similar calculations of the stress-strain relationship for dry foams under simple and extensional shear, and on the connection between topology and stress history. However these results have only been presented in Ref. [91].

Such accurate portrayals of foam as those discussed above have heavy overheads in terms of

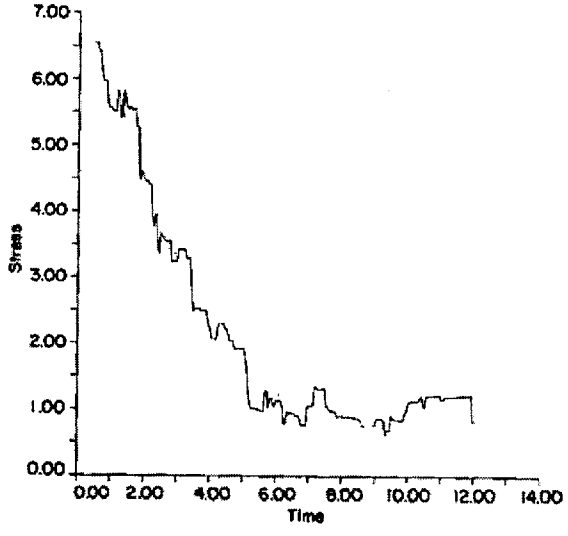

Figure 2.38: Creep

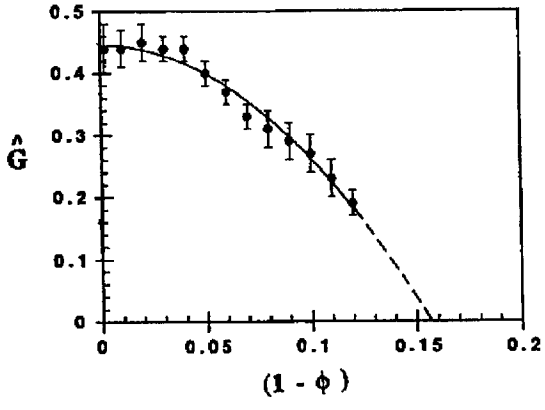

Figure 2.39: Elastic shear modulus against $(1 - \Phi)$

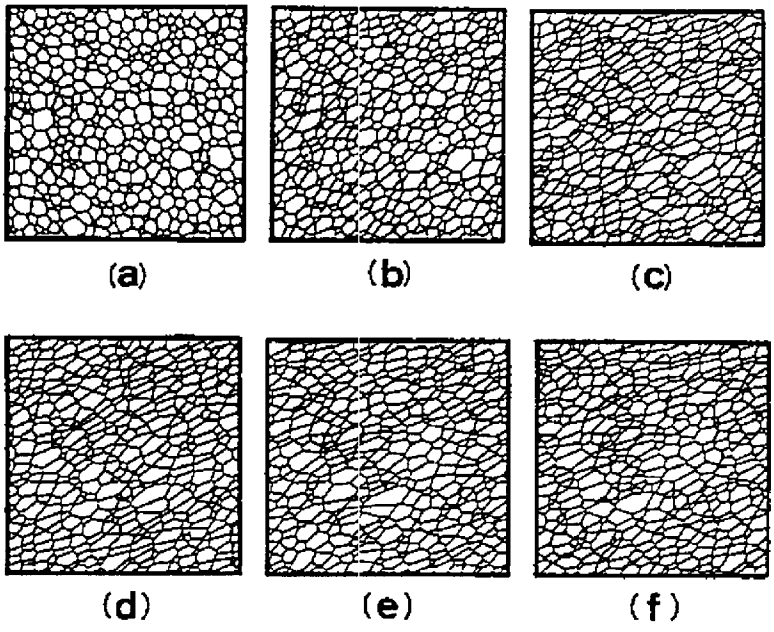

Figure 2.40: Stress affecting topology — simple shear

calculations, and thus only small systems and short timescales can be effectively studied, and possibly only using expensive supercomputers [42]. However it is possible to consider larger timescales and systems if the model is idealised somewhat. To idealise the model a basic feature must be chosen and an attempt made to reconstruct the foam from this element.

The work of Okuzono, Kawasaki and Nagai uses the vertex as the primitive element of the froth, and extends the model used in Ref. [43, 44] and discussed above in Section 2.6. In order to study the rheological properties of the system it is necessary to incorporate into the dynamics a constraint keeping the cell areas constant, which may be done with a Lagrange multiplier. This is because the model does not correctly account for the differing timescales of diffusion and film relaxation in foam, but is akin to grain growth (where the model originated) with equal rates for both effects. The dissipation function is derived from the model of Schwartz and Princen [86] as mentioned above. The strain may be imposed on the system in two ways; either by imposing a velocity field on the vertices [92, 93] or by manipulating the periodic boundary conditions to mimic strain application [94]. In Ref. [93] Okuzono et al. used the first method to obtain the results shown in Fig. 2.41 for the shear stress, a simulation sample under simple shear is shown in Fig. 2.40.

By using the second method, Okuzono and Kawasaki [94] showed that the dynamics of foam can be far from uniform. Under simple shear the foam undergoes intermittent avalanches of activity, separated by quiet periods of strain absorption. This behaviour is very similar to that studied by Bak and others [95, 96, 97, 98], and termed self-organized criticality (SOC). SOC behaviour has yet to be rigorously defined or explained but the essence is that a system

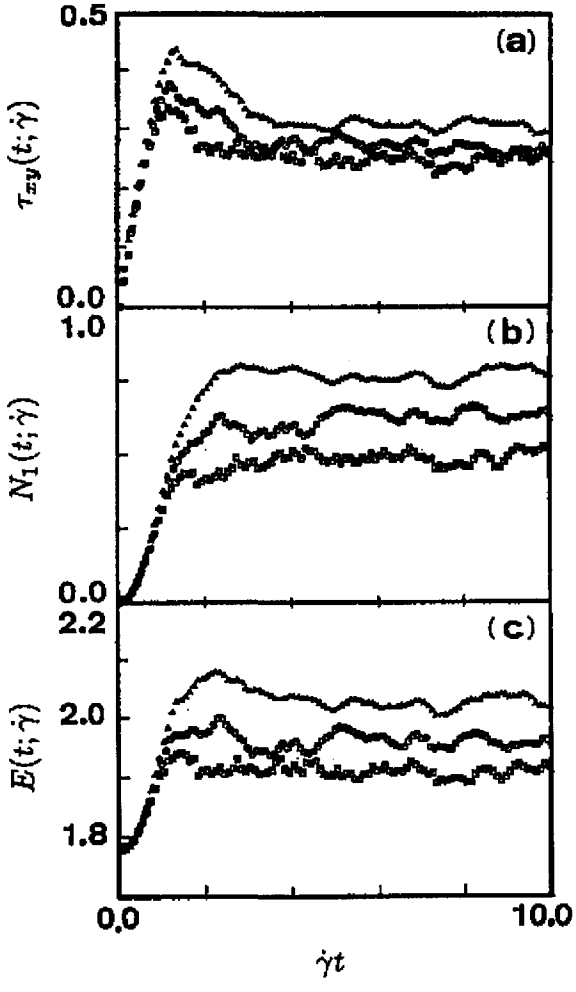

Figure 2.41: Stress-strain relation from vertex simulation

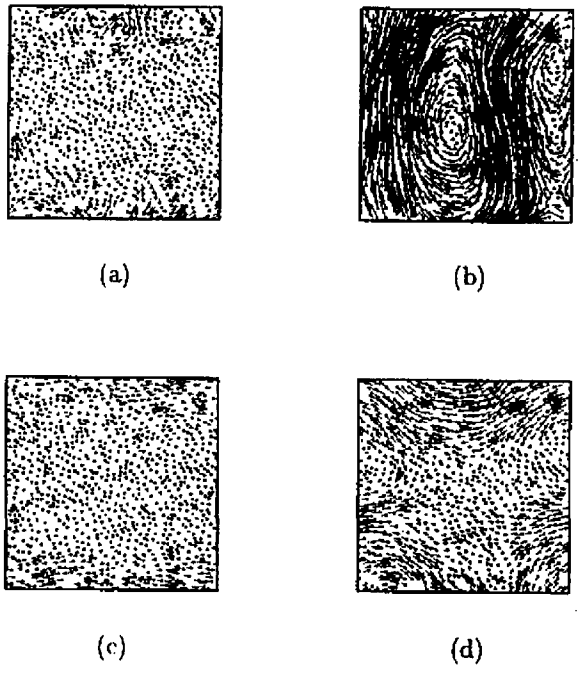

Figure 2.42: Episodic rearrangements under simple shear

exhibits this punctuated dynamics. A typical SOC system has some spatial correlations which cause the system to move towards, and then remain near, some metastable submanifold of the phase space.

SOC models were designed to explain the ubiquity of the $1/f^{\beta}$ spectra in physics; these are caused by the scale invariance of the avalanche size distribution. Okuzono and Kawasaki calculated the power spectra of the avalanche size distribution, and the energy and shear stress time series. They found that they all had the expected $1/f^{\beta}$ form; the time series had $\beta \simeq 2$ and the distribution had $\beta \simeq 1.5$. These features will be discussed further in Chapter 4.

The work of Kawasaki et al. has been extended by Yuan and Edwards to deal with the question of real flow situations. This is the most interesting development of the work on foam rheology, the first movement towards the real goal of these studies. By developing a scheme for calculating the pressure gradient in the foam [99] they are able to impose deformations by increasing the pressure at one end of a system relative to the other. Periodic boundary conditions are applied across these ends, and the other two boundaries are treated with sticking conditions, that is the bubbles touching the boundaries are fixed there. Whilst theory is not really at a stage where it can be compared to the simulation results one interesting, and relieving, discovery is that the predicted yield stress compares well with those obtained by Kawasaki et al. using simple shear.

The final simulation we shall consider is that of Durian [100]. This model focuses on the bubbles as the most primitive element of the foam, and is well fitted for considering very wet foams. Durian tracks each bubble's course during the deformation applying a simple dynamics

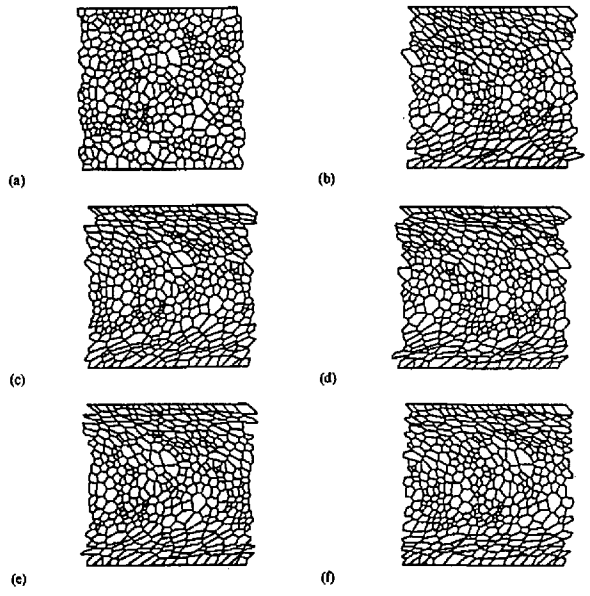

Figure 2.43: Flow simulation

composed of two parts. The first part is due to the energy increase when two bubbles deform as they come into contact. The second part incorporates viscosity, via a pairwise additive force proportional to the velocity difference of neighbouring bubbles (this is the simplest form for a viscous drag). Whilst this model has yet to be fully developed it has already produced interesting results. Whilst both Durian and Weaire et al. agree on a value of $\Phi \simeq 0.84$ for the rigidity loss transition, the form they obtain for the dependence of G on Φ is markedly different. Durian has (Fig. 2.45) $G \simeq (\Phi - \Phi_c)^{1/2}$, whereas Weaire et al. have [101, 102, 103] $G \simeq a + b(1 - \Phi)^2$. It is intriguing that the Φ_c estimates line up, though they are not firm figures as such, as they are obtained by fitting the curve through the points and extrapolating. The best explanation of the disagreement is that the work of Durian was for simple shear and that of Weaire et al. was for extensional shear. Whilst these two shears should agree for infinitesimal deformations and therefore for the shear modulus they will disagree for the finite measurements which must be used in simulations. Furthermore the elastic regime is rigorously non-existent in foams and in small samples the plastic effects may alter the results markedly.

The bubble simulation does agree with other models in predicting a Bingham plastic dependence of the yield stress, as shown in Fig. 2.45.

2.8 Foam Osmotic Pressure

The first model of foam osmotic behaviour was that of Princen [2]. He considered a regular hexagonal foam and from the symmetry was able to determine the structure for all values of the liquid fraction Φ between the perfectly dry foam $\Phi = 0$ to the point at which the bubbles

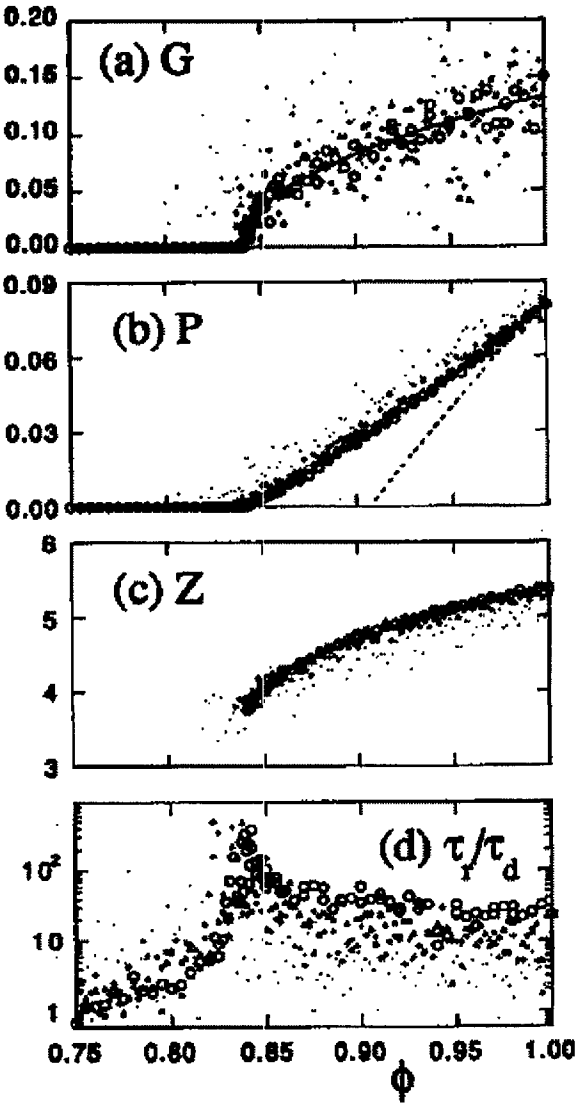

Figure 2.44: Various results from Durian's bubble based simulation

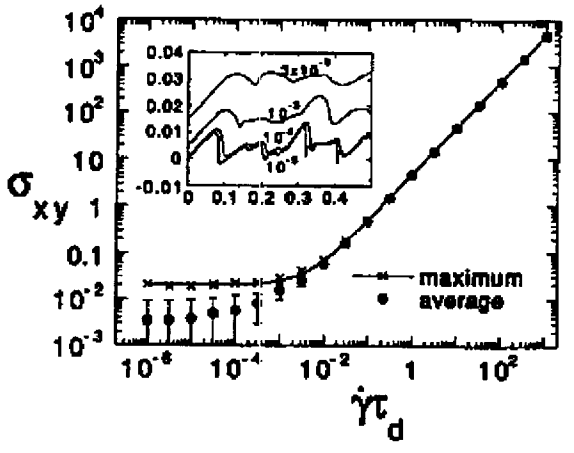

Figure 2.45: Bingham plastic behaviour of yield stress

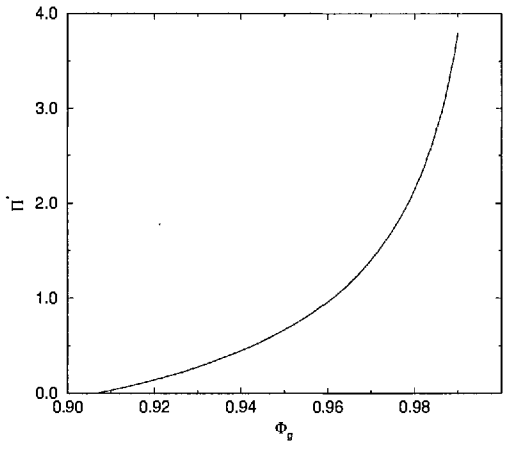

Figure 2.46: The osmotic pressure Π^* for an ordered hexagonal foam

fall apart Φ_c. For a regular hexagonal foam $\Phi_c = 0.9069$. Princen's calculation worked from the $\Phi = \Phi_c$ up to $\Phi = 0$. In Appendix C we reproduce a similar argument but working from $\Phi = 0$ to $\Phi = \Phi_c$ which will be more convenient to generalise.

In Fig. 2.46 we plot the result of Princen. For comparison with the results of Weaire et al. [104] we use the following normalization $\Pi^* = \Pi \overline{A}^{1/2}$, where $\overline{A}$ is the average bubble area (πR^2 for the ordered case). Π^* is dependent on the surface tension parameter, we consider it here for $\sigma = 1$.

In [104] Weaire and Hutzler used their foam simulator (Section 2.7.3) to calculate Π directly for a 200-cell disordered foam. The expectation was that, as a result of the Bolton-Weaire decoration lemma, the behaviour should be similar for large Φ, but that significant deviations could occur around Φ_c. These deviations are due to the coalescence of three-sided Plateau borders, forming borders with more sides. Unlike in the hexagonal foam above, not all thin films go to zero length at the same time, so that there may be many coalesced borders before the point of foam disintegration.

The osmotic pressure can be calculated most efficiently in the simulator by rewriting it as

$$\Pi = -\left(\frac{\partial F}{\partial A}\right)_{A_g} = \frac{1}{2}\left(\tau_{xx} - \tau_{yy}\right) - p_{pb} \tag{2.24}$$

where p_{pb} is the pressure in the Plateau borders. This pressure is taken to be constant throughout the foam. This corresponds closely to reality, as in 3D the Plateau borders form a network, and even in 2D are connected by the liquid layers on the glass plates.

The simulation results are shown in Fig. 2.47. It is evident that if one continues to increase the fluid fraction of the foam indefinitely then at some stage the foam will disintegrate into a collection of free bubbles. At some stage the cells are no longer all deformed and in contact, they are just packed together, beyond this point steric effects play a lesser rôle and the bubbles

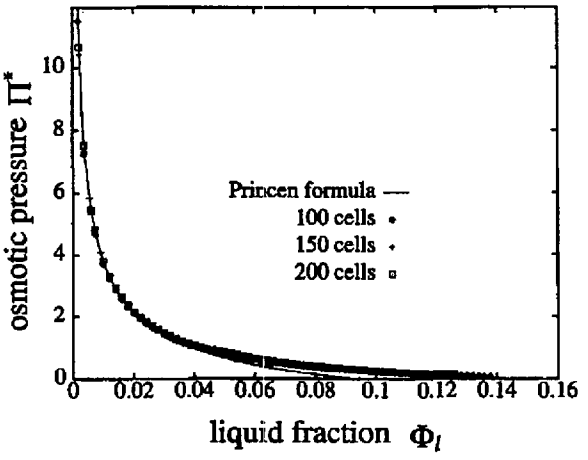

Figure 2.47: The osmotic pressure Π^* for ordered and disordered 2D foams

are free. It seems clear that what is observed will be some kind of percolation phenomenon. There is a changing probability of a certain pair of neighbours constraining each other, and at some point this lack of constraints percolates throught the system, allowing it to fall apart. However, note that this is not common or garden 'local' percolation, as in forest fire models etc., but is akin to rigidity percolation [105, 106]. The connection between sample rigidity and individual neighbour constraints is non-local, and non-rigidity is not attained by a simple percolating path across the system. If we apply the experience of studies of rigidity percolation to our problem we find some interesting connections.

A simple argument in [107] says that for compactions of hard disks the disintegration of the structure should occur when the disks have an average contact number (number of touching neighbours) of $Z = 4$. We arrive at this conclusion by noting that as the disks have circular symmetry their rotational degrees of freedom are irrelevant. So they only have their two translational degrees of freedom. Thus, if the average contact number is Z there are only $2 - Z/2$ degrees of freedom consistent with the structure; if Z drops to 4 then there are no degrees of freedom consistent with that structure and it is unstable to disintegration. These events are very similar to what happens during the random severing of springs in a spring lattice [105, 106]. In the foam there is no lattice, but there is a network (the Delaunay triangulation) which is defined for each disordered foam structure uniquely. Therefore it is tempting [103] to also compare their results on the mean-field theory of such lattices. Their findings are that the elastic and bulk moduli go to zero linearly at the rigidity loss transition. This prediction is apparently matched by the results of the foam simulation.

However, as the bulk modulus is the first derivative of the osmotic pressure with respect to Φ this implies a quadratic dependence of Π on Φ in the vicinity of the transition. This also apparently agrees well with what is seen in the simulations, as shown in Fig. 2.48, although the errors in the results are fairly large so that other dependencies can not be ruled out.

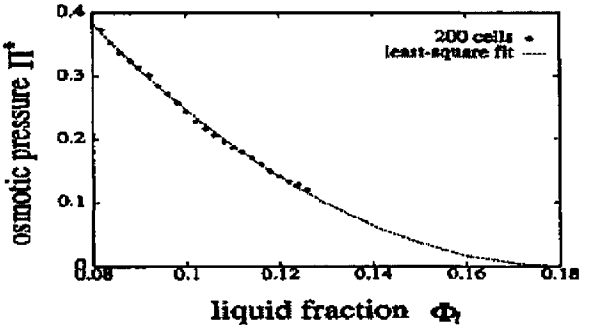

Figure 2.48: The osmotic pressure Π^* close to the rigidity loss transition fitted to a quadratic

The osmotic pressure can be fitted to a quadratic

$$\Pi^* = a(b - \Phi_l)^2 \tag{2.25}$$

and then we find that $a \simeq 37$ and $b \simeq 0.18$. $1 - b$ is the value of the critical fraction Φ_c at which the foam disintegrates into its constituent bubbles and has a value $\simeq 0.82$. This value is evidently considerably lower than the critical fraction for hexagonal foams $\Phi_c^h = 0.906$.

2.9 Foam Drainage

An interesting and connected area is the study of foam drainage. This is important because the way in which foam drains determines how we go about creating and destroying foams, and the equilibrium forms which foams adopt. When we first create a foam it has a certain liquid volume fraction Φ. If we allow this foam to stand the liquid phase, being the denser, drains out of the foam to the liquid phase reservoir at the bottom. However it is clear that the liquid phase does not completely leave the foam, because the osmotic pressure in the foam would lead flow back into the bulk. This leads to several questions; at what rate does the liquid phase flow out of the foam, what form does the flow take, and what is the equilibrium dependence of Φ on height?

The first major investigator of foam drainage was Weaire. Experiments had been done before involving the rate of drainage from wet foams, and the equilibrium form of foams, but without much success because theory was not up to comparison. Weaire [108] suggested a new system for the study of drainage, one which would be easier to approach and might lead to subsequent models for the other cases. He started to do experiments in which fluid constantly entered a foam stack at the top, drained through, and emerged at the bottom (Fig. 2.49). By adjusting the rate of fluid delivery he could study the drainage of wet foams in a steady state.

At the same time he and Verbist formulated a model [109] which made predictions for this system. The model assumed all drainage to be along the linear Plateau borders, like Mysels [85], and so they modelled viscous flow through pipes with variable cross-sectional area A. In

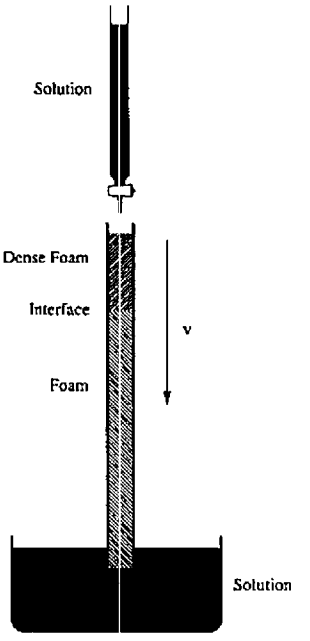

Figure 2.49: Experimental study of steady drainage

this way they were able to derive a non-linear partial differential equation describing drainage,

$$\frac{\rho g}{C\sigma}\frac{\partial A}{\partial \tau} = -\frac{\partial}{\partial \xi}\left(\left(\frac{A\rho g}{C\sigma}\right)^2 - \sqrt{\frac{\rho g A}{4C\sigma}}\frac{\partial A}{\partial \xi}\right) \tag{2.26}$$

The steady flow situation gave them boundary conditions for which the equation had very nice solutions, solitons of the form

$$Q(x,t) = \begin{cases} N x_0 t_0 V^2 \tanh^2\left(\sqrt{\frac{Vt_0}{x_0^3}}[x - Vt]\right) & x \leq Vt \\ 0 & x \geq Vt \end{cases} \tag{2.27}$$

where $Q(x,t)$ is the flow of fluid at a point $Q = Au$. By using many of these pipes in parallel the foam is approximated. The predictions of the model match very well the experimental facts, with a clearly observable solitary wave propagating down the foam stack. The total flow behind the wavefront is proportional to V^2 which is also seen in the experiments. Furthermore, the solitary wave solution has other interesting properties. Increasing the fluid delivered at the top Q means an increased flow in the wave, and a secondary wave with a higher velocity should start from the top. This has also been qualitatively confirmed in experiment. Other work was done by Fortes and Coughlan [110] but it came to less firm predictions.

Our interest in this thesis, in connection with our work on foam osmosis, will be to predict the equilibrium profile of a drained foam.

2.10 Conclusions

In summary we see that a substantial amount of work has been done on the rheological and osmotic properties of foam. The aim throughout has been to develop models of disordered foam, as this is the kind of foam found in the real world, however the success has been limited. The work can be split into three areas; analytical, qualitative and numerical. We consider the three :

- The analytical work has concentrated on the behaviour of regular hexagonal foams. This has been useful because the models are exactly soluble in certain situations — these models have given evidence for a yield stress, and expressions for average stresses. However, the exact symmetry of the model has limited its applicability, so that only time (strain) averaged quantities are of interest, which means that the real rheological response is still unreachable. Whilst the model suggests certain additional features (yield stress etc.) the artefacts are so strong that even qualitative predictions are impossible. Likewise the osmotic model is interesting but evidently cannot shed light on such features as the rigidity loss transition.

- The qualitative work referred to is that of Cates, Edwards, Pithia, Witten, and Morse. Such work is interesting because it is well founded and gives good analytic estimates of properties. However, it, too, is not yet capable of producing more accurate predictions, or more complex features such as stress-strain curves. This is because such models typically only consider one film or bubble in the foam, and ignore the larger geometrical/topological structure.

- The simulations and numerical calculations constitute the largest part of the work done. They are both exceptional and useful. They provide real two-dimensional foams for comparison to theory, and to an extent models of foam. However, most of the simulations are so close to real foam as to offer no simplification of the properties — they do not tease out the topological and geometrical identities. Furthermore, they are so computationally intensive that they are only realisable for small numbers of cells, so that no good predictions for large realistic systems are possible. Thus, they sit uncomfortably between experiment and theory.

Thus, there is still a lot of space for models of foam structure and behaviour which can directly incorporate a description of disorder to give realistic predicitions of experimental properties and separate the different aspects of the foam to give some real understanding of its workings.

Chapter 3

Voronoi Diagrams and Foam

A Voronoi diagram is the union of the Wigner-Seitz cells of a collection of generators. Hereafter we shall refer to the generators as 'sites', and the Wigner-Seitz cells as 'cells'. These structures enjoy a vast collection of names, due to their huge range of applicability; Voronoi diagrams, Thiessen tesselations, Dirichlet tesselations to mention but a few. As mathematical cellular structures, with a firm definition and thus greater hopes of analytical tractability, they are of great interest to those studying physical cellular systems of all kinds. The use of Voronoi diagrams and their generalisations in the study of foams has been considerable. As a model of the necessary correlations in space-filling structures without any dynamic effects they have long been studied [111, 112, 113, 1, 114, 6, 10]. Many simulators start with a Voronoi diagram as the initial state [37, 93]. The Laguerre diagram, a generalisation of the Voronoi diagram, with a size parameter for each site, has been successfully used to simulate foam. The diagram is used to model the foam so that the only data the simulation must track is the position and size of each site. The surface tension dynamics is mapped into this space and provides a very efficient simulation [115, 116, 117].

Our aim here is to further the work done on the distribution functions of stochastic two-dimensional Voronoi diagrams (with randomly positioned sites) as a model for random cellular structures [1, 112, 118].

For the remainder of this chapter we shall be referring to two-dimensional Voronoi diagrams constructed in the plane, perhaps with periodic boundary conditions. Most of the ideas could be extended to three-dimensional diagrams, but this involves some subtleties and has not yet been accomplished. Thus the work outlined here is really related to two-dimensional foams, although we hold to the tenet explained in the previous chapter that such results should give some qualitative results for three-dimensional foams.

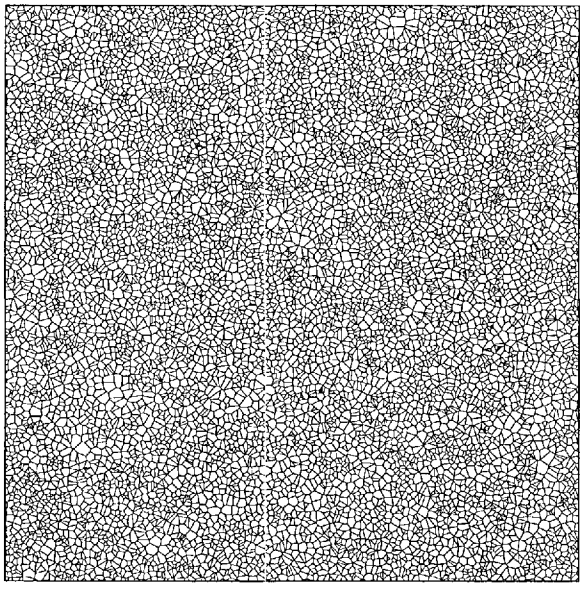

Figure 3.1: A Voronoi diagram

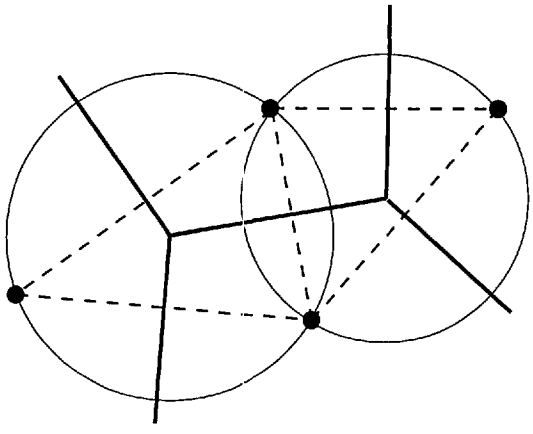

Figure 3.2: Delaunay triangles and sites

3.1 Voronoi Diagrams

The Voronoi diagram of a set of sites is the union of the Voronoi cells (cells) of the sites. The cell of site X is the convex polygon which contains all those points in the plane which are closer to site X than to any other site. The boundary of the cell is composed of straight line segments, these lines perpendicularly bisect lines joining neighbouring sites. We will again use the term 'topology' to refer to the number of sides of a cell. Three line segments, or edges, meet at each vertex of the diagram, so that the diagram is a three-valent planar graph. Vertices of higher connectivity are possible but rely on special symmetries in the locality, they are topologically unstable in the same way higher valency vertices are physically unstable in foams. Essentially topological instability means that such features arise with probability zero, or such localities make up a set of measure zero. To exclude such cases the literature often refers to Voronoi diagrams for sites in 'general position', this means that no four or more sites lie on a common circle. Because they are three-valent planar graphs, like foams, Voronoi diagrams also obey Euler's law $\overline{n} = 6$.

As a valency three planar graph the Voronoi diagram has a well defined dual which is a planar triangulation. This triangulation is known as the Delaunay triangulation of the set of sites. The sides of a particular Delaunay triangle join three neighbouring sites. The edges of the Voronoi diagram are the perpendicular bisectors of the sides of the triangle. The three edges meet at the vertex, which is the circumcentre of the triangle. These relations are depicted in Fig. 3.2. The most important feature for our work is that the three sites defining the position of the vertex lie on the circumcircle whose circumcentre is at the vertex, and that no other site may lie inside (or on) this circle.

We shall be interested in stochastic Voronoi diagrams formed from randomly distributed sites. The distribution used will be the Poisson point process, with or without a hard-core repulsion between sites. We study the case where the expected density of points is one per unit area, $\rho = 1$, evidently other cases are easily determined by scaling the results. The definition of the Poisson point process without hard-core repulsion is that all infinitesimal areas dA have equal probability of containing a site equal to ρdA. The probability of more than one site falling in the same infinitesimal area is taken to be zero. This implies that the probability $P_0(A)$ of some area A containing no sites is proportional to $e^{-\rho A}$.

The Poisson point process with hard-core repulsion is similar, but after each site is placed the area in which the next site can be placed is redefined to exclude the disc of radius R around that site. This leads to a Voronoi diagram with more isotropic and bubble-like cells.

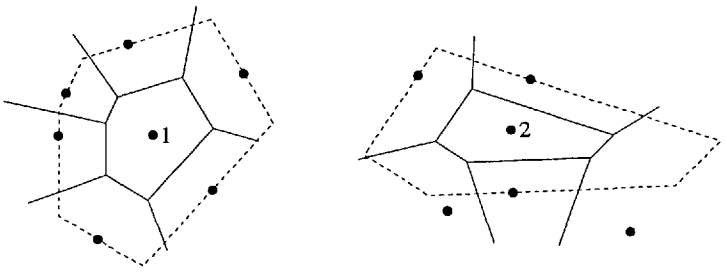

Figure 3.3: Active zones of sites

3.2 Distribution Functions

The first studies of the distributions of Poisson-Voronoi diagrams were made by Meijering [119], who derived expressions for the mean values of many quantities including the area. This work was subsequently extended by Gilbert [120] who derived variances for many of these quantities, including the topology and area. The first work which focussed on the form of the distributions was that of Kiang [121], who fitted a gamma distribution to the area distribution, taken from measurements, giving

$$f(A) \propto A^{\gamma-1} e^{-\gamma(A/\overline{A})} \tag{3.1}$$

with $\gamma \simeq 4$, where A is the area of the cell in units of the average cell area. Weaire et al. gave an intuitive justification of this finding in Ref. [118]. They started from the distribution of nearest neighbour distances, and invoking the fact that the average cell has six sides worked out the distribution of areas arising from six independent neighbours. The end result was Eq. 3.1 with $\gamma \simeq 3.63$. This is in good agreement with Kiang, especially with his revised estimate of $\gamma \simeq 3.5$.

Kumar et al. [112] extended an argument of Weaire's [122] explaining the Aboav-Weaire law for foams, to cover Voronoi diagrams. Voronoi diagrams appear to follow a similar law but with a slightly different form. The work uses the exact result of Miles [123] for the vertex angle distribution in two dimensions

$$f(\alpha) = \left(\frac{4}{3\pi}\right) \sin\alpha(\sin\alpha - \alpha\cos\alpha) \tag{3.2}$$

and a rough estimate of the correlations between angles to obtain this form of the Aboav-Weaire law,

$$m_n = 4.942 + \frac{7.223}{n} - \frac{6.543}{n^2} \tag{3.3}$$

where m_n is the average topology of a cell neighbouring an n-sided cell.

Mulheran pushed these lines of thought further with Ref. [1] in which he obtained approximate expressions for both the area and topology distributions. The work in this chapter is an extension of his ideas. Mulheran's approach was to consider the probability of the sites lying in the necessary regions to create a cell of a specific configuration (area and topology), (for details

see Ref. [1]). The idea is that there is an 'active area' for each site, which just contains those sites which determine the configuration of the site's cell. For example consider cells 1 and 2 in Fig. 3.3. It is easy to see from the definition of the Voronoi cell that the active zone must be contain at least the area formed by doubling the linear dimensions of the site's cell. The neighbours of site 1 lie exactly on the boundary of this area, so that this is exactly the active zone of site 1. This means that the active zone of site 1 has four times the area of cell 1. If we construct the same 'double-cell' for site 2 we find that some neighbouring sites lie outside the double-cell, thus the active zone of site 2 has somewhat more than four times the area of cell 2. Therefore, we suppose in general that a cell of area A on average has an active zone of area νA, where ν will be determined later, with $\nu > 4$. Now we can frame the question "Given an n-sided cell, what is the probability $f_n(A)\ dA$ that its area falls between A and $A + dA$", using the active zone's properties :

1. The active zone must contain the cell's own site and all the other n neighbouring sites. All other sites must lie outside the active zone.

2. The final element of active zone area must contain the last neighbouring site.

3. The active zone must contain at least two nearest neighbours since all cells have $n \geq 3$.

By taking into account all these requirements we find

$$f_n(A)\ dA = \frac{\nu^{n-1}}{(n-2)!} A^{n-2} e^{-\nu A}\ dA \tag{3.4}$$

Now by using this equation we can obtain a form of Lewis' law

$$\langle A_n \rangle = \int_0^\infty A f_n(A)\ dA = \frac{1}{\nu}(n-1) \tag{3.5}$$

We can use this expression to obtain ν, using $\overline{A} = 1$

$$\sum_n \phi_n \langle A_n \rangle = \frac{1}{\nu}\left(\sum_n n\phi_n - 1\right) = 1 \tag{3.6}$$

and Euler's law so that $\nu = 5$.

Now we can use the same method to obtain ϕ_n, the distribution of cell topologies. As each cell must have at least three neighbours the probability of a cell of area α having n neighbours is the probability that its active zone contains $n - 3$ extra neighbour sites and no more. This argument yields

$$\phi_n = \frac{(\nu\alpha)^{n-3}}{(n-3)!} e^{-5\alpha} \tag{3.7}$$

where $n > 3$.

This idea of calculating the distributions from considering the necessary populations of various areas is thus very successful. However this particular example now has a limitation, in that the formulae Eq. 3.4 and Eq. 3.7 give one distribution when the value of the other variable

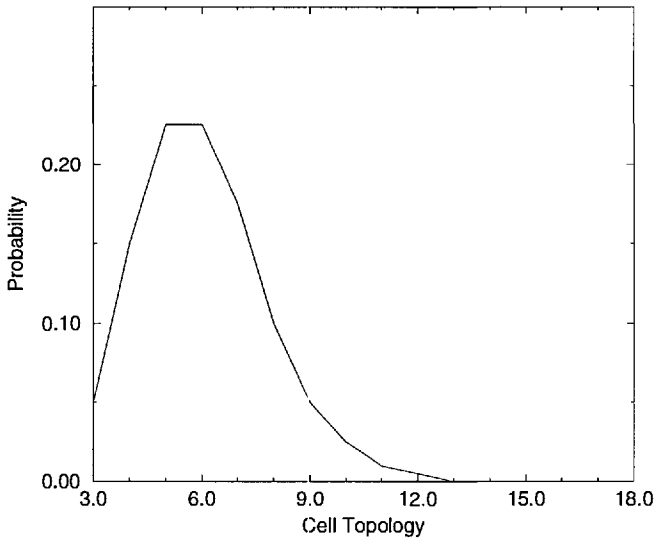

Figure 3.4: Plot of ϕ_n against n

is known. Part of our aim is to improve this situation. However by using one value of the area to characterise the whole diagram we can obtain rough estimates of the distibutions. Mulheran does this by requiring Eq. 3.7 to obey Euler's law, which implies that $\alpha = 3\overline{A}/5$. We can now plot ϕ_n and $F(A)\ dA = \sum_{n=3}^{\infty} \phi_n f_n(A)\ dA$. We reproduce here two plots from Mulheran [1] in Figs. 3.4 & 3.5.

For more numerical results from computer experiments see Refs. [111, 124], which are used below. More information on analytical results for means, variances and a few distributions can be found in Ref. [12].

3.3 Area-Neighbours Distribution

It seems interesting to try and extend this approach, using the necessary emptiness of the circumcircles, to cover further distributions. We saw in Section 3.2 how Mulheran used this idea to obtain the distribution of topologies and the distribution of areas. Unfortunately his method would not allow the calculation of the joint distribution, but culminated in Eq. 3.7. This happened because he needed to know the topology to obtain the area distribution, and vice-versa. Thus it would be interesting if we could come up with an expression for the joint distribution. Here we show how we can form an approximate expression for the joint distribution.

Once again our approach is to consider the circumcircle areas which must be empty to form a cell of a certain configuration. However rather than considering the probability of a correct empty area existing we consider the way in which cells might 'collect' sides as sites are dropped.

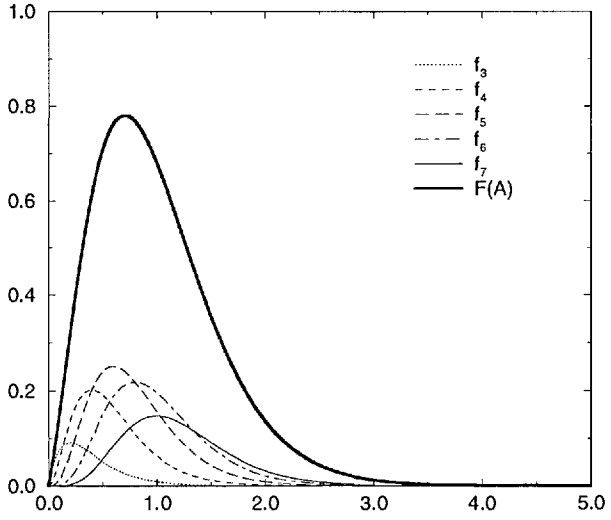

Figure 3.5: Plot of $F(A)\ dA$ and $f_n(A)\ dA$ against A

In a Poisson Voronoi diagram each site defines a cell. The way in which we will consider the cells can be explained in two ways. It is similar to Weaire and Kermode's [40] algorithm for forming Voronoi diagrams on lattices. The diagram can be formed by allowing each site's cell to grow at each time step, starting from zero area; if all cells grow at the same rate the final configuration is a Voronoi diagram. Alternatively it can be compared to the numerical algorithm developed in Appendix A. This algorithm inserts sites one by one, and adjusts the cells as sites are inserted. Clearly the insertion of a site creates a new cell, and forces neighbouring cells to change area and topology. In the following argument we also consider that each site defines an initial cell, which changes as its information about its surroundings increases. Plainly the simplest possible cell is a triangular one, so that each site starts with a triangular cell determined by its three nearest neighbours.

Consider the equilateral triangle depicted in Fig. 3.6. This triangle is formed by the closest three sites to the central site. If we forget for a moment all other sites, these three sites force the central site to have a regular (equilateral) triangular (topology $n = 3$) cell. Now if this is to be the final form of this cell, then the surrounding sites must be so arranged as not to impinge on the central site. This can only be achieved if the moon-shaped area drawn is empty of sites, along with the two rotated copies of it associated to the other sites. The shape of this area is defined by the fact that the central circle is known to be empty (these are three nearest sites), and the fact that for the cell to be triangular the vertices must be formed by the centres of the drawn circle (and its rotated counterparts). Thus these are the circumcircles of Delaunay triangles and must be empty of sites. As can be seen the argument can be duplicated for

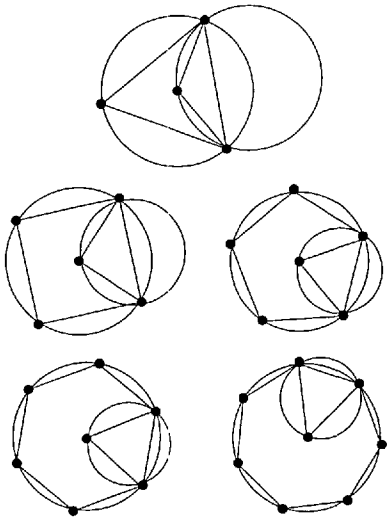

Figure 3.6: Regular neighbourhoods

regular cells of higher topology n, with n crescent-shaped areas. We will borrow terminology from [1] and term the union of these areas as the 'active zone' of the cell. Now we have a way to calculate the probability $P_k(n)$ that if a regular cell has topology n it will keep this topology, and the probability $P_u(n)$ that it will suffer an increase in topology. If the area of the crescent is given by $A(n)$, then the active zone area is $nA(n)$, and the probability of the active zone being empty of sites is $e^{-nA(n)}$. Thus $P_k(n) \simeq e^{-nA(n)}$ whilst $P_u(n) \simeq 1 - e^{-nA(n)}$.

We would like to use this idea to find an approximate expression for the joint distribution. We do this by imagining that all cells are regular, this is necessary so that we can derive usable expressions. Now if a cell of topology n does increase topology then it must, so to speak, 'pass through' the state of having topology $n+1$. Thus if a cell of area α and topology n suffers an increase of topology we assume it gives rise to a cell with area α and topology $n+1$, and then we use the same argument again. This gives us a way of getting a chain of probabilities of cells having different topologies, assuming that the areas of the cells are fixed as their topology changes. This assumption clearly does not hold exactly as each neighbour constrains the cell, and reduces its area, so that the area we use is an overestimate. This error is, however, partly offset by the increase of the average distance of the neighbours from the central site. When a cell increases in topology it is because a new site has been found in the active zone. In our picture the impinging sites are scanned in order of increasing distance from the central site, so that each new neighbour site increases the average distance. However the distance we use in our formulae is related to $\sqrt{\alpha}$, so that it is an underestimate.

So we have a method for obtaining a chain of probabilities. First we need an expression for the probability distribution of $n = 3$ 'seed' cells of different areas, $Q_3(\alpha)$. Then the probability of having a four-sided cell of area A is $Q_3(\alpha)P_u(3)P_k(4)$, that is the probability of getting a seed cell of area α times the probability that that cell increases to topology 4 times the probability

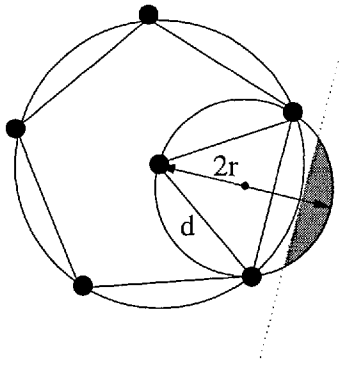

Figure 3.7: Approximate areas

that it stops at that point, and so on.

To put this argument on a firmer footing we need an expression for the area $A(n)$. The area is depicted for a cell with $n = 5$ in Fig. 3.7. Evidently the exact expression for this area will be complex and will not be suitable for our simple argument. Thus we use the area shaded in Fig. 3.7, which is quite a good approximation to the real area, goes to zero nicely as $n \to \infty$ and gives a tidy result. We can see that this area is something like a fraction $(2r - d)/2r$ of the area of the circle with radius r. r is given by

$$r = \frac{d}{2\sin(\pi/n)} \tag{3.8}$$

so that

$$A = \frac{2r - d}{2r}\pi r^2 = \frac{\pi d^2}{4}\left[\csc^2(\pi/n) - \csc(\pi/n)\right] \tag{3.9}$$

and thus the total area $A_t(n) = nA(n)$ is given by

$$A_t(n) = \frac{n\pi d^2}{4}\left[\csc^2(\pi/n) - \csc(\pi/n)\right] \tag{3.10}$$

We can now see that this argument will give us a joint distribution which agrees with simple considerations. Lewis' law states that there is a linear correlation between average cell area and topology, with large cells tending to have large topologies. We can see from the argument above that a small cell will have small d and thus $P_k(n)$ will grow at the expense of $P_u(n)$, thus tending to make small cells have less sides. Conversely large cells with large d will have a decreased $P_k(n)$ and an increased $P_u(n)$, leading to a peak at higher n. However we need an expression for the distribution of the area of the 'seed' cells, $Q_3(\alpha)$. We know that the circumcircle of the triangle must contain three points. The last point completes the triangle, and it must lie on the circumcircle (we in fact have all points lying on the circle because we assume regularity). So that we have

$$Q_3(\alpha)\, d\alpha = 2\pi d\left(\pi d^2\right)^2 e^{-\pi d^2}\, d\alpha \tag{3.11}$$

where d and α are related by

$$d^2 = \frac{4\alpha}{3\sqrt{3}} \tag{3.12}$$

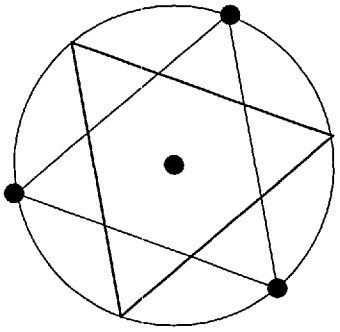

Figure 3.8: Initial cell

Thus we have now that

$$Q_3(\alpha)\, d\alpha = \alpha^{5/2} \left(\frac{64}{27} \frac{\pi^3}{3^{3/4}} \right) e^{\frac{-4\pi\alpha}{3\sqrt{3}}} \tag{3.13}$$

while

$$P_k(n) = e^{-(n\pi\alpha)[\csc^2(\pi/n)-\csc(\pi/n)]/(3\sqrt{3})} \tag{3.14}$$

and

$$P_u(n) = 1 - e^{-(n\pi\alpha)[\csc^2(\pi/n)-\csc(\pi/n)]/(3\sqrt{3})} \tag{3.15}$$

These expressions are then inserted into the following expression to give the final results

$$P(\alpha, m)\, d\alpha = e^{-4\beta\alpha} \left(e^{-\sum_{i=3}^{m-1} \beta i[\csc^2(\pi/i)-\csc(\pi/i)]} \right)^{\alpha} \left(1 - e^{-\beta m\alpha[\csc^2(\pi/m)-\csc(\pi/m)]} \right) \tag{3.16}$$

where

$$\beta := \frac{\pi}{3\sqrt{3}} \tag{3.17}$$

The form of this result is not all that one might wish, involving some rather awkward sums, however it does enable us to make some calculations. Using the joint distribution we integrate either area or topology to obtain the distribution over the other variable. In Figs. 3.9 and 3.11 we compare the results from Mulheran's simulation and model to our results.

Fig. 3.9 shows the results of simulation, Mulheran's model and our model for the topology distribution. Our model clearly does not compete with Mulheran's model in general. The tail of our distribution is far too fat, and stretches down to $n = 19$, twice as far as the simulation results. In a sample of 2×10^6 polygons Kumar and Kurtz found only two or three 15-sided cells. This tail has removed probability from the range around $n = 6$ leaving our distribution depleted here. The net effect of all this is to give us $\langle n \rangle = 7.2$ where we know that $\langle n \rangle$ must exactly equal 6. While this is not inconsistent, in that our model is concerned with a single cell and the constraint on $\langle n \rangle$ arises from cell-cell correlations, it is rather disappointing. This lack of cell-cell correlations seems likely to be behind the whole problem. Our assumption of regularity of cells corresponds to ignoring the random positioning of sites, and the detailed way they impinge on one another. Thus we are likely to overestimate the active zone areas.

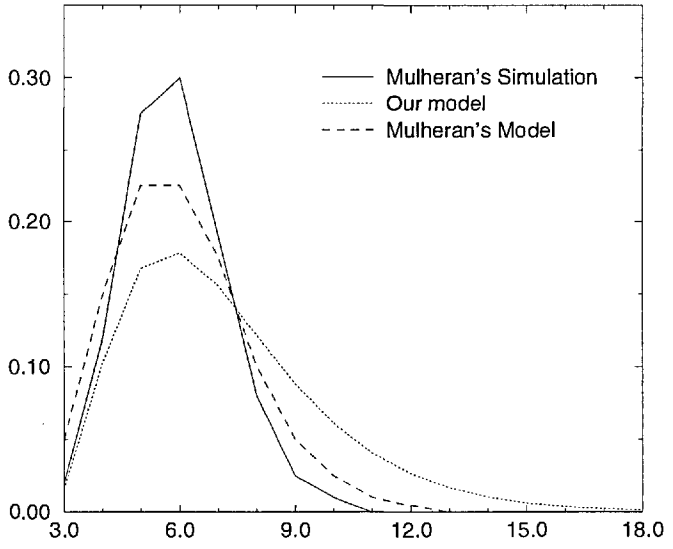

Figure 3.9: Cell topology results compared

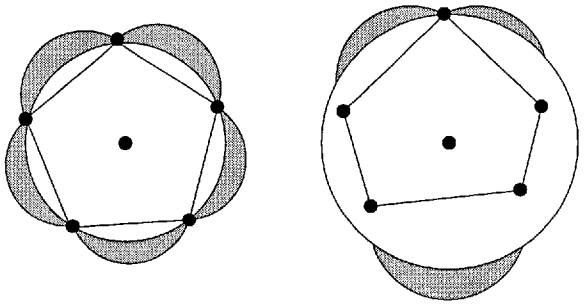

Figure 3.10: Irregular cell compared

For example, Fig. 3.10 shows two pentagons, one regular, the other irregular. We note that a similar method applied to the irregular cell yields a smaller active zone. The method once again consists of scanning for the next nearest neighbour and checking it for impingement on the cell. The active zone again corresponds to the area which must be empty for that neighbour to be irrelevant. Thus, if we could free our model of the regularity constraint it seems likely to fare better. There is however some good news here. Our model has a very good estimate for the probability of three and four-sided cells. Furthermore, the shape around $n = 6$ matches better than Mulheran's model, although the magnitude is out. We have $n = 6$ as the mode of the distribution.

Fig. 3.11 shows three sets of results for the area distribution. Weaire's formula is a good fit to his simulation data, and the other two curves are from Mulheran's and our models. This time our model comes out on top, with a very close comparison to Weaire's fitted curve.

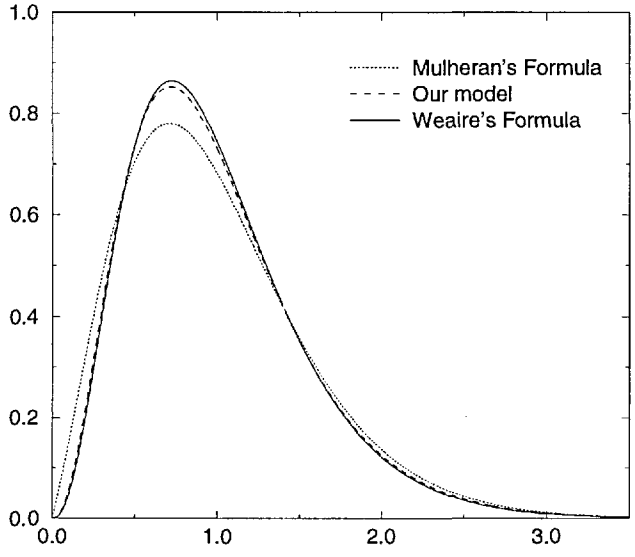

Figure 3.11: Cell area results compared

This is because our initial area formula is very close to his one parameter gamma distribution. Mulheran's curve is close, but has a linear start, and a long fat tail.

As mentioned above there is clearly a correlation between cell topology and area. Small cells will have small active zones, which are, therefore, more likely to be empty of additional sites. This implies that small cells will probably have relatively few sides. Similarly large cells are more likely to have many neighbours. Such correlations have been studied in real systems and simulations, and the correlations generally conform to a linear relation, known as Lewis' law,

$$\langle A_n \rangle = 1 + \lambda(n - 6) \tag{3.18}$$

Different systems have different values for λ, although there is some 'universality' in the values taken. Mulheran found that his simulations were well fitted by $\lambda = \frac{1}{4}$, and his model predicted $\lambda = \frac{1}{5}$. Our model does not give a perfectly linear correlation, Fig. 3.12, but is fairly close to linear. It is as close to linear as the experimental results at least. We find for our calculations that $\lambda \simeq 5.5$, which is close to the experimental findings, although inferior to Mulheran's results. Once again our deviation can be at least partly explained away by the underestimated active zone areas.

In Fig. 3.13 we show the cell area distributions of the different cell topologies. This tells a similar tale to Lewis' law, to which it is evidently connected. We see that as the topology increases the distribution shifts toward larger areas.

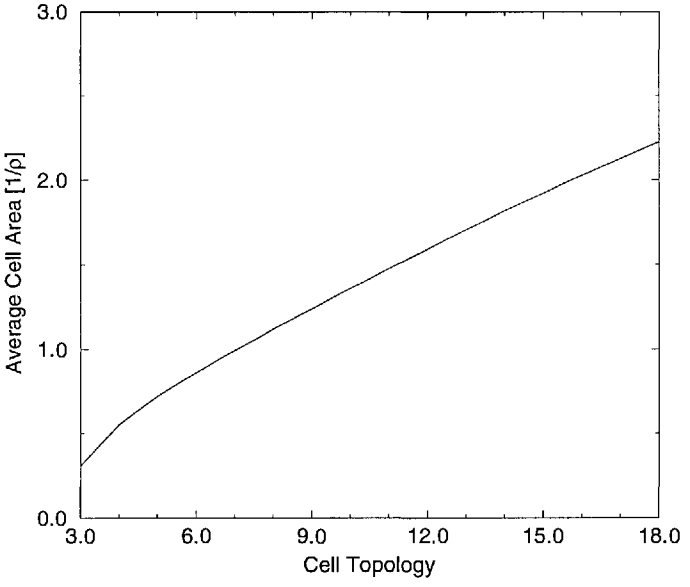

Figure 3.12: Average cell area vs. topology

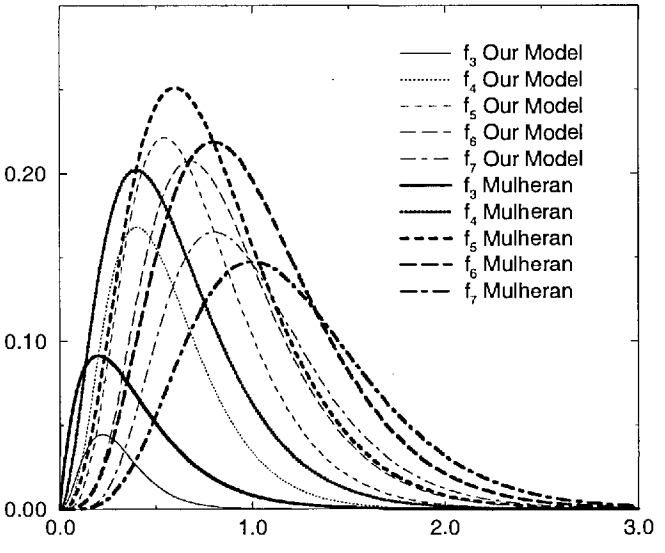

Figure 3.13: Cell area results by topology

Chapter 4

Vertex Ensemble Model

4.1 Basic motivation

In the summary at the end of Chapter 2 we noted that there is a need for a model of disordered foam which is sufficently abstract to allow us to increase our understanding of foam behaviour, whilst being sufficiently concrete to enable predicitions to be made to compare with realistic experiments. Our aim in this thesis is to develop such a model.

In physics when modelling disordered systems it is a common approach to use a probability distribution to summarise the available information. One does not attempt to explicitly model the whole system, as one does in a simulation, but chooses one element of the system as most 'important' and then describes the structure by the distribution over the configurations of this element. This was the approach used successfully by Beenakker and others as detailed in Chapter 2. We wish to now use their approach in order to develop our model of foam rheology and osmosis.

The models of Beenakker et al. used the cell as the elemental 'body' of the foam. This was useful for work on coarsening because the available rules with which to develop the model were von Neumann's law and some notions of cell topology correlations. Use of these rules enabled the models to be constructed and solved. The cell was subsequently adopted as the most important unit of foams and became ubiquitous in their study. Thus the models and simulations of Weaire and others concentrated largely on the behaviour of cells, until the work of Kawasaki et al. on the vertex dynamics of dry foams. Kawasaki et al. wanted to further simplify the models of foam structure in order to make larger simulations involving thousands of cells, and thus adopted a model with straight films and vertex dynamics only. However, due to their initial interest in grain growth they were in essence interested in the cells, and the vertices were modelled approximately, while the cell dynamics included were exact. This focus on cells is however problematic from the point of view of modelling rheology (and osmosis)

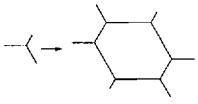

Figure 4.1: Constructing an irregular hexagonal foam from a vertex

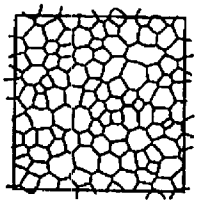

Figure 4.2: Foam sample

because the dynamics and variables describing the cell configurations do not lend themselves to calculation of the correct quantities.

We saw in the work of Kraynik et al. that the most convenient unit for the study of the rheology of foam is the vertex. In the course of their calculations they effectively used a vertex as a unit cell of the ordered foam, such a cell stores all the information required in order to calculate the rheological parameters of the system. To some extent it may seem that the film is an adequate unit; it is the films which form the vertex which actually determine the value of the stress tensor etc. However it is evident that without forming the films into a vertex we cannot apply the necessary constraints on them. It is the vertex structure of the foam which stops all films from lining up; it was the lack of this feature which restricted Derjaguin's model to the limit of infinitesimal strains.

We intend then to use the vertex as our primitive unit of foam structure. In addition to the above comments this fits into our notion of the physics of foam. Because the topology of the cells plays such a vital rôle in disordered foam we concluded in Chapter 2 that we would need to model foams such that,

$$Model \simeq Topology + \epsilon Geometry.$$

Any model which was based on cells would need to adopt the alternative approach because the topological correlations extend over large distances. By using the vertex we are choosing a unit with no topological degrees of freedom of its own. We then define the topology by defining its neighbourhood. In our model we will deal with the topological question by embedding each vertex in an irregular hexagonal foam in which it is the unit cell; we show the construction of an irregular hexagonal foam from a vertex in Fig. 4.1. We briefly recollect that an irregular hexagonal foam is a foam where all cells are identical irregular hexagons, that is not all their sides are of equal length.

The use of the vertex as the primitive unit also fits in with simple intuition about foam rheology and osmosis. Looking at Figure 4.2 we can see that as a strain is applied, say an

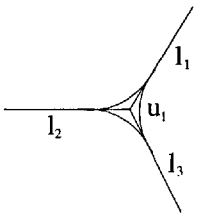

Figure 4.3: A vertex

extensional shear, the films will stretch in that direction and contract across the strain axis. However at some stage films will begin to reach very small lengths, at which stage they can undergo T1 events to create a longer film perpendicular to their original direction, decreasing the total free energy. This is the origin of the yield stress of foams. However the whole process is neatly described in terms of the dynamics of vertices; their surroundings move and force them to change configuration. At some stage they are forced to interact directly by a T1, but this event conserves the number of vertices and is just another feature of their dynamics. Of course the T1 events also affect the topology of the foam, which we have ignored in our model. However for the purposes of studying rheology the timescales are normally much shorter than those on which coarsening occurs (excepting creep), so that topology is irrelevant dynamically. This provides reinforcement for our proposition to model the vertices as embedded in irregular hexagonal foams, which also have no coarsening process. With regard to the osmotic properties of foam we see again that the topology of the cells is unimportant on the timescales we are interested in. Again the important configurational information concerns the vertices and the T1 events.

So let us define our model. We consider the most important unit of the foam to be the vertex, which we define to be a Plateau border (wet or dry) and the three half-films which 'belong' to it. Thus a vertex is defined by a liquid volume (the fluid resident in the Plateau border), an orientation (defining which way the films point), and the three lengths of the half-films. A vertex is shown in Fig. 4.3. We are interested in phenomena which occur on a timescale short compared to that of coarsening, so that we expect the topology of the cells and the gas flow between cells to be unimportant; we therefore consider only straight (as opposed to curved) films. We are interested in typical experimental foams, which are observed to be fairly homogeneous, so that an exact spatial description seems inappropriate. We therefore model the foam by a probability distribution over the configuration space of vertices. Because of the unimportance of coarsening, and the need of some neighbourhood constraints on the vertex, we embed each vertex in the irregular hexagonal foam formed by it as unit cell. As we have decided to abandon any attempt to exactly model the spatial behaviour of the bulk of the foam we need to make some assumptions as to how we will apply deformations to our conceptual sample. This problem is neatly solved for us by the assumption of periodic embedding. For such hexagonal

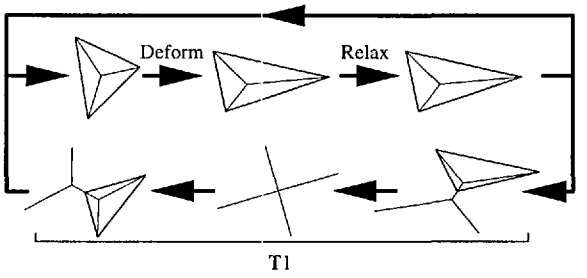

Figure 4.4: Full vertex map

foams [81] the deformation of vertices is affine for both extensional and simple shear. The similar problem for osmotic study will be discussed in Chapter 6. Thus we have a distribution which evolves under a map defined by the relaxation dynamics and the deformation, we call this map F_D. We can observe the evolution of the foam sample in the evolution of the distribution. We make quantitative predictions by using the distribution to calculate expected values which will be predictions of experimental values, for quantities such as the stress tensor and viscosity.

4.2 Vertex map

There are several ways of looking at this model, and some alternatives are illuminating. The way in which we have described it above we think of a distribution, a continuity equation and an evolution equation, and we imagine integrating smoothly over time to obtain the evolution of the distribution. From the distribution we can then obtain any other quantities, such as the stress tensor, which we are interested in. From this point of view we cannot talk about a particular vertex' evolution. However, if we return to the roots of the model, which lie in the approach of Beenakker, we can develop a more intuitive picture which can enable us to improve our physical picture of foam evolution.

Beenakker solved his model by running simulations using large numbers of conceptual cells. If we apply the same approach to our model we can replace the distribution with a large ensemble of vertices. Such an ensemble could be created in several different ways. Firstly we can capture the distribution of vertices in a real foam, say by digitizing a picture of a sample. Alternatively we could do the same with a simulation sample. In this case we choose the second approach and relax a Voronoi diagram under the film dynamics, and then split it into its constituent vertices. So we have our initial ensemble of vertices now; as above, each vertex has an orientation, a liquid fraction and three half-film lengths, or, equivalently, three half-film vectors (not fully independent) and a liquid fraction. Each vertex is embedded conceptually in an irregular hexagonal foam and thus feels the same deformation as the bulk sample, imposed on the triangular unit cell which contains it. As the triangular cell is deformed the vertex inside changes its configuration so that it stays at equilibrium, with the film forces in balance. If we

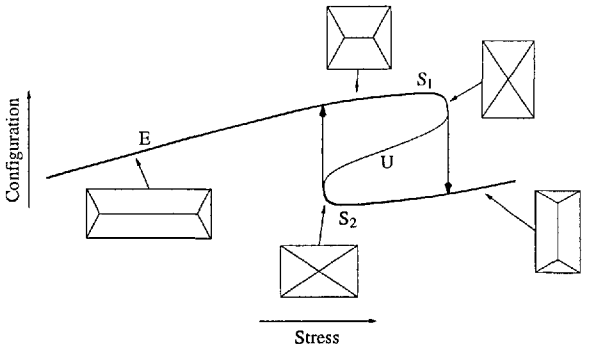

Figure 4.5: Embedded vertex undergoing T1 event

imagine modelling this numerically, integration is replaced by evolution through small discrete steps. We can picture a typical vertex evolving under such a system (see the upper part of Fig. 4.4); first a small but finite deformation is applied to the triangular cell. If the films were to retain their position so as to deform with the cell then they would be out of equilibrium, as shown in the center panel. The dynamics of the films intervenes to relax the vertex to a new equilibrium configuration. This defines a map on the vertex configuration space, which moves vertices in small jumps. We call this the vertex map, $\mathcal{F}_{\mathcal{D}}$. The continuous part of the map is defined fully in Appendix B.

However the map is not yet fully defined. As we noted in Chapter 2, as the neighbourhood of a vertex is deformed it may be forced towards a catastrophe, where it suddenly has access to a much lower energy configuration; this is a T1 event taking place. We show the catastrophe again in Fig. 4.5. Thus the map also contains discontinuous jumps in the configuration space which arise as films disappear, causing T1 events which change the vertex suddenly. If we use the 3 lengths, orientation and fluid volume as coordinates in the configuration space then we find that the space has a curious structure. The fluid volume u_l gives us a half-space, with a boundary at $u_l = 0$. Likewise the three lengths give half-spaces, and it is at these boundaries that T1s and thus jumps occur. The orientation rather complicates matters, but we can define it by the angle between one axis and a particular film, and then identify the three points corresponding to different choices of film. The vertex map is continuous in the volume defined by the boundaries, but is discontinuous at the (length= 0) boundaries. Thus vertices move on smooth trajectories (or orbits) in the bulk space but jump when they collide with the boundary, which gives absorbing boundary conditions with source regions in the bulk space. The source regions are four dimensional hyper-surfaces in the five dimensional configuration space. A schematic diagram of the system is shown in Fig. 4.6, the curve C is a source hyper-surface.

The catastrophe therefore induces a discontinuous part to the vertex map $\mathcal{F}_{\mathcal{D}}$. The relation between the point at which the vertex strikes the boundary and the point it jumps to in the bulk (the corresponding source point) is determined by a set of rules. These rules merely

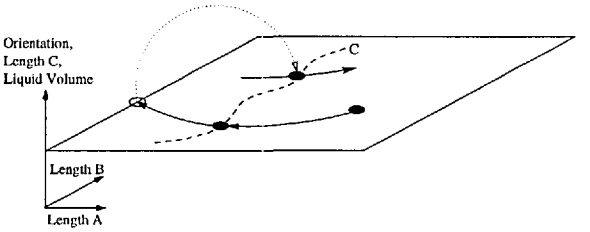

Figure 4.6: Behaviour under vertex map

encapsulate the way in which a T1 takes a short film in one direction into a perpendicular film. The rules are set out in detail in Appendix B.

4.2.1 Quasistatic Vertex Map

The map as described above is general and covers many situations. In this thesis we consider two specific examples of foam out of three important ones. The areas of interest in modelling foam rheology are the abstract but simple dry foam, with no forces other than surface tension, the more realistic viscous foam, where viscous forces arising in the thin films are also included, and closest to nature, the wet foam, with thick fluid films. The two examples we consider are the first two, dry and viscous foams.

For dry foams the map above is made specific in the following way. The only forces acting are those of film surface tension, which implies that all films meet at common angles of $2\pi/3$ radians. When one film reaches length zero this constraint can no longer hold and the vertices search for a new configuration. This configuration can be found using the rules mentioned above. The change is instantaneous within the model, because the present configuration is unstable, and the corresponding stable configuration has a third non-zero film. Such an instantaneous change presents no great problems in the model because there are no viscous forces to oppose such motions.

In Fig. 4.7 we show a vertex evolving under the vertex map defined by a dry foam dynamics and an applied simple shear. Similar diagrams, but showing how the vertex fits into the foam bulk are shown in Kraynik and Hansen [81]. We term such a trace the 'orbit' of the vertex under the vertex map.

4.2.2 Vertex Map with Viscosity

For viscous foams the map is made specific in a slightly different manner. Now we have additional forces acting which may give rise to different forces in different films. Because of this the vertices at equilibrium will not in general have an equiangular structure. This implies a different looking set of vertices, but the same basic constraints apply. When a film reaches zero length the same rules are applied in order to find the new film configuration. However the

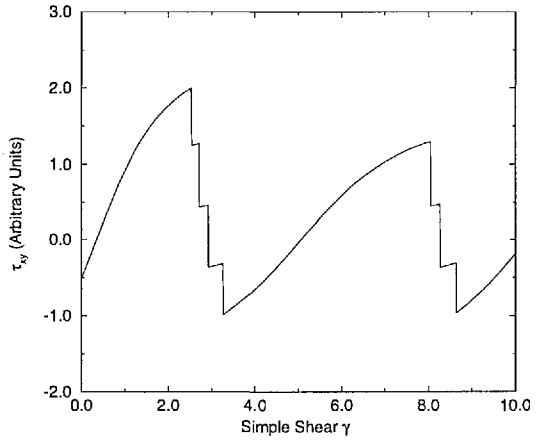

Figure 4.7: Vertex orbit — dry simple shear

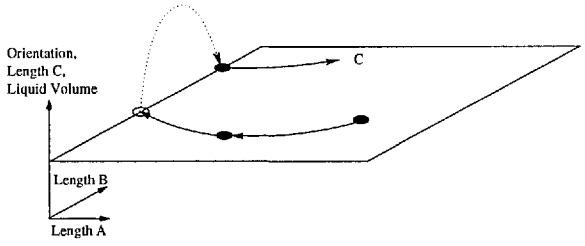

Figure 4.8: Behaviour under viscous vertex map

changes do not take place instantaneously as their rate is determined in part by the viscous forces in the flipping film. This means that there are in fact no discontinuities in the length of the films for the viscous foam map, although the vertex still moves very rapidly in this segment of its orbit. Note however that there are still discontinuities in the vertex orbits; the sudden topological change when a film flips alignment corresponds to a jump of the vertex along the length= 0 boundary as illustrated in Fig. 4.8.

4.2.3 Wet Vertex Map

We will not consider the wet vertex map further here, because so far we have not been able to obtain useful results. The map shares most of the structure of the viscous map; the same topological discontinuities, and lack of length discontinuities. This similarity is because the picture of a dry skeleton plus wet decorations mentioned in Chapter 2 is applied. The lack of results is due to the difficulty of calculating the configuration of the curved film segments, which makes the calculations much more time consuming.

4.3 Calculations and Quantities

Now we need to briefly describe the manner in which we obtain quantitative results from our models. The foam is represented by a probability distribution over the configuration space of vertices. Therefore we obtain values for the variables which we are interested, such as stress tensor, osmotic pressure and viscosity, by taking expected values over this distribution. In terms of the ensemble of vertices this corresponds to adding all their individual contributions. The full details are given in Appendix B.

In order to compare the results to experiment we need to model a specific material sample, which means incorporating material constants. Foams are typically characterised by four parameters. The first is the surface tension of the surfactant films σ, the second is the average cell diameter before deformation $\overline{d_I}$ (or average film length $\overline{l_I}$), the third the viscosity of the films , and the fourth is the gas volume fraction which we shall not need to include as our work here assumes the dry foam limit $\Phi_g \to 1$.

In this work we will use a recipe in [125] with $\overline{d_I} = 100\mu m$ and $\sigma = 2.2 \times 10^2 Nm^{-1}$. The model calculations are performed with $\overline{l_I} = 1$ and $\sigma = 1$, so to dimensionalise we multiply by $\sigma\overline{l_I}$. This gives τ per vertex, so we multiply by ρ_V, the number of vertices per unit volume where

$$\rho_V \sim 2\rho_C \sim 4\left(\pi\overline{d_I}^2\right)^{-1} \tag{4.1}$$

with ρ_C the number of cells per unit volume.

Chapter 5

Vertex Ensemble Model applied to Two-Dimensional Foam

5.1 General Comments

Now we examine the predictions of the vertex ensemble model. By using the ensemble picture we can visualise the behaviour of our theoretical sample under deformations.

As we apply a deformation the distribution of vertices will alter so as to resist the applied strain. The strain field acts on each vertex and causes it to align in some sense to the instantaneous local strain axis, with the longest films tending to lie along the axis. This leads to the form of the stress tensor, with a net force opposing the strain. We expect that this will be a fair prediction for the reaction of a real foam sample, although we would expect our calculations to generally overestimate the forces. This is because there are no correlations between vertices in our model, which means that the vertices are freer to move than in the real foam. Such constraints seem likely to slightly lower the net force the sample can muster to oppose the strain.

We will start our examination of the results of the model by considering the evolution of a sample under the effects of simple shear. This allows us to see the success of the model, and to examine how it works more closely.

5.2 Dry Foam under Simple Deformations

5.2.1 Simple Shear

Simple shear does not occur generally in real flow situations, but it is a good approximation to many deformation gradients and is simple to model. It is therefore one of the cases most often

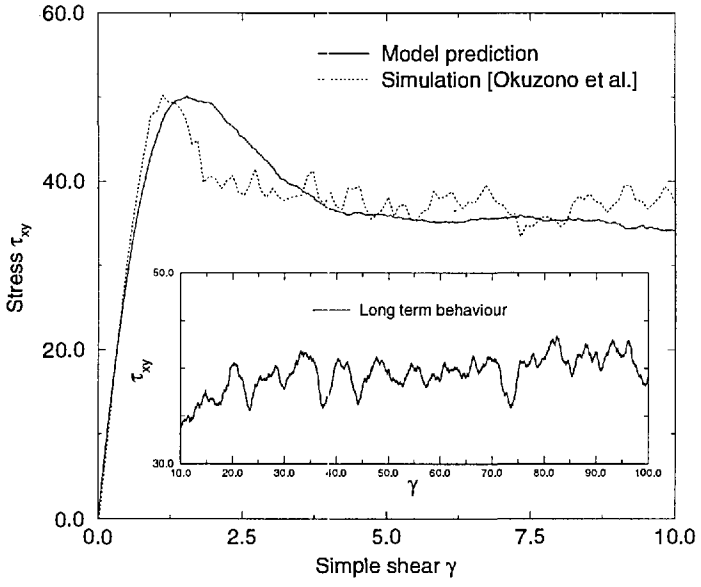

Figure 5.1: Calculation for simple shear of dry foam

considered when constructing theoretical models of fluids.

As we discussed in the previous chapter simple shear is applied across the whole sample and the individual vertices feel the same deformation as the bulk. First of all we present the main result and then we shall examine what the model tells us about the way in which foam acts, and how the shear response is built up. In Fig. 5.1 we show the model calculation of the stress-strain relation under simple shear. The results are universal as the model has only two parameters for a dry foam, the surface tension σ and the mean bubble size d_0. The graph here is for the recipe given in Chapter 4.

We note immediately the presence of the various features which we discussed in Chapter 2, the initial elastic response, the yield stress and the plastic flow regime. The elastic modulus obtained from our model is of course very close to the elastic modulus of Kraynik et al. [81, 57], because the stress-strain curve up to the first T1 is independent of orientation. From Khan and Armstrong [57] we can see that the prediction for ordered foams for the initial elastic regime is

$$\tau^e_{xy} = \tau_{xy}|_{\gamma\to 0} = -\frac{\sigma}{3a} \tag{5.1}$$

where a is the hexagonal side length. From our model we obtain a τ^e_{xy} of $-0.22\frac{\sigma}{l}$, where l is the average film length. The deviation is due to the distribution of asymmetric vertices, which means there is no true elastic regime.

The yield stress is clearly present, though it highlights the difficulties discussed in defining the yield stress. The foam initially yields at the end of the elastic regime giving the first yield stress. However, this is the highest value of the shear stress, as it subsequently decreases

almost linearly to the steady state value, which is approximately 70% the peak value. This linear decrease is a feature which we did not discuss before, and is perhaps slightly unexpected, but which is born out in numerical simulations. The results of Kawasaki et al. [93] are shown in Fig. 5.1 in comparison to our calculations, and show clear agreement both qualitatively and quantitatively. Similar features can also be seen in the results of Weaire et al. [56] which are noisier but are from more 'accurate' foam simulations.

We obtain for the steady state yield stress, that is well into the flat plastic regime, $\tau_{xy}^{y} = 0.24\frac{\sigma}{\pi l}$.

Some discussion of the errors in the predictions is necessary at this stage. The errors in the calculated figures are of the same order as the noise which is visible on the curves. This is around 1% of the figures themselves. Thus, the quantitative and qualitative features of the curves are quite definite, and stand out clearly from any noise. Nevertheless this expression for the noise must be treated carefully as, as will be explained below, the noise seen on the predictions is not gaussian noise.

One of the key features of the vertex ensemble model is that it gives us some physical feeling for the origins of the stress-strain relations. The initial state of a foam is clearly not similar to the state of a strained sample. Strain defines a unique axis for the previously isotropic foam. For simple shear the axis slowly rotates in the direction of the applied shear, for extensional shear the axis is fixed. The foam is stressed along this axis, and can relax perpendicular to it. Thus, the stress tensor has a large component in this direction, and the bulk of the foam must align along this axis. So as we strain the sample (or ensemble) the vertex distribution shifts to align.

The initial state of the sample is isotropic, and in some sense the vertices are correlated, although any vertex configuration is possible in the initial sample (that is to say that stress only affects the distribution of vertices, the actual configurations accessible to individual vertices are in no way affected) the distribution is concentrated on those vertices with isotropic stress tensors. Because some vertices will undergo T1s immediately we see that there is no absolute elastic regime as we know from observing real samples. However, because the distribution favours isotropic vertices (those with isotropic stress tensors) we have a short regime where the behaviour is effectively elastic.

As the strain proceeds the distribution changes until eventually it reaches a stage where it is invariant under the deformation. We expect this because we know that vertices are not stable under the simple shear, there are no configurations which do not undergo T1 events at some stage, so we expect a flow of vertices to be set up. Vertices will align to the strain axis and then jump away as they undergo T1s, to then align again and so on. The basic mechanism is shown in Fig. 5.2.

The regime where linear decrease in 'yield stress' takes place is the transition between these

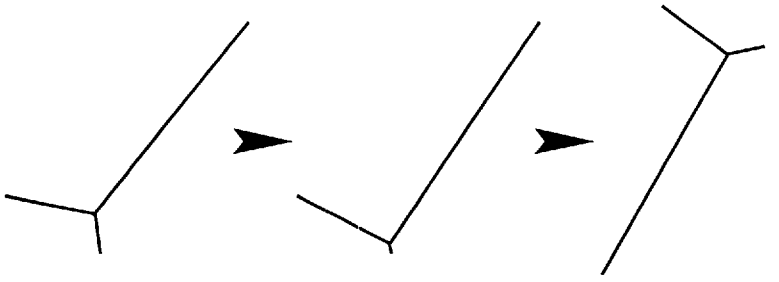

Figure 5.2: Vertex hopping under simple shear

two modes.

Inset in Fig. 5.1 is the longer term behaviour of the foam. We note two features; firstly that the curve is noisy and that this noise is not white noise, we shall return to discuss this below in Section 5.5. The second feature is that there is a slight increase from $\gamma = 10$ to $\gamma = 100$. We should note that these values of γ are not realistic physically, that is they are not likely to arise in a flow scenario. Nevertheless, the origin of the effect is clear. As the sample is sheared the local strain axis is shifting, and shifting at a decreasing rate. Thus, the vertices are better able to align themselves to the axis and the total stress opposing the strain is increasing slightly.

Now we consider briefly the way in which the response is built up from the orbits of individual vertices. In Fig. 5.3 we show the individual stress orbits for vertices in a small ensemble. These vertices have been chosen with equal length films and are rotated at 0, 6, 12, 18, 24, 30, 36, 42, 48, 54 degrees to the vertical. The sum of their stress orbits is shown, this is the sample stress orbit in the ensemble picture. We can see that the point at which a vertex undergoes its first T1 depends only on the ratios of the film lengths, and that vertices with all films of equal length must be the last to undergo T1s. We also know [57] that the last vertex of this kind to T1 is the one oriented at 45 degrees, this vertex undergoes a T1 at a strain just under $\gamma = 4$. So by the time $\gamma = 4$ all vertices must have undergone at least one T1, so that the foam has really started to flow plastically. This is why the real plastic regime is entered around $\gamma = 4$, as is apparent in Fig. 5.1. It is apparent that even a small ensemble soon begins to show the features of a real sample, that is that the individual features of the orbits cancel out to produce the aggregate behaviour.

We should briefly discuss the cascades of T1s which are apparent in Fig. 5.3. It may seem somewhat inconceivable that a vertex can go through such a repetitive run of events without moving to another, quieter, area of configuration space. This occurs because one film is long compared to the other two; this long film pins down the configuration of the vertex. Thus when a T1 event occurs the film which had zero length cannot gain much length in the rearrangement and the system remains near to the catastrophic zone. It is unfortunately rather hard to quantify this statement, but an illustration of the motions of a vertex during a cascade is given in Fig. 5.4. The crossed lines show the position of the actual vertex which has been

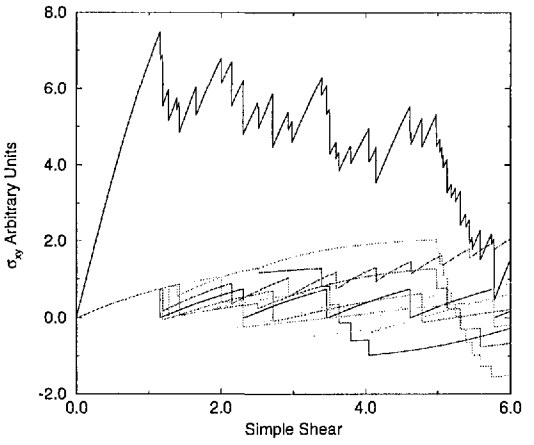

Figure 5.3: Vertices individual stress orbits

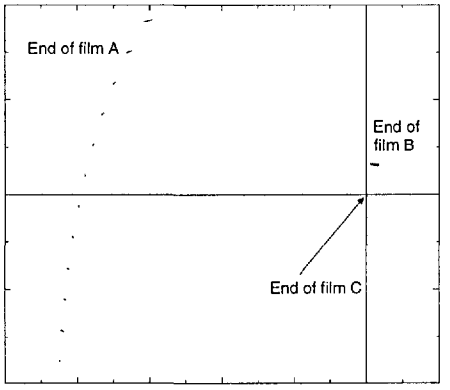

Figure 5.4: Motions of a vertex in a simple shear cascade

kept fixed; moving relative to this are the points marking the ends of the half-films. It is clear that one film is relatively long. The cascade of T1 events is clear in its effect on the endpoint of this film. The other endpoints are pinned down near the vertex, especially the lower one which is hardly separable from the vertex point.

5.3 Extensional Shear of Dry Foam

Next we consider the effects of extensional shear. This is the second commonly studied situation in foam flow. The vertex ensemble predictions for the stress-strain relation for extensional shear are shown in Fig. 5.5, with a magnified look at the steady state response inset. The form of the curve is notably different from Fig. 5.1, with only two regimes apparent, the elastic and the

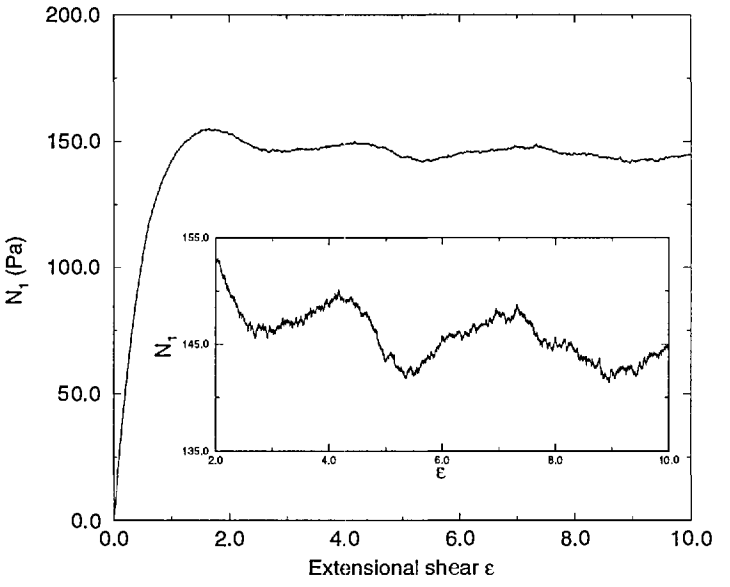

Figure 5.5: Extensional shear prediction

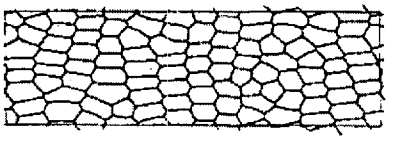

Figure 5.6: Simulational sample under extensional shear

plastic. This agrees fairly well with the simulation results of Weaire et al. which are, however, rather noisy. Another possible agreement is the fairly definite oscillations along the steady state response. Similar structures are apparent in the results of Weaire et al., but there they are hidden amongst noise and could have been discounted as such. In our calculations however, they show quite strongly with an amplitude of about 7% of the yield stress.

Once again the elastic regime predicted by our model is fairly close to that predicted by Khan et al. [57, 81], where

$$N_1^e = N_1|_{\epsilon\to 0} = -\frac{4\sigma}{a\sqrt{3}} \tag{5.2}$$

where a is the hexagonal side length. From our model we obtain a N_1^e of $-2.4\frac{\sigma}{a}$.

The yield stress N_1 is not ambiguous in this case because there is almost no change in the plastic regime. The value we obtain is in good agreement with that of Weaire et al. The oscillations do however, require some explanation. A plausible argument arises from examining the structure of the deforming foam. Under extensional shear the strain axes are fixed, with the foam sample being stretched along one axis and shrinking along the perpendicular axis. Thus the vertices tend to align, with one long film along the stretching axis and shorter films

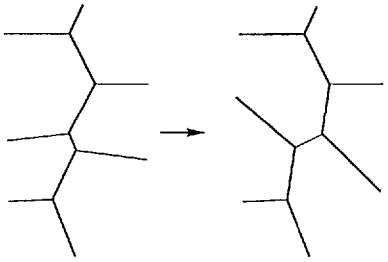

Figure 5.7: Zipper structure evolving

across the axis. Extensional strain therefore leads to concentration of the vertex configuration distribution on the area of configuration space corresponding to this alignment. We observe this concentration in our model, which leads to a lower entropy for the system (using a statistical interpretation of the entropy $H = \int p(x) \log p(x) dx$) which naturally corresponds to an increase in the inherent order of the system. In experimental and simulational samples, an example of which is shown in Fig. 5.6, the alignment of vertices leads to a more ordered arrangement of cells, as has been noted in Weaire and Fortes [56] amongst others, as we showed in Chapter 2 this has the effect of lowering μ_2, the variance of the topology distribution, which again naturally corresponds to a lowering of entropy and increase in ordering.

So as we impose extensional strain the vertex distribution contracts towards the aligned configuration. Naturally though in such a disordered system all vertices do not converge at the same rate, and there will always be a small fraction of vertices distributed across the whole configuration space. As the distribution contracts the individual vertices converge towards the one perfectly aligned state. This state has the long film exactly aligned with the strain axis. Once in this state the vertex is pinned, and the the only further change of configuration is an increase in the long film length and decrease in the lengths of the short films. As the vertices converge towards this state, they are in states which have one long film aligned almost along the axis, and shorter films asymmetrically placed away from the axis. Such states have one short film shrinking at a faster rate than the other, which means that they are unstable in the sense that they undergo T1 events, but do so at a low rate.

In the real sample we can see the ordering reflected in the 'zipper structure' of the foam. Zig-zags of short edges run from top to bottom of the sample, joined by long almost horizontal films, to form a hexagonal cell structure. We term these zig-zags zippers. If the structure were perfectly aligned then no further evolution would occur, but the films are not exactly aligned, which means that some of the films in the zippers slowly get shorter. When a film reaches zero length a T1 occurs, which leads the zipper to split into two (hence the name), as shown in Fig. 5.7. This leads to a periodic development of the sample as zippers slowly increase in number.

Thus we can see the same underlying behaviour in both systems, abstract and real. We can

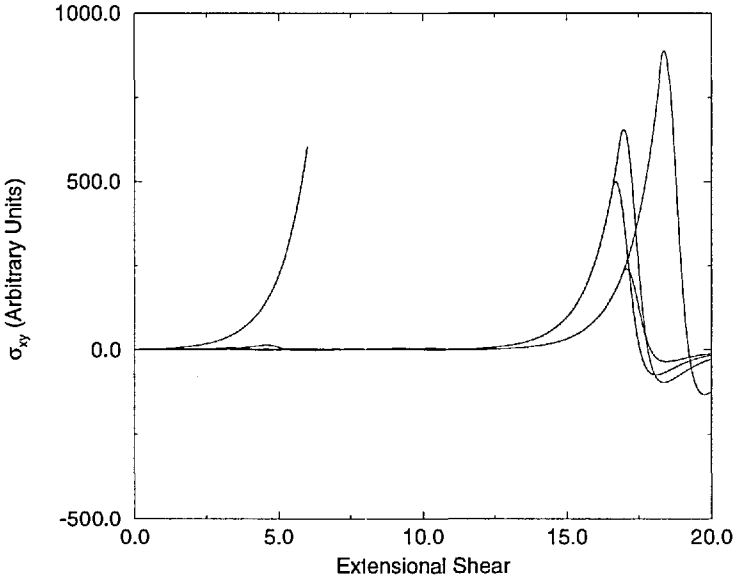

Figure 5.8: Exponential contributions

see that the dynamics of the vertices is the same in both cases; indeed we would expect the VEM model to correspond most closely to reality in this example, because in the sample each vertex is very close to being surrounded by copies of itself, i.e. the foam really is almost ordered-hexagonal. We can see the origins of the behaviour in 5.9 where we show the contributions from individual vertex orbits in a small ensemble. It is clear that there is a significant contribution with a periodicity in the range of $\Delta\eta \sim 3.0 - 4.0$.

Unfortunately this mechanism also prevents us from studying the long term behaviour under extensional shear using our model. The distribution converges on the area around the orbit shown in Figs. 2.29 & 2.30. These orbits have exponentially increasing N_1 and soon dominate the calculation. This is unphysical, as we can see in Fig. 5.7 the interaction between vertices in a real sample causes more scattering of vertices around the vertex undergoing a T1 which disorders the foam and diminishes this effect. However, the values of ϵ at which this happens are of order 100 which is not a regime of realistic application anyway.

5.4 Experimental Calculations

Next we turn our attention to more concrete situations, which correspond to actual experimental measurements. In Chapter 2 we outlined some of the more common apparati used to collect rheological data. Here we make calculations for the response of dry disordered foams in two of these apparati for which experimental measurements are available in the literature, namely the rotary rheometer in both steady and oscillating strain.

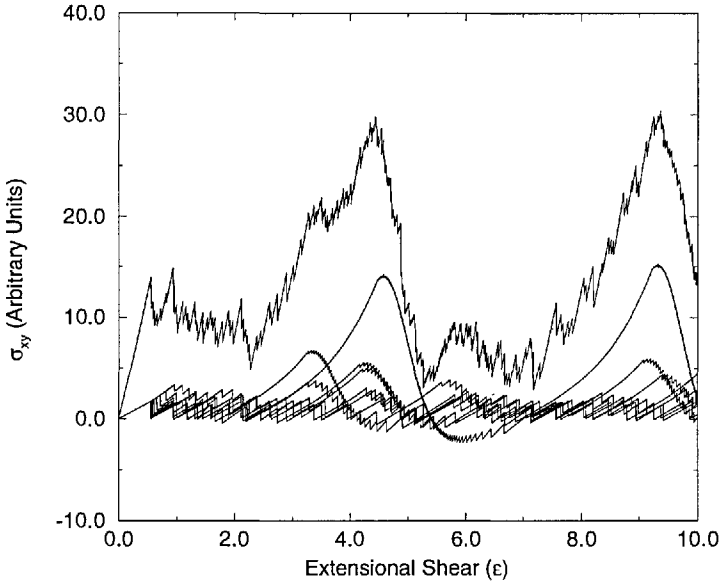

Figure 5.9: Small ensemble under extensional shear

5.4.1 Rotary Rheometer

Khan and Armstrong [56, 125] performed experiments using a rotary rheometer to ascertain various rheological parameters. Here we are interested in their measurement of the torque required to produce a certain rim shear, see Chapter 2 for definitions.

Our calculation is done in the same way that interpretation of the experiment is usually carried out. We simply integrate the torque produced by each cylinder of foam to find the total torque. The strain at radius r is given by

$$\gamma(r) = \gamma_R \left(\frac{r}{R}\right) \tag{5.3}$$

where R is the radius of the rheometer disks and γ_R is the value of the strain at the rim also known as the rim shear. Thus, the total torque T is given by

$$T(\gamma_R) = \int_0^R dr\, 2\pi r h \cdot r\tau_{xy}\left(\gamma(r)\right) \tag{5.4}$$

where we use the values of $\tau_{xy}(\gamma)$ we have calculated previously.

These values are in good agreement with the experimental measurements carried out by Khan and Armstrong. They agree both in order of magnitude and in functional form. Our results are an overestimate of approximately 15%, averaged over the calculated region, and the curve plainly has the same overall shape with a linear regime evolving into yield as the yield surface moves inward. This agreement is good considering the simplicity of the model. As we expected the calculation is an overestimate of the physical torque, due the unconstrained

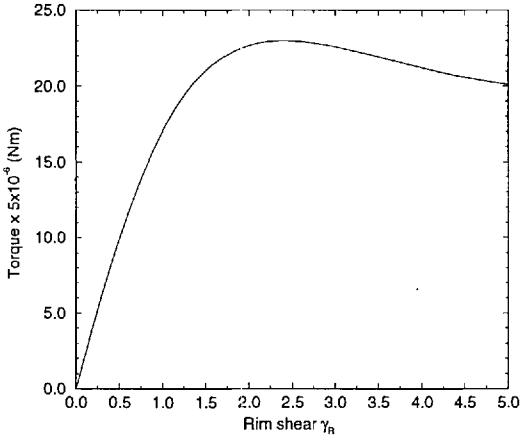

Figure 5.10: Predictions for dry foam in a rotary rheometer

motions of vertices in our model. Real vertices would be more highly correlated due to the residual geometrical order in the foam. Furthermore the cylinders of foam are not of course disconnected as is assumed in the calculation, so that the yield surface is not a true surface but a region in which the deformation is more complex.

5.4.2 Oscillatory Shears

The second experimental prediction made using the model refers to oscillatory shear in a rotary rheometer, an experiment carried out by Yoshimura and Prud'homme [66]. Although their experiments concerned the dependence of yield stress on strain rate, which we consider when we discuss the inclusion of viscous forces, we first consider the predictions of our simple model. In Fig. 5.12 is a plot of our prediction for the shear stress during oscillatory simple shear. The form can be compared to the results shown in Fig. 2.22 from [66] Yoshimura and Prud'homme. Clearly the basic form is the same, with higher amplitude oscillations developing a flat top as the yield strain is reached. The thumb on the left hand side of the peaks is not yet understood, nor observed experimentally. We have not attempted to plot the phase angle against the maximum stress as Yoshimura and Prud'homme did, but we note that the overall motion of the peak is in the correct direction (Fig. 2.21).

In Fig. 5.11 we show two individual vertex orbits. We note that the orbits are periodic, as all vertex orbits are under oscillatory strain.

5.5 Self Organized Criticality

Kawasaki et al. [94] have recently developed their vertex model to model foam rheology with the deformations applied using the periodic boundary conditions of the model system. This cor-

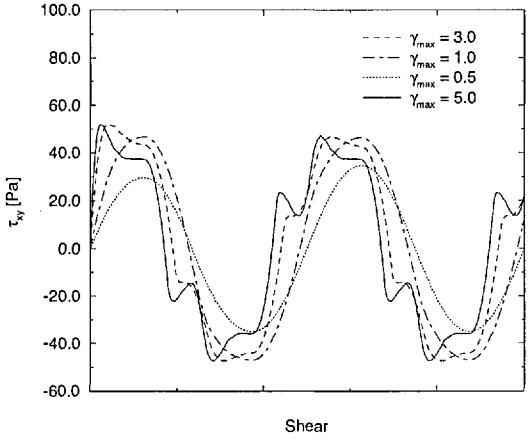

Figure 5.11: Calculated τ_{xy} for oscillating simple shear

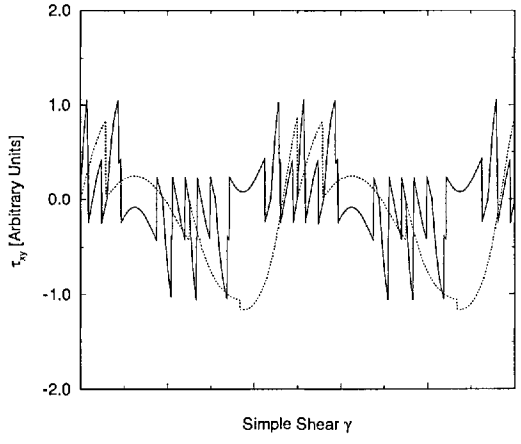

Figure 5.12: Individual orbits under oscillating simple shear

responds in some sense to real deformations which are felt by the sample only on its boundaries and which propagate into the sample by the same mechanisms which make up the rheological behaviour of the system, as opposed to the manner in which deformations are generally modelled at present as homogeneous affine deformations.

The results of this latest vertex model are interesting in many ways. Primarily they agree with previous work, and indicate that the approximation of affine deformation is a good one. Snapshots of the simulation sample indicate that the foam remains fairly homogeneous at the strain rates which the model covers. However, this approximation does break down when it comes to the detailed dynamics of the vertices, and the more refined model exposes the effects of vertex correlation to scrutiny. Furthermore the vertex model allows much larger samples (of up to 1000s of cells) which means that the signal to noise ratio of the simulation traces is far superior to the more physical simulations of Weaire et al.

The main result of this work is to show a surprising structure in the evolution of foam. The simulation sample is seen to have a punctuated dynamics similar to the processes used to describe earthquakes and sandpiles. The similarity is evident, a system composed of many independent parts, with static and dissipative forces involved, and under an external force. The result is the kind of behaviour commonly known as self-organized criticality (SOC). An SOC system typically evolves into a regime where it constantly occupies a critical state, where the external force causes some kind of sudden change in the configuration — the crucial feature is that the magnitude of the change has a power law distribution. Thus, the system has a scale invariant evolution.

The most commonly studied example [96, 95] is the sandpile, made famous by Bak et al. Although the sandpile is not exactly the one of common experience it is very close. Sand is 'dropped' on to one end of the pile, and a set of dynamic laws is defined which summarize the sand behaviour. Thus, sand particles can stick, but the shear strength of the sand is low, giving rise to a hopping probability which depends on the number of neighbours bearing down on a particle. If one starts with a flat pile the sand slowly accumulates until it has a slope corresponding to its coefficient of friction, at this stage avalanches begin to occur. As mentioned above the avalanches are characterized by a power law distribution, which implies that they occur on all length scales. The basic phenomenon is well documented and intuitively grasped although no precise derivations of the exact origins are known.

The parallel with a strained foam sample is immediate. A sample is placed under simple shear. At first the vertices adjust and align to the local strain axis. In foam T1 events play the rôle of hops, and energy plays the rôle of sand grains above. Thus, energy is poured into the system in the form of stress on the sample, and is dissipated away by T1 events, just as sand was transported away by hopping. As the strain increases the foam approaches the SOC regime, this regime is entered more or less at the yield stress. At this point the T1 avalanches

begin, operating in the same manner as above. One T1 releases local stress, but may increase local stress on neighbours causing them to undergo T1s and so on. Once in this regime the foam maintains a fairly constant stress concentration and rate of T1 activity, so that it is in a critical state, and so may also be expected to show power law distributed avalanches. This is indeed the case as demonstrated by these simulations. Kawasaki et al. found strong evidence for power law distributions of both the energy release and stress release in these avalanches, as well as power law spectra for the energy and stress time series.

They also clearly observed the geometrical evidence which goes with SOC behaviour. With their simulation they track the motions of each vertex, that is each Plateau border, in the sample. By plotting the velocity of each vertex the nature of the punctuated dynamics becomes clearer. Each avalanche shows up as a vortex-like rearrangement of vertices, with a large range of sizes visible. The largest avalanches clearly involve the whole sample in one large vortex. Such flows are shown in Fig. 2.42.

The question arises as to what kind of spectra the stress and energy time series have in the vertex ensemble model. Naturally there are no such features as avalanches in the model, and similarly power law spectra were not expected as the model does not contain the vital ingredient of SOC systems, local correlations. In the vertex ensemble model each vertex goes its merry way oblivious to its neighbours, because it has no defined locality. However, it was a valid question because the similarities between the calculated predictions of the vertex ensemble model and the vertex simulations were so clear.

The only way to compare the two models is by using the power spectra of the shear strain curves. This is because our model can't have the 'classical' SOC behaviour, so that we can't measure, for example, the probability distribution of different avalanche sizes. The power spectrum is defined by

$$S_X(\omega) = \lim_{T\to\infty} \left\langle \frac{2\pi}{T} |X_T(\omega)|^2 \right\rangle \tag{5.5}$$

$$X_T(\omega) = \frac{1}{2\pi} \int_{-T/2}^{T/2} x(t) e^{-i\omega t}\, dt \tag{5.6}$$

Thus to calculate it for our model we clearly take the limit at finite T, after squaring the modulus of the Fourier transform of the time series data. This is the same technique as used by Kawasaki et al. Surprisingly the spectra taken from the plastic flow regime of the vertex ensemble predictions show a power law distribution similar to theirs, although with a different slope. Our data gives a spectrum $S_{\tau_{xy}} \sim \omega^{-4.2}$, see Fig. 5.13, where Kawasaki et al. have $S_{\tau_{xy}} \sim \omega^{-2.0}$, so the exponents are not close, however we are seeing the presence of a scaling spectrum.

Now, however, a harder question arises: How can a model with no correlations reproduce the features of a model exhibiting SOC behaviour, including the tell-tale power law spectra. This question is made more interesting by the continuing lack of firm agreement on the underlying

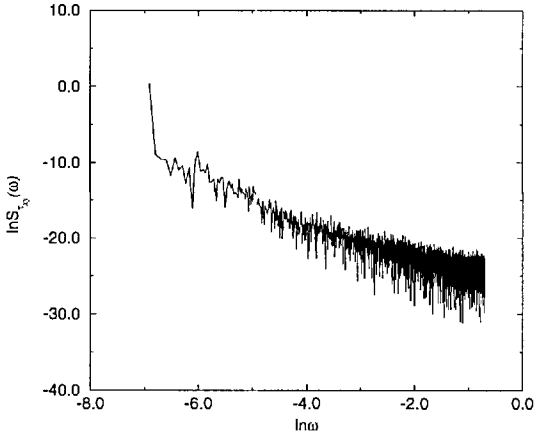

Figure 5.13: Scaling power spectrum from ensemble model

basis of SOC behaviour, and the necessary ingredients.

In the VEM there are no correlations and all vertices are independent, so the answer must lie in the form of the individual vertex orbits. We know from the studies of Kraynik et al. that only a very small set of orbits are periodic, a set as sparse as the rationals amongst the real numbers. In fact Kraynik and Hansen proved that these orbits are indexed by solutions to a Diophantine equation, and that all other orbits are completely aperiodic. This term is used in the sense that they never again visit their starting configuration. However, the question of what the orbits do look like was left open. A representative stress orbit is shown in Figs. 5.14 & 5.15, and the total energy orbit is shown in Fig. 5.16.

Examining the orbits we see that the origins of the scale invariant spectra are clear, the non-periodic orbits are in some sense self-affine. Evidently they are not perfectly self-affine in that they have a cut-off at the shear-scale $0 < \gamma < 10$, but looking at the same orbits at larger and larger shear-scales we see the same form, with different scaling parameters in the two different dimensions. A rough argument connecting the self-affinity and the power law spectra can be constructed as follows.

The definition of self-similarity for the orbit means that

$$f(A_h^n x) = A_v^n f(x) \tag{5.7}$$

where A_h, A_v are the horizontal and vertical scaling factors, which define the scaling exponent α through

$$\alpha = \frac{\log A_v}{\log A_h} \tag{5.8}$$

Now denoting the Fourier transform of $f(x)$ by $\tilde{f}(\omega)$ we have

$$A_h^{-n} \tilde{f}\left(\frac{\omega}{A_h^n}\right) = A_v^n \tilde{f}(\omega) \tag{5.9}$$

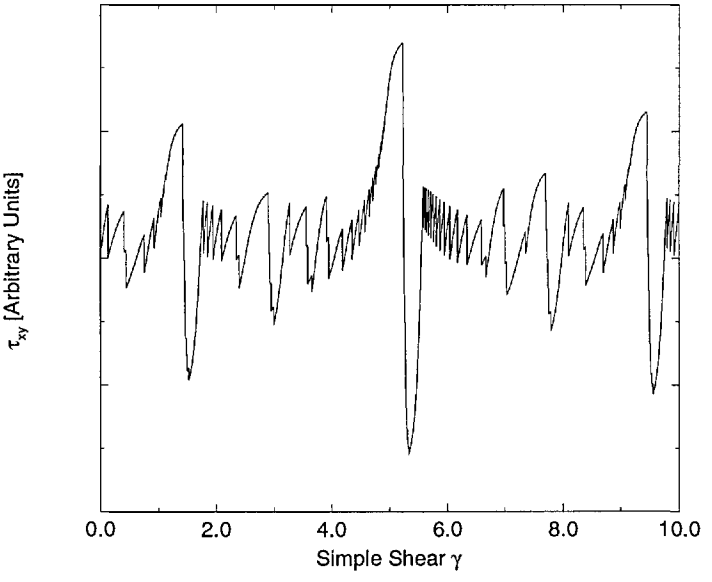

Figure 5.14: Stress orbit for $\theta = 0.9817$ $0 < \gamma < 10$

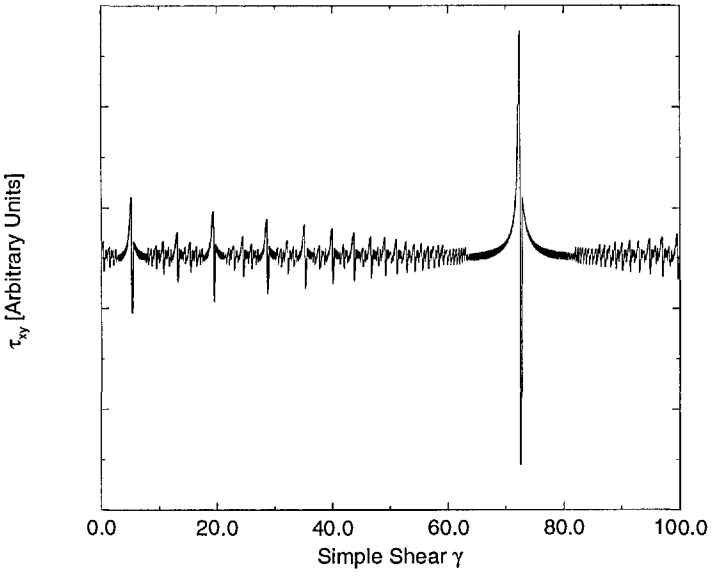

Figure 5.15: Stress orbit for $\theta = 0.9817$ $0 < \gamma < 100$

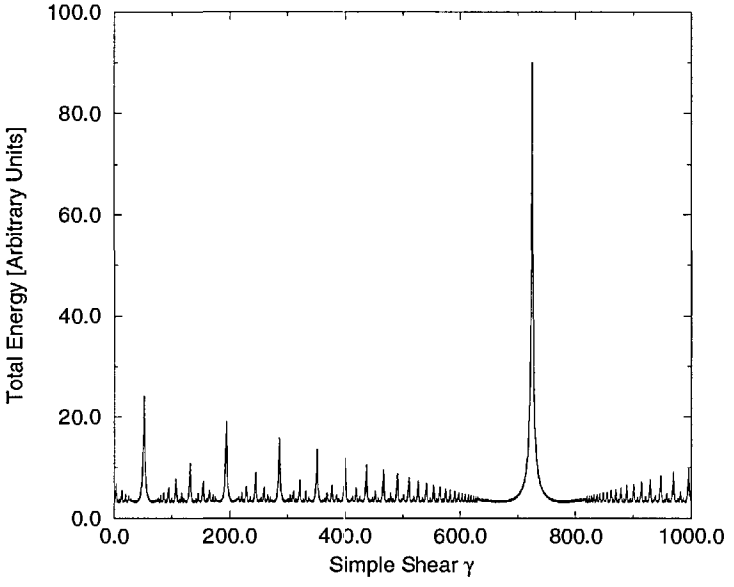

Figure 5.16: Length orbit for $\theta = 0.9817$

so that

$$\tilde{f}(\omega) = (A_h A_v)^n \tilde{f}(A_h^n \omega) \tag{5.10}$$

Now if we define $\Omega = A_h^n$, fixing ω at $\omega = \omega_0$ we have

$$\tilde{f}(\Omega\omega_0) = \Omega^{-(1+\alpha)} \tilde{f}(\omega_0) \tag{5.11}$$

as $A_v^n = A_h^{n\alpha} = \Omega^\alpha$, by Eq. 5.8. This implies that

$$\tilde{f}(\Omega) \simeq \Omega^{-(1+\alpha)} \tag{5.12}$$

and that the power spectrum $S(\omega)$, which is $\sim \tilde{f}^2$ is

$$S(\Omega) \simeq \Omega^{-2(1+\alpha)} \tag{5.13}$$

Clearly if these orbits are self-similar, as time (or strain) goes by the magnitude of the peaks in energy or shear stress must increase, which is indeed seen in Fig. 5.16. This may seem unphysical at first but is in fact caused by the same mechanism which gives rise to the exponentially diverging length in the example given by Kraynik. Because we are considering the system under an area conserving map all cells have constant area. As they become elongated they squeeze in together, and in order to cover the initial sample area they pull in cells from far away, while pushing out cells from the initial sample area at the sides of the sample. This leads to a high density of cells with a high contribution to the stress tensor component along the strain axis, and thus a high peak. This is an artefact of the hexagonal foam model, but

one which is consistent within the model. The sharpness of the peak is an illusion caused by the fact that we are looking at graphs covering a very large range of strains, in fact the 'sides' of the peak are very much like the sides of peaks in the earlier graphs of lower strain systems; they are formed of a smooth curve on the leading side and a cascade of T1 events on the falling side. These arise in the manner shown in Fig. 5.4.

Thus, we see that self-affine orbits imply a power law spectrum for the net stress orbit, if, as we observe, the individual orbits share similar values of α. As noted above the value of α found in these deterministic orbits ranges around 1.5, while the exponents found in our stress and energy power spectra are around -4.2. Thus, we see that the connection is confirmed, although a closer match would be desirable. The deviation is probably due to the additional presence of periodic orbits.

Two interesting questions still remain with respect to these orbits, which unfortunately we have not been able to resolve. Firstly what are the key features of the dynamic map $\mathcal{F}_\mathcal{V}$ which produce this behaviour, and secondly how do they sum together to give such a smooth bulk stress orbit.

The first question is especially interesting as we have searched a large amount of the fractal and dynamic systems literature and have not found another system which exhibits this type of orbit. However, the literature is vast and this does not necessarily mean that no such work has been done. Nevertheless this behaviour seems original. Deterministic fractals, and self-affine curves, typically arise from recursive rules which operate on the whole curve, of the kind which produce the Koch curve etc. Fractals which are associated with dynamic systems are generally either limiting sets or attractors which are not traced by the evolving phase points but only defined by them, or are Poincaré sections. In this system the self-affine curve is the orbit of the evolving vertex itself. The manner of construction is clearly different, Poincaré sections grow by periodically sampling the system, strange attractors are limit sets and the Koch curve is defined recursively, these orbits are growing self-affine curves. We have not been able to find evidence of this kind of 'growing' fractal elsewhere.

The map has a feature which may be of relevance. Firstly the map moves vertices towards fixed boundaries at which they undergo some discontinuous motion. In the dry foam mapping the vertices jump in orientation and also in film length configuration, which implies a jump along the boundary and a jump into the bulk of the configuration space. However, as we see below the basic features of the orbits are retained under the viscous map, which has only the jumps along the boundaries. Presumably the presence of these discontinuities in the orbits has some relation to the fractal orbit structure.

It is also interesting to ponder the way in which the vertex model mimics the 'true' SOC system. It is evident that at least some kinds of quasi-SOC behaviour can arise, not from the commonly found local correlations, but from large systems of elements with independent stick-

slip dynamics. Yet it is not immediately apparent if this explanation can have any relevance to systems such as the sand pile, where no such independent subsystem is obvious. Certainly the sand grain and the foam vertex have little in common beyond the external forces bearing on them. Perhaps by considering a more abstract subsytem a formulation of the sand-pile in terms of a VEM-like model is possible, or perhaps foam dynamics belongs to a class of quasi-SOC systems, which possess some of the properties of SOC systems but are not truly linked to them.

We should note that the above discussion of how well the model fits the simulation data, even having power law fluctuations, does cast a small amount of doubt on the means of dealing with the errors in the calculations. By repeating the calculations with different ensembles we find that the errors are small relative to the signal we are interested in, of order 1%. However, we know that the errors, which are essentially the fluctuations, are not distributed normally but in a power law distribution. Furthermore we have seen by looking at the orbits that the net behaviour arises from the summation of many thin spikes, where the spikes grow in height as the γ gets larger. Thus, we may expect large fluctuations in the large shear limit, and would need to be careful in using data collected from such large shear values, but these values are of no physical interest and have not been studied in our work.

5.6 VEM with Viscous Forces

The approach we will use is very simplistic, but nevertheless effective to some degree. It was first proposed by Khan and Armstrong, and subsequently used by Kraynik and Hansen in their early work. The assumption is that the viscous forces have little effect on the dynamics of the foam when the deformation rate is small, and that the major effect is in the adjusted expression for the stress tensor. The idea is to ignore the effects on the vertex map, using the same one as above, and to include extra terms in the stress tensor expressions which include the film viscosity, these terms are derived in Appendix B. By using this method we obtain a viscous contribution to the stress tensor which is added to the surface tension contribution. This term is only dependent on the strain rate through a simple factor. This method has never been carried out with the full expression for the viscous forces acting in the foam, but only with simpler approximations.

By using the full expression for the viscous forces we obtain a contribution which is proportional to $\dot{\gamma}^{2/3}$ which is in agreement with a more complete treatment by Kraynik and Reinelt, although it disagrees with early experimental results of Princen and Kiss which suggest a contribution like $\dot{\gamma}^{1/2}$, although for wetter foams. The calculation is also at variance with the results of Kawasaki et al., who found classical Bingham fluid like behaviour with $\dot{\gamma}$, although they stated that [93] their data were not accurate enough to determine the exponent properly.

The form of the viscous term with respect to the shear is shown compared to the surface

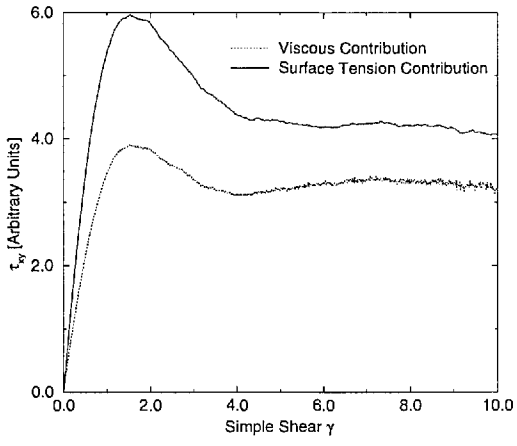

Figure 5.17: Naive viscous contribution in simple shear

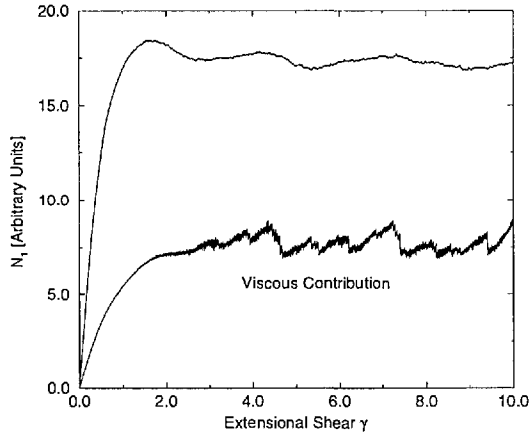

Figure 5.18: Naive viscous contribution in extensional shear

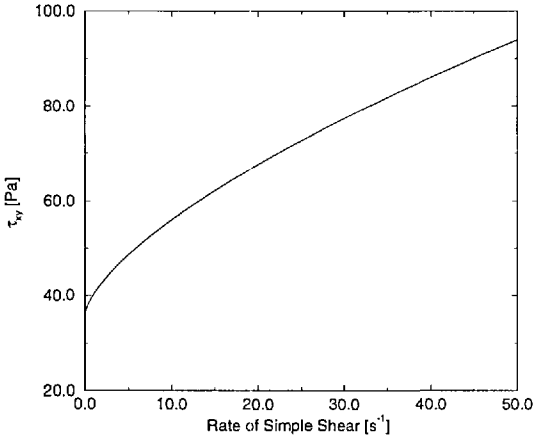

Figure 5.19: Total stress against strain rate in simple shear

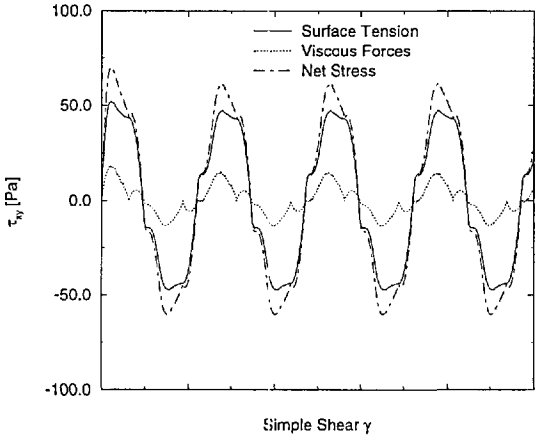

Figure 5.20: Viscous term for oscillating simple shear

tension term in Figs. 5.17 and 5.18. Evidently the viscous term has a similar strain dependence to the surface tension term, which means that the net stress is also similar. Thus, the net stress also shows an elastic regime, a yield stress, and a plastic flow regime. The total stress in the plastic regime is plotted against the strain rate for simple shear in Fig. 5.19. The plot for extensional shear is identical in form. It is clear that the behaviour may be hard to distinguish from Bingham fluid behaviour in experiments.

In Fig. 5.21 we plot the predictions of this simple approach to viscous forces for the situation of oscillating simple shear, as measured by Prud'homme and Yoshimura [66]. We note the peculiar shape of our viscous term in Fig. 5.20, with two peaks in each strain half-period. This would appear to be related to the similar structure of the surface tension component. Once again it is caused by the level of structure (history) which the foam maintains, so that it is not

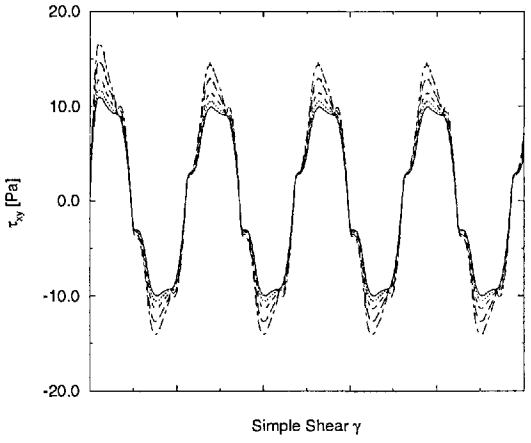

Figure 5.21: Different rates of oscillation

fully relaxed at the point where strain is zero, and exhibits two distinct phases as the strain grows in the opposing direction.

This simple model gives us a not unreasonable estimate of the foam's true behaviour. We, like Prud'homme and Yoshimura, observe an increasing structure to the response as the strain rate increases, with the stress being much greater in the first portion of the strain half-period, see Fig. 2.22.

Chapter 6

Osmotic Pressure of 2D Foam

6.1 Osmotic Pressure of Ordered Foam

As usual our starting place in dealing with the study of the osmotic pressure of foam is with the osmotic pressure of a 2D ordered hexagonal foam. Princen solved this problem in Ref. [2] and found that

$$\Pi = \frac{\sigma}{R}\left(\frac{\Phi}{\Phi_c^h}\right)^{1/2}\left[\left(\frac{1-\Phi_c^h}{1-\Phi}\right)^{1/2} - 1\right] \tag{6.1}$$

where Φ denotes the gas volume fraction (from now on we shall use Φ interchangeably with Φ_g unless otherwise stated, and Φ_l for the liquid volume fraction, ie $\Phi_l = 1 - \Phi_g$), and Φ_c^h denotes the 'critical packing fraction' where the foam begins to disintegrate into isolated bubbles. This fraction is given by

$$\Phi_c^h = \frac{\pi}{2\sqrt{3}} \simeq 0.907 \tag{6.2}$$

Princen used the symmetry of the hexagonal structure to determine the arrangement of fluid inside the foam, and the corresponding changes in the surface length. He imagined that one starts with a hexagonal close-packed array of round bubbles and then applies pressure Π which compresses the foam forcing the bubbles to develop flat contact regions — films. This involves the expulsion of fluid and determines the relationship between volume fraction and pressure.

In Appendix C we reproduce a similar argument with which to derive the same result but this time starting with a perfectly dry hexagonal foam and allowing the foam to expand and suck up fluid. We now extend this new argument in order to deal with hexagonal foams constructed from films with differing lengths, first by considering foams with two distinct film lengths and then those with three film lengths, note that these foams still have an ordered structure. Finally by considering the probability distribution of film lengths, which we have in analytical form, we use the VEM approach to predict the osmotic pressure of disordered foams.

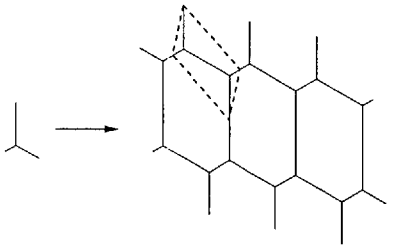

Figure 6.1: Constructing an ordered foam with unit cell

6.2 Extended Ordered Foam

We know that the reason for the difference in behaviour between the hexagonal ordered foam and the disordered foam lies basically in the way in which the thin films disappear. One sign is in the behaviour at the rigidity loss transition, where due to the lesser 'stiffness' of the thick films increased fluid fraction leads to disintegration. In the ordered foam this disintegration is instantaneous, whilst in the disordered foam it is gradual, leading to the percolation effect, as some films disappear before others. At first the fluid collects at the vertices, but at some stage the vertices at opposing ends of a film will touch, and then it becomes a thick film. Evidently short films will disappear first, so that the percolation behaviour is intimately connected to the distribution of film lengths. A similar effect can be seen to operate on the osmotic pressure (they are related as mentioned above). The configuration of a thick film is quite different to that of a pair of wet vertices, and leads to a change in the osmotic pressure behaviour for the thick films. So again, we expect the tail of the osmotic pressure curve to be determined by the way in which the film length distribution mixes different basic behaviours.

We therefore wish to study foams with unequal film lengths. We start by considering an extension of Princen's model by looking at foams formed from a repeated hexagonal cell, but with unequal side lengths. We can then extend the model to approximate to a disordered foam by using the VEM approach, with a distribution of vertices behaving as if they were embedded in an ordered foam.

By selecting three half-films with arbitrary lengths we can construct an ordered hexagonal foam, as shown in Fig. 6.1. We can imagine a foam like this with no boundaries, we choose to imagine a foam on a two-dimensional torus (periodic boundary conditions) rather than an infinite sample. We note two things here about the model :

- We are interested in the quasistatic behaviour of the foam, and wish to construct a simple model containing the important features. Therefore, we do not wish to describe the detailed processes by which the fluid makes its way to the Plateau borders. This leads us to study the way in which the Plateau borders change for a system with a fixed geometry, by which we mean that the shape of the unit cell, as shown dashed in Fig. 6.1,

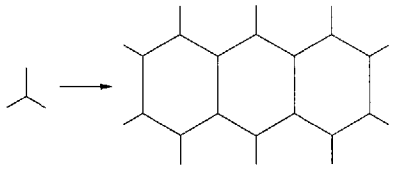

Figure 6.2: Constructing a symmetric ordered foam

is constant even though its size is changing. It is conceivable, though unlikely, that under some circumstances the foam in Fig. 6.1 would alter its film lengths in order to move towards the ordered foam as we added fluid. We do not expect this to be relevant anyway because a truly disordered foam could not order itself thus.

- Leading on from this point we can see that a local unit cell in a disordered foam has a constrained geometry because of the presence of its neighbours — its motions are highly restricted. Thus in order to model disordered foams we wish to consider the case where the unit cell has a constant shape (is similar to itself at different scales).

So in this model we imagine a torus whose shape is such that when covered with a hexagonal ordered foam some films are longer than others. To keep the unit cell shape constant means to keep the torus shape constant, whilst applying a uniform dilation (blowing it up like a balloon).

6.2.1 Two distinct film lengths

We start by considering a case in which we have two films of equal length, and the third different. This is a more symmetrical case which is easier to study. The foam is shown in Fig. 6.2.

We will obtain the length l and liquid volume u_l of a vertex, with three half-films, initially one of length a_0 and two of length b_0, as functions of Φ. As before we model the vertex as embedded in a periodic hexagonal foam, constructed of copies of itself. We will define $b_0 = \alpha a_0$, so that $\alpha = 1$ corresponds to the case studied by Princen. We can split the behaviour down into several parts

- Three thin films and a wet vertex
- One thick film, and two thin films. This happens if $a_0 < b_0$ ($\alpha > 1$)and occurs when the vertices at opposing ends of film a coalesce.
- Two thick films, and one thin film. This happens if $b_0 < a_0$ ($\alpha < 1$)and occurs when the vertices at opposing ends of the films b coalesce.
- Three thick films. This case presents no difficulties, it corresponds to the disintegration of the foam and thus the osmotic pressure $\Pi = 0$.

Three thin films

First we consider the case where the vertex is wet, and the three films are thin, as shown in the central part of Fig. 6.3, the larger circle shows the point at which we leave this mode and move to the mode with one thick film.

First of all we have from our previous model that

$$u_l = 2r^2\left(\sqrt{3} - \frac{\pi}{2}\right) \tag{6.3}$$

and we define

$$Q = \left(\sqrt{3} - \frac{\pi}{2}\right) \tag{6.4}$$

so that

$$u_l = 2Qr^2 \tag{6.5}$$

$$du = 4rQ\,dr \tag{6.6}$$

Φ is defined so that

$$\Phi = \frac{u_g}{u} \rightarrow d\Phi = -\frac{u_g}{u^2}du = -\frac{\Phi^2}{u_g}du \tag{6.7}$$

We also know that the geometry of the Plateau border is constant up until the point at which one film thickens — we have three films, a border formed of three circular arcs, and the angles are fixed at 120°. This implies that $b = \alpha a$, so that

$$l = 2(4b + 2a) - 4rQ = 4(2\alpha + 1)a - 4rQ \tag{6.8}$$

$$dl = 4(2\alpha + 1)\,da - 4Q\,dr \tag{6.9}$$

Also we have

$$a = \frac{a_0}{\Phi^{1/2}} \tag{6.10}$$

so that

$$da = -\frac{a_0}{2}\Phi^{-3/2}\,d\Phi = \frac{a_0}{2}\frac{\Phi^{1/2}}{u_g}\,du \tag{6.11}$$

and likewise for b. This implies that all together

$$dl = 2(2\alpha + 1)a_0\frac{\Phi^{1/2}}{u_g}\,du - \frac{du}{r} \tag{6.12}$$

The constant geometry also allows us to define another function $H(a)$ giving the volume of the hexagon unit cell

$$H(a, b) = b\sqrt{3}(a + b/2) \tag{6.13}$$

$$H(a) = \alpha\frac{\sqrt{3}}{2}(2 + \alpha)a^2 \tag{6.14}$$

so that

$$\dot{\Phi} = 1 - \frac{u_l}{u} = 1 - \frac{2Qr^2}{H(a)} = 1 - \frac{2Qr^2\Phi}{u_g} \tag{6.15}$$

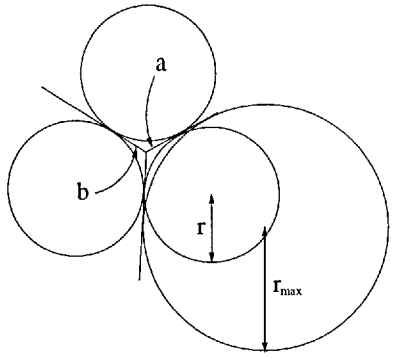

Figure 6.3: Vertex with fluid

so that now we can obtain

$$\Pi = -\sigma \frac{dl}{du} = -\sigma \left(2(2\alpha+1)a_0 \frac{\Phi^{1/2}}{u_g} - \left(\frac{2Q\Phi}{u_g(1-\Phi)} \right)^{1/2} \right) \tag{6.16}$$

We would like to rewrite this result in a more meaningful form. We can do this by introducing the value Φ_c at which the first Plateau borders coalesce. There are two separate expressions for this value, depending on whether $\alpha > 1$ or $\alpha < 1$.

If $\alpha > 1$ then we have border coalescence when

$$r = a\sqrt{3} = \frac{a_0\sqrt{3}}{\Phi^{1/2}} \tag{6.17}$$

which means that

$$\frac{a_0\sqrt{3}}{\Phi_c^{1/2}} = \left(\frac{H_0(1-\Phi_c)}{2Q\Phi_c} \right)^{1/2} = \left(\left(2\sqrt{3}\alpha(2+\alpha)a_0^2 \right) \frac{(1-\Phi_c)}{2Q\Phi_c} \right)^{1/2} \tag{6.18}$$

so that

$$\Phi_c = 1 - \frac{\sqrt{3}Q}{\alpha(2+\alpha)} \tag{6.19}$$

We can immediately check this expression by setting $\alpha = 1$, with which we obtain

$$\Phi_c(\alpha = 1) = 1 - \frac{\sqrt{3}Q}{3} = 1 - \frac{(\sqrt{3} - \pi/2)}{\sqrt{3}} \tag{6.20}$$

which gives us $\Phi_c = \pi/2\sqrt{3}$, identical with Princen's result.

Considering the second case we have $\alpha < 1$, and coalescence when

$$r = b\sqrt{3} = \frac{\alpha a_0\sqrt{3}}{\Phi^{1/2}} \tag{6.21}$$

so that

$$\frac{\alpha a_0\sqrt{3}}{\Phi_c^{1/2}} = \left(\frac{H_0(1-\Phi_c)}{2Q\Phi_c} \right)^{1/2} = \left(\left(2\sqrt{3}\alpha(2+\alpha)a_0^2 \right) \frac{(1-\Phi_c)}{2Q\Phi_c} \right)^{1/2} \tag{6.22}$$

so finally

$$\Phi_c = 1 - \frac{\alpha\sqrt{3}Q}{2+\alpha} \tag{6.23}$$

Again we can check this and we find that for $\alpha = 1$ this expression gives $\Phi_c = \pi/2\sqrt{3}$. We plot the value of Φ_c against α in Fig. 6.4, the cusp is at the point where $\alpha = 1$, and $\Phi_c = 0.9069$.

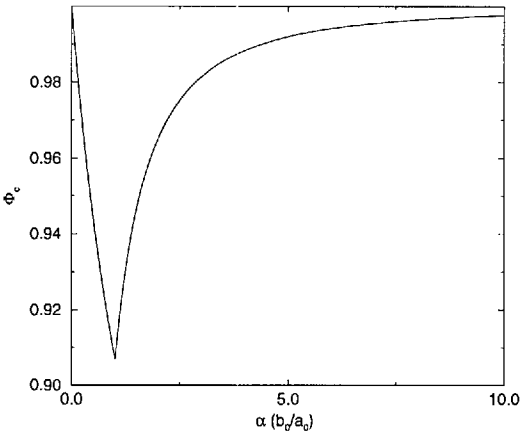

Figure 6.4: Φ_c against α

Now returning to our calculation of Π, we have for the case where $\alpha > 1$ that

$$Q = \frac{(1 - \Phi_c)\alpha(2+\alpha)}{\sqrt{3}} \tag{6.24}$$

so that we can rewrite Eq. 6.16

$$\Pi = -\frac{\sigma\Phi^{1/2}}{u_g}\left(2(2\alpha+1)a_0 - \left(\frac{2(1-\Phi_c)\alpha(2+\alpha)u_g}{\sqrt{3}\,(1-\Phi)}\right)^{1/2}\right) \tag{6.25}$$

and by using Eq. 6.14 and $u_g = \pi R^2$, R being the radius of the free bubbles, we get

$$\Pi = -\frac{2\sigma\Phi^{1/2}a_0}{\pi R^2}\left((2\alpha+1) - \alpha(2+\alpha)\left(\frac{1-\Phi_c}{1-\Phi}\right)^{1/2}\right) \tag{6.26}$$

Now we use Eq. 6.20 to obtain

$$\Pi = -\frac{2\sigma}{\pi R^2}\left(1 - \frac{\sqrt{3}Q}{\alpha(2+\alpha)}\right)^{\frac{1}{2}}\left(\frac{\pi R^2}{2\sqrt{3}\alpha(2+\alpha)}\right)^{\frac{1}{2}}\left(\frac{\Phi}{\Phi_c}\right)^{\frac{1}{2}}\left(2\alpha+1-\alpha(2+\alpha)\left(\frac{1-\Phi_c}{1-\Phi}\right)^{\frac{1}{2}}\right) \tag{6.27}$$

Now we can tidy up the prefactor to get

$$\Pi = -\frac{\sigma}{R}\frac{2}{\alpha(2+\alpha)}\left(\frac{\alpha(2+\alpha)-\sqrt{3}Q}{2\sqrt{3}\pi}\right)^{\frac{1}{2}}\left(\frac{\Phi}{\Phi_c}\right)^{\frac{1}{2}}\left(2\alpha+1-\alpha(2+\alpha)\left(\frac{1-\Phi_c}{1-\Phi}\right)^{\frac{1}{2}}\right) \tag{6.28}$$

Again we can check our result against Princen's, Eq. C.21, for $\alpha = 1$. The prefactor evaluates to $1/3$, whilst the α terms in the brackets equal 3, so that the result indeed checks.

For the case where $\alpha < 1$ the working is similar, so that

$$Q = \frac{(1 - \Phi_c)(2+\alpha)}{\alpha\sqrt{3}} \tag{6.29}$$

so that we can rewrite Eq. 6.16

$$\Pi = -\frac{\sigma\Phi^{1/2}}{u_g}\left(2(2\alpha+1)a_0 - \left(\frac{2(1-\Phi_c)(2+\alpha)u_g}{\alpha\sqrt{3}\,(1-\Phi)}\right)^{1/2}\right) \tag{6.30}$$

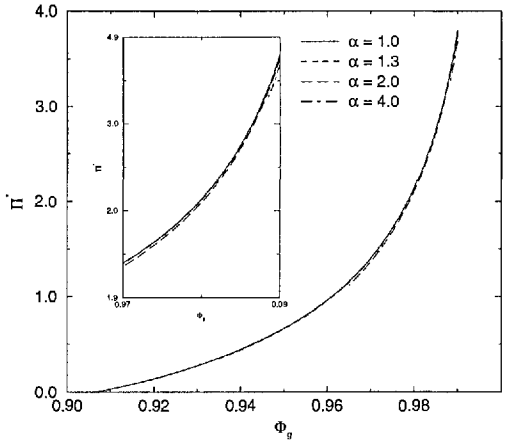

Figure 6.5: Π^* against Φ for $\alpha > 1$

and by using Eq. 6.14 and $u_g = \pi R^2$, R being the radius of the free bubbles, we get

$$\Pi = -\frac{2\sigma\Phi^{1/2}a_0}{\pi R^2}\left(2\alpha + 1 - (2+\alpha)\left(\frac{1-\Phi_c}{1-\Phi}\right)^{1/2}\right) \tag{6.31}$$

Now we use Eq. 6.23 to obtain

$$\Pi = -\frac{2\sigma}{\pi R^2}\left(1 - \frac{\sqrt{3}\alpha Q}{2+\alpha}\right)^{\frac{1}{2}}\left(\frac{\pi R^2}{2\sqrt{3}\alpha(2+\alpha)}\right)^{\frac{1}{2}}\left(\frac{\Phi}{\Phi_c}\right)^{\frac{1}{2}}\left(2\alpha + 1 - (2+\alpha)\left(\frac{1-\Phi_c}{1-\Phi}\right)^{\frac{1}{2}}\right) \tag{6.32}$$

Now we can tidy up the prefactor to get

$$\Pi = -\frac{\sigma}{R}\frac{2}{2+\alpha}\left(\frac{2+\alpha-\sqrt{3}Q\alpha}{2\sqrt{3}\alpha\pi}\right)^{\frac{1}{2}}\left(\frac{\Phi}{\Phi_c}\right)^{\frac{1}{2}}\left(2\alpha + 1 - (2+\alpha)\left(\frac{1-\Phi_c}{1-\Phi}\right)^{\frac{1}{2}}\right) \tag{6.33}$$

Once again we can check our result against Princen's, Eq. C.21, for $\alpha = 1$. Again the prefactor evaluates to $1/3$, whilst the α terms in the brackets equal 3, so that the result indeed checks.

These formulae can now be used to plot the first part of the osmotic pressure curves of these foams. In Figs. 6.6 & 6.5 we plot several of these curves, for $0.25 \leq \alpha \leq 4$, with the curve for $\alpha = 1$ for comparison. The curves in Figs. 6.6 & 6.5 are very close to the curve for $\alpha = 1$, but with the cutoffs apparent. We should briefly discuss the curves; it might seem at first that the curves should all lie on top of each other, with only the cut-offs differing. This seems reasonable because after all we are adding fluid to a dry foam, and it is merely decorating the vertices, up until the first coalescence. Thus each vertex is exactly the same as in Princen's case, and the relationship between the amount of fluid at the vertex and the small change in length should be the same for all values of α. However this first impression is wrong because it assumes that we are holding $u = u_l + u_g$ constant during the operation; one can see that if this were the case it would be correct. However the definition of the osmotic pressure requires us to vary u_l

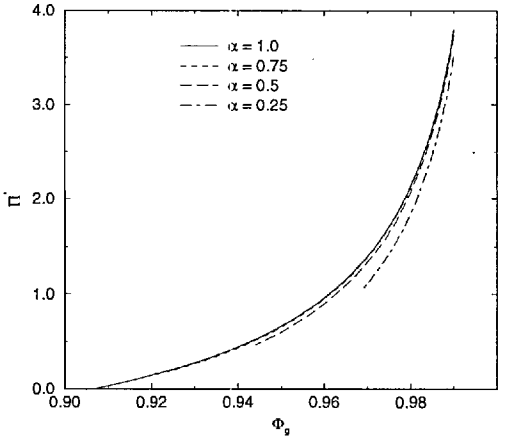

Figure 6.6: Π^* against Φ for $\alpha < 1$

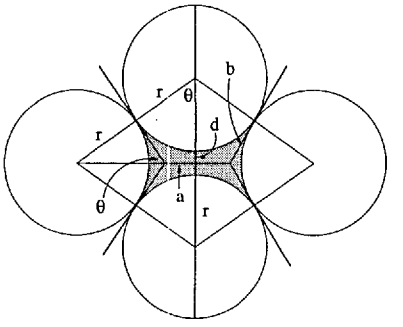

Figure 6.7: Vertex with one thick film

while holding u_g constant. The constancy of u_g implies that we must increase u by increasing slightly the size of the unit cell containing the bubble. This area increase implies an increase of the dry film length corresponding to the edges of the unit cell, and naturally the ratio of the two changes is a function of the geometry of the unit cell, and thus of α. This then accounts for the very small variations in Π as a function of Φ as α moves away from $\alpha = 1$.

Once the foam has reached the first border coalescence at $\Phi = \Phi_c$ it moves into one of two modes. If $\alpha < 1$ the foam subsequently has two thick films, alternatively if $\alpha > 1$ it has two thin films. These two cases behave quite distinctly up until the point at which the foam disintegrates into separate bubbles.

One thick, two thin films — $\alpha > 1$

We first consider the case with $\alpha > 1$. The foam continues to absorb fluid into its new geometry, as shown in Fig. 6.7, until it reaches the point of disintegration shown in Fig. 6.8. We will first discuss the general behaviour of the foam, then we shall derive equations to describe it.

The geometry of the foam is shown in Figs. 6.7 & 6.8. The foam is now formed of bubbles

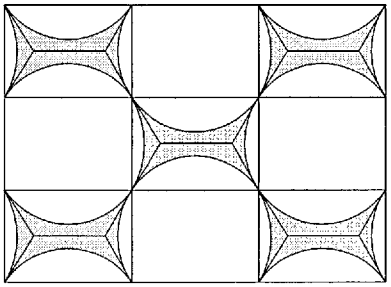

Figure 6.8: Definition of the box-cell

separated by thin films and by thick Plateau borders, as each bubble could previously be associated with two vertices, we now associate one Plateau border with each bubble. The Plateau border is formed by four circular arc films, as shown in Fig. 6.7. We now define new cell which is more useful than the hexagonal cell containing the bubble. This new cell is the box-cell, shown in Fig. 6.8. Its corners are at the middle of the b films, lying on the centres of the edges of the rhombus in Fig. 6.7. Because of the assumed constant geometry of the foam, as we increase the fluid fraction the shape of this box-cell will remain constant, with side length ratio β. The foam can be built from these cells, alternately full of gas, or containing a Plateau border. At the final border coalescence, or disintegration, the bubbles are the circumcircles of the empty box-cells.

It is also useful to show the shape of the vertex in another way, as depicted in Fig. 6.9, and extended from Weaire et al. [103]. (x, y) is the corner of the box-cell, of which a quarter is shown. We can see that all arcs are of radius r as follows. The arcs lining the gray area are of radius r, being the curved film surfaces. The quarter-circle passing through the end of the thin film and the extremity of the wet area has radius r by the cosine rule. The line passing through the intersection, perpendicular to the thin film, forms a right-angled triangle with hypotenuse $2r$ with the axes; this can be seen also in Fig. 6.7. Now the length $\vec{OA} = 2r\cos\theta$, so that $\vec{OX} = r^2 + 4r^2\cos^2\theta - 2 \times r \times 2r\cos\theta \times \cos\theta = r^2$.

The smaller dashed box we will term the inner-box. The inner-box has its corner where the thin film ends, so that this box contains the wet part of the box-cell. The shape of this cell varies as the liquid fraction changes, and it coincides with the box-cell at disintegration. The relation between angles ψ and θ is

$$\psi = \frac{\pi}{2} - \theta \tag{6.34}$$

Now we can see that for r, x, y set to particular values we can vary θ over a range of structures, the problem we need to solve is to find the correct one. Once we know the dependence of the structure of the Plateau border on the liquid fraction we can proceed as before to determine the free energy, and thus the osmotic pressure. The structure of the border is harder to determine than before, because θ & r can be varied independently and the only constraints are the

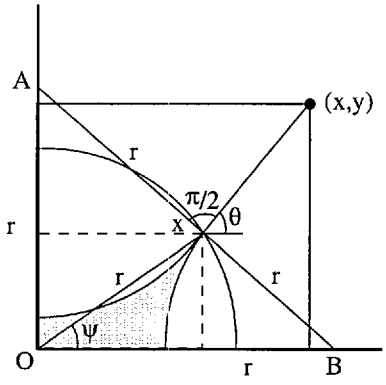

Figure 6.9: Border diagram

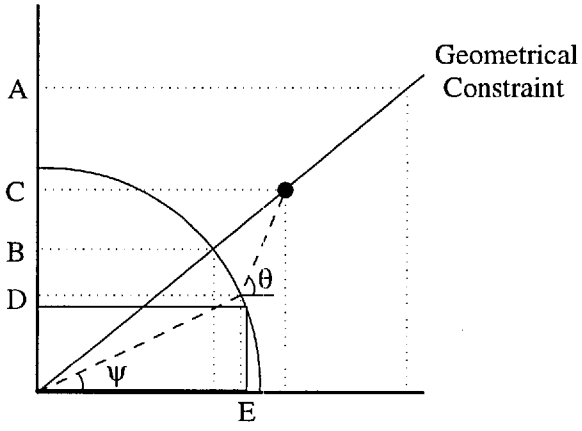

Figure 6.10: Border diagram for foam with small α

volume fraction Φ, and the equilibrium requirement, which cannot be readily solved. However we can simplify the problem by looking at Fig. 6.10, which shows us the border diagram of a small α (but $\alpha \geq 1$) foam, however note that all border diagrams are schematic. In this form of border diagram we keep the size of r fixed, scaling everything else to fit. A is the box-cell for the initial state, at Φ_c, whilst B is the inner-box for the final state, at Φ_d. C & D are the box-cell and inner-box respectively for a Φ somewhere inbetween. The corners of all the box-cells must lie on the line marked 'Geometrical Constraint', and they move along it as Φ varies. The corners of the inner-boxes move along the arc, and the two coincide at disintegration. The inner-box starts off at the first border coalescence as E, and moves to B, with θ varying corresponding to the variation in ψ, so that evidently as a result θ must cover the entire interval between $\pi/3$ and θ_d (excluding T1s, see below). Using this fact we can obtain Φ and Π as functions of θ. The dashed line passing through the corner of inner-box D is the vector to the end of the thin film. When Φ reaches Φ_d this must lie along the 'Geometrical Constraint' line. The further section of dashed line shows the film vector, and must pass through the corner of the box-cell. It is apparent that this is possible for all values of θ in the range $\pi/3$ to θ_d.

In Figs. 6.11, 6.12 & 6.13 are shown the paths described by some example borders. Fig. 6.11 shows a foam with $\alpha \simeq 2$, which means that $b_0 \simeq 2a_0$. It is evident that the value of Φ_d is much lower than for Princen's regular foam. The border moves smoothly between coalescences. In Fig. 6.12 is a foam with square symmetry, we will see this is a dividing case. The final figure, Fig. 6.13, shows the path of a foam with α just over 3.0. Figs. 6.12 & 6.13 have in common that they show foams which can be thought of as stressed, they can be made from regular hexagonal foam by stretching along one axis. The foam in Fig. 6.12 is strained along the direction of the middle film, and so it is in the lowest possible energy configuration, thus it behaves smoothly. However the foam in 6.13 is strained perpendicular to the middle film, and it is initially sitting in a local but not global minimum configuration. This is the same situation which has become familiar in foam rheology, where a vertex pair is trapped in a local minimum and can only be free to move the global minimum at some critical strain, at which it undergoes the well-known T1 process. Here we have the same T1 process occurring in the wetting of the foam — the vertex pairs cannot access the lower energy state until some critical Φ, which we will call Φ_t. This effect has previously been noted in Weaire et al.'s simulation results, [103], and the effects can be clearly seen in Fig. 4 of Ref. [104], in which the liquid fraction of a simulated disordered foam is cycled, where the osmotic pressure response on the first wetting cycle differs from that on subsequent cycles.

A firmer demonstration of the nature of the T1 and local minimum can be given with the help of the border diagram, shown in Fig. 6.14. The parallel to the strain T1 is exact, the vertex pair, or border, is sitting in a local minimum and can only move to the global minimum at a critical Φ_t. The reason this Φ_t is critical is that the border can not change any further in that configuration, in the present case it can absorb no more fluid in the rheological case it can absorb no more strain. The way this works is shown in the border diagram, where again 'Geometrical Constraint' marks the line of box-cell corners, A marks the initial box-cell, C the initial inner-box, B the final inner-box, and D an critical inner-box. The diagonal line shows the 'Geometrical Constraint' line for foams with square symmetry, any foam strained beyond this line must undergo a T1 during wetting. The dashed line passing through the corner of inner-box C has the same significance as before, and shows that this configuration is possible. However when we look at inner-box D we can see that it is not possible to maintain this configuration, because the film vector line is parallel to the 'Geometrical Constraint' line and cannot intersect it, remember the two angles ψ and θ are linked. This inner-box is the critical point, the border now passes through non-equilibrium configurations, which are examined in more detail in Ref. [104], in order to reach a new equilibrium position. The new equilibrium configuration is on the other side of the diagonal line, and is identical to that for a foam which has been strained in a similar way along the centre film, because β' must equal β^{-1}.

This can all be explained further using the concepts of the equilibrium surface and catas-

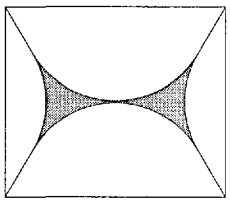

$\Phi = 0.962$

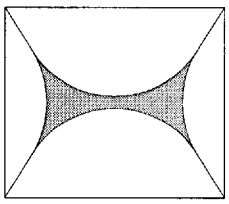

$\Phi = 0.947$

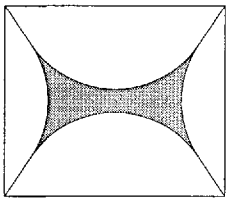

$\Phi = 0.932$

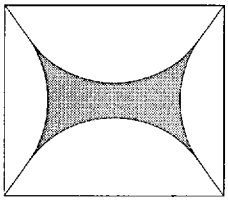

$\Phi = 0.915$

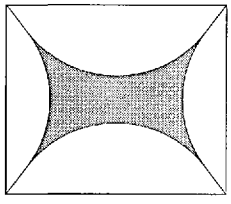

$\Phi = 0.893$

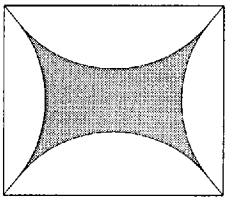

$\Phi = 0.861$

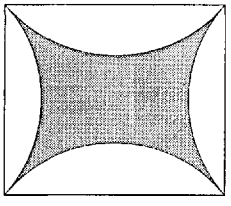

$\Phi = 0.802$

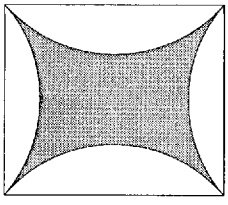

$\Phi = 0.793$

Figure 6.11: Behaviour of foam with $\beta = 1.732$

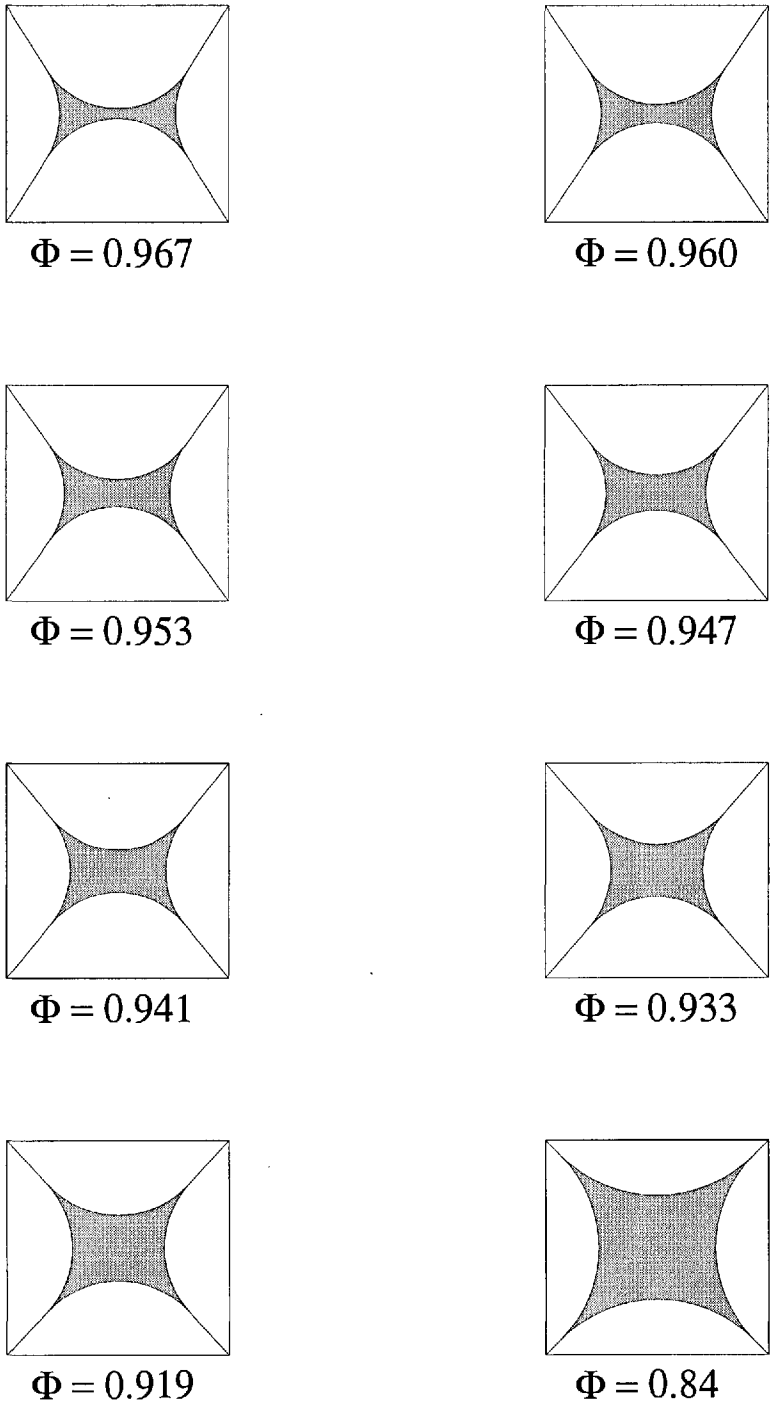

Figure 6.12: Behaviour of foam with $\beta = 1$

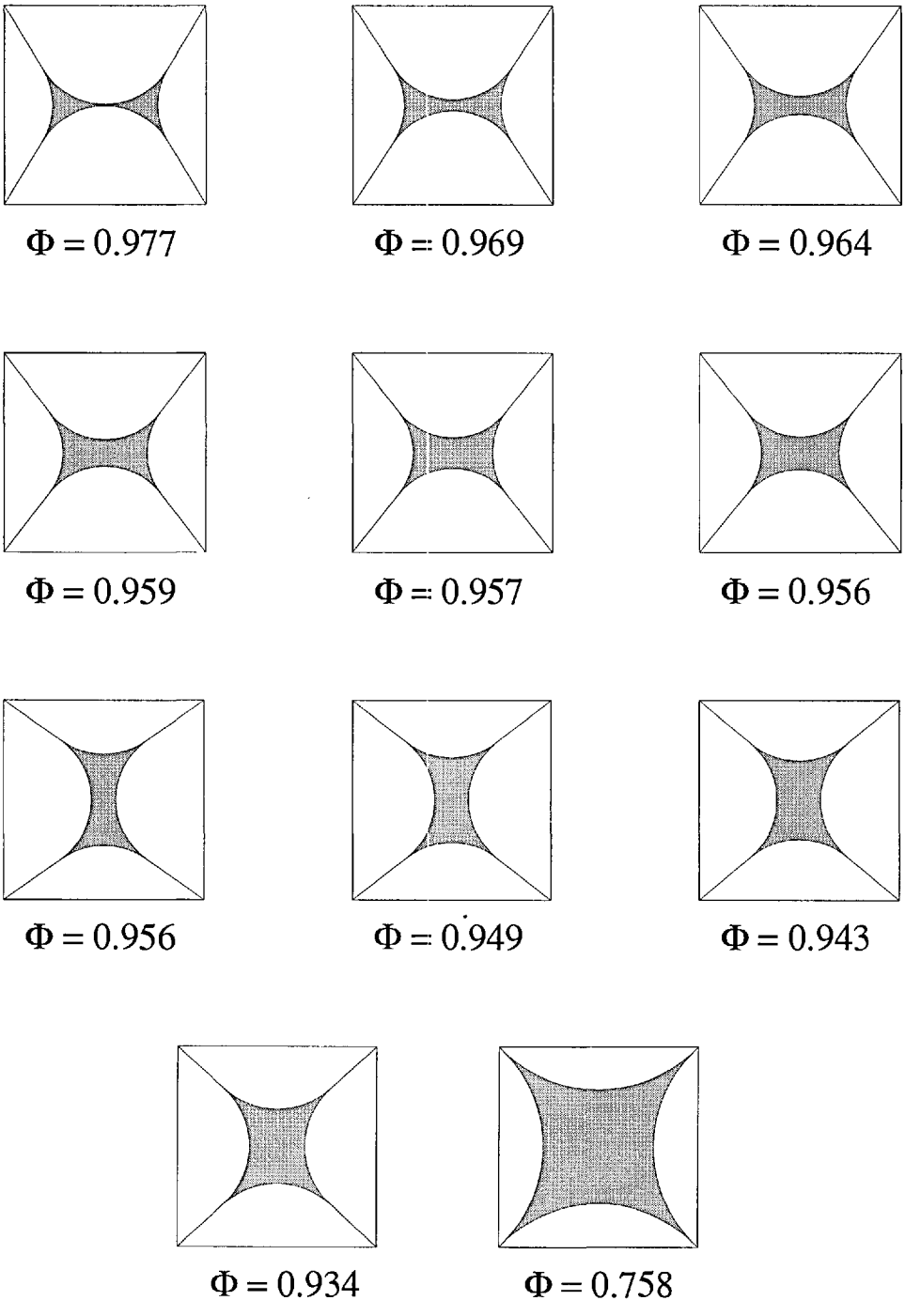

Figure 6.13: Behaviour of foam with $\beta = 1.01$

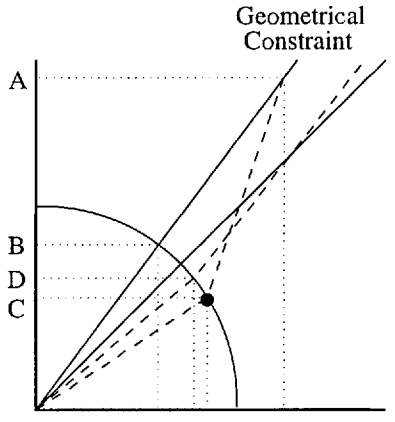

Figure 6.14: Border diagram for foam with large α

trophe theory. We refer back to Fig. 2.14, which showed a wet catastrophe fold. An unstrained vertex would be towards the left of the diagram, and increasing its fluid content would merely move it backwards across the sheet. However, if we strain a vertex we move it towards the fold. If we stop short of forcing a T1, and then increase the fluid content the vertex moves along the equilibrium surface towards the rear. However, as we explained in Chapter 2, the path is not parallel to the fold but moves towards it. Thus at some point the vertex is forced to jump from the upper sheet to the lower sheet across the fold. This is the occurrence of the T1 event. Subsequently the vertex moves as normal along the sheet. In the same way as normal if the fluid content is reduced the vertex will not return to its original configuration, thus alternating the fluid content relaxes strain in the foam.

Now we will derive the equations to describe the border development. We define W to be the width of the box-cell, and D to be its height. θ is shown in Fig. 6.7, as are r the radius of curvature of the border boundary and d the border width at the centre. As before the gas volume is u_g, which is fixed, and at disintegration the bubbles are circular with radius R. α is the ratio of b to a, and we now define β as

$$\beta = \frac{D_0}{W_0} = \frac{\alpha\sqrt{3}}{(2+\alpha)} \tag{6.35}$$

First we shall obtain the value of Φ at the disintegration point. It is evident that at disintegration each bubble is the circumscribing sphere of one of the box cells shown in Fig. 6.8. This means that

$$R^2 = \left(\frac{W}{2}\right)^2 + \left(\frac{D}{2}\right)^2 \tag{6.36}$$

so that

$$R^2 = \frac{a_0}{4\Phi_d}\left((2+\alpha)^2 + 3\alpha^2\right) \tag{6.37}$$

but we also know

$$R^2 = \frac{u_g}{\pi} = \frac{2a_0^2\alpha\sqrt{3}(2+\alpha)}{\pi} \tag{6.38}$$

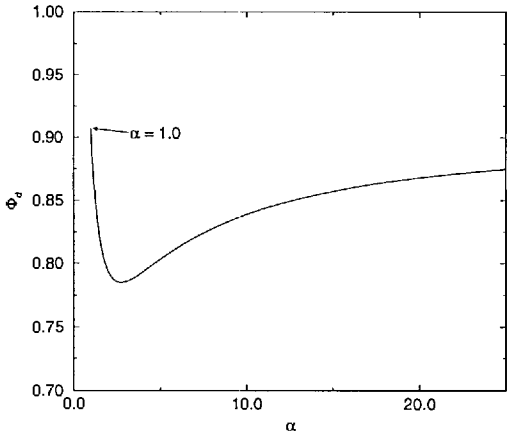

Figure 6.15: Φ_d against α

so we have finally

$$\Phi_d = \frac{\pi(1+\alpha+\alpha^2)}{2\alpha\sqrt{3}(2+\alpha)} \tag{6.39}$$

Once again we can apply our check against Princen's result by setting $\alpha = 1$, so that we get $\Phi_d = \pi/2\sqrt{3}$. Φ_d is plotted against α in Fig. 6.15. We should briefly explain the shape of the curve in this figure. Here we show the values of Φ_d for $\alpha > 1$; these join to the values for $\alpha < 1$, see Fig. 6.19, in a cusp. The part of the curve running down to the minimum corresponds to those configurations where no T1 event occurs, so that the the foam moves smoothly from having one thick film to disintegration. The part rising from the minimum corresponds to those configurations where a T1 occurs. At the T1 the configuration flips, mapping the foam onto the other section of the curve, with $\beta' = \beta^{-1}$, or $\alpha' = (2+\alpha)/(\alpha-1)$.

At this point we know that

$$\theta = \theta_d = \frac{\pi}{2} - \arctan\left[\frac{2D}{2W}\right] = \frac{\pi}{2} - \arctan[\beta] = \frac{\pi}{2} - \arctan\left[\frac{\alpha\sqrt{3}}{(2+\alpha)}\right] \tag{6.40}$$

Now we can solve for both Π and Φ as functions of θ in the range $\pi/6 > \theta > \theta_d$ as discussed above. As the configuration is defined by θ and β we can do the calculations for $W = 1$ and scale up by $a_0(2+\alpha)/\Phi^{1/2}$. We have that

$$b\sin\theta = D/2 \tag{6.41}$$

and

$$a + b\cos\theta = W/2 \tag{6.42}$$

whilst

$$d = r(2\cos\theta - 1) \tag{6.43}$$

and

$$r = (a + d\cot\theta)\cot(\theta/2) \tag{6.44}$$

imply that

$$r = \left(\frac{W}{2} - \frac{D}{2}\cot\theta\right)\tan\theta\,(1+\tan(\theta/2)\tan\theta - 2\cos\theta)^{-1} \quad (6.45)$$

$$= \frac{1}{2}(1-\beta\cot\theta)\tan\theta\,(1+\tan(\theta/2)\tan\theta - 2\cos\theta)^{-1} \quad (6.46)$$

where we have set $W = 1$. Now we have

$$u_l = (8\sin\theta\cos\theta - \pi)r^2 \quad (6.47)$$

$$= \frac{(8\sin\theta\cos\theta - \pi)}{4}\frac{(1-\beta\cot\theta)^2\tan^2\theta}{(1+\tan(\theta/2)\tan\theta - 2\cos\theta)^2} \quad (6.48)$$

so that with

$$\Phi = 1 - \frac{u_l}{u_g} = 1 - \frac{u_l}{2W_0D_0} = 1 - \frac{u_l}{2\beta} \quad (6.49)$$

Finally

$$\Phi = 1 - \frac{(8\sin\theta\cos\theta - \pi)}{8\beta}\frac{(1-\beta\cot\theta)^2\tan^2\theta}{(1+\tan(\theta/2)\tan\theta - 2\cos\theta)^2} \quad (6.50)$$

To obtain Π we need

$$\Pi = -\sigma\left(\frac{dl}{du_l}\right)_{u_g} = -\sigma\left(\frac{dl}{d\theta}\frac{d\theta}{du_l}\right) \quad (6.51)$$

where u_g is implicitly fixed in our working. From scaling up Eq. 6.48 we obtain $\frac{du_l}{d\theta}$, and we have

$$l = (8b - 8r\cot\theta + 2\pi r)\frac{a_0(2+\alpha)}{\Phi^{1/2}} \quad (6.52)$$

$$= \frac{a_0(2+\alpha)}{\Phi^{1/2}} \times \left(\frac{4\beta}{\sin\theta} - (4\cot\theta - \pi)(1-\beta\cot\theta)(1+\tan(\theta/2)\tan\theta - 2\cos\theta)^{-1}\right) \quad (6.53)$$

from which we obtain $\frac{dl}{d\theta}$. Thus we have Π as a function of θ, which we use with Eq. 6.50 to obtain Π as a function of Φ. Π is plotted in Fig. 6.20 for a few different $\alpha > 1$.

Two thick, one thin — $\alpha < 1$

Now we will derive the equations describing the behaviour, we define D, W, β and α as before, where now $0 < \alpha < 1$, the other variables are defined in Fig. 6.17.

We will first obtain the value of Φ_d. We know that

$$2r = 2D = \frac{2\beta W_0}{\Phi^{1/2}} \quad (6.54)$$

and at disintegration

$$r = R = \sqrt{u_g/\pi} \quad (6.55)$$

so that

$$\Phi_d = \frac{\pi\sqrt{3}\alpha}{2(2+\alpha)} \quad (6.56)$$

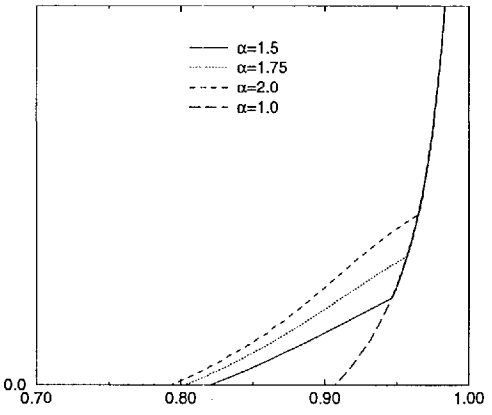

Figure 6.16: Π against Φ for a few $\alpha > 1$

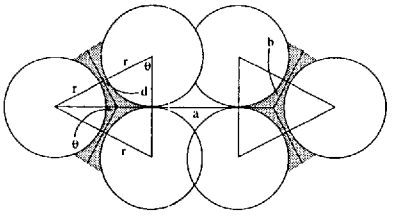

Figure 6.17: Vertex with two thick films

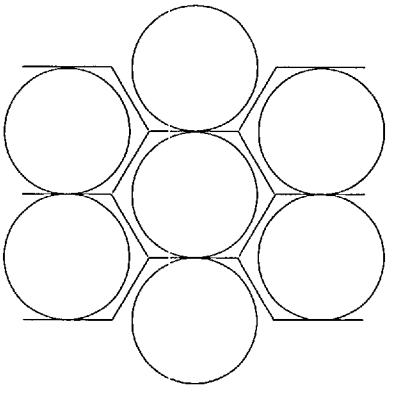

Figure 6.18: Disintegration of two thick film foam

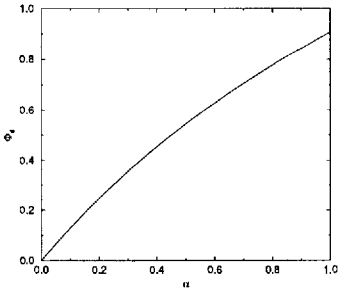

Figure 6.19: Φ_d against α

To obtain the value of θ_d we note that

$$\theta_d = \arctan\left[\frac{R}{W}\right] = \arctan\left[\frac{D_0}{W_0}\right] = \arctan\left[\frac{1}{\beta}\right] \tag{6.57}$$

so that

$$\theta_d = \arctan\left[\frac{2+\alpha}{\alpha\sqrt{3}}\right] \tag{6.58}$$

a and b obey the same equations

$$b\sin\theta = D/2 \tag{6.59}$$

$$a + b\cos\theta = W/2 \tag{6.60}$$

$$\tag{6.61}$$

whereas r is now given by

$$r = D = \beta W = \beta \tag{6.62}$$

where we once again set $W = 1$, and scale up by $a_0(2+\alpha)/\Phi^{1/2}$. We also have that

$$u_l = r^2(2\tan\theta - \pi) = \beta^2(2\tan\theta - \pi) \tag{6.63}$$

so that

$$\Phi = 1 - \frac{u_l}{u_g} = 1 - \frac{\beta^2(2\tan\theta - \pi)}{2W_0D_0} = 1 - \frac{\beta(2\tan\theta - \pi)}{2} \tag{6.64}$$

whilst

$$l = 2 + 2r(\pi - \tan\theta) \tag{6.65}$$

again with $W = 1$.Now if we scale up we obtain

$$u_l = \beta^2(2\tan\theta - \pi)\frac{a_0^2(2+\alpha)^2}{\Phi} \tag{6.66}$$

$$l = \frac{(2 + 2\beta(\pi - \tan\theta))a_0(2+\alpha)}{\Phi} \tag{6.67}$$

which together with

$$\Pi = -\sigma\left(\frac{dl}{d\theta}\frac{d\theta}{du_l}\right) \tag{6.68}$$

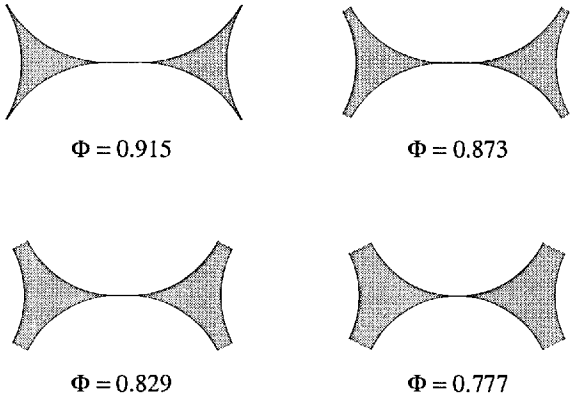

Figure 6.20: Development of a foam with $\alpha < 1$

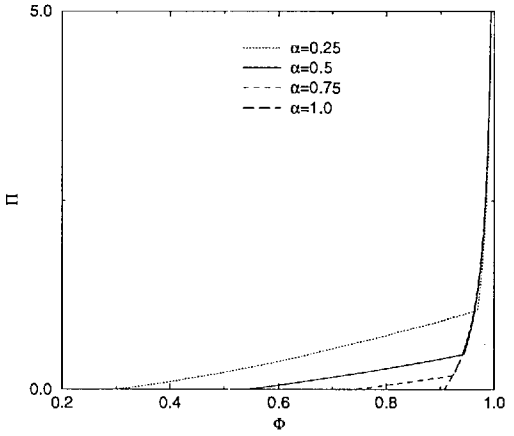

Figure 6.21: Π against Φ for a few $\alpha < 1$

gives us that

$$\Pi = -\frac{\sigma \mathcal{F}^{1/2}}{4\sqrt{6} a_0 \alpha} \left(2 + \frac{2\alpha\sqrt{3}\,(\pi - \tan\theta)}{2+\alpha} - 2\mathcal{F} \right) \tag{6.69}$$

where we have defined

$$\mathcal{F} = 2 - \frac{\sqrt{3}\alpha\,(2\tan\theta - \pi)}{2+\alpha} \tag{6.70}$$

Now by using the equations for R and Φ_d, and solving Eq. 6.64 for $\tan\theta$ in terms of Φ, we can obtain

$$\Pi = -\frac{\sigma}{2R} \left(\frac{\Phi}{\Phi_d} \right)^{1/2} (\Phi - \Phi_d) \tag{6.71}$$

6.2.2 Three distinct film lengths

Now we can generalize our treatment above to the case featuring 3 distinct film lengths, which is the case we need for our VEM approach. The case is not much more complex, just a little more opaque.

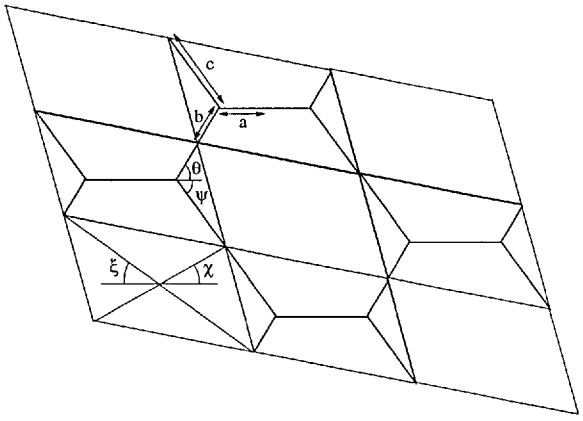

Figure 6.22: Constructing a disordered foam with box-cells

We name the three films a, b and c in order of increasing length. We also define $b_0 = \beta a_0$ and $c_0 = \gamma a_0$. We can construct the foam as shown in Fig. 6.22, and define box-cells in the same way as before. The area of the original cell is

$$u_g = 2\sqrt{3}a_0^2(\beta + \beta\gamma + \gamma) \tag{6.72}$$

It is evident that there will be four major regimes, which are; foam with three thin films, foam with one wet film, foam with two wet films, and disintegrating foam. We follow Kraynik et al. [87] in calling these regimes phases I, II, III and IV respectively. We start by obtaining expressions for the configurations at which the foam changes from one phase to another.

The foam starts in Phase I, with three thin films and a Plateau border. The transition to Phase II, with one thick film and two thin films, occurs when

$$r = \left(\frac{u_g\,(1-\Phi)}{2Q\Phi}\right)^{\frac{1}{2}} = \frac{a_0\sqrt{3}}{\Phi^{1/2}} \tag{6.73}$$

so that

$$\Phi_c = 1 - \frac{\sqrt{3}Q}{(\beta + \beta\gamma + \gamma)} \tag{6.74}$$

and evidently both θ_c & $\psi_c = \pi/3$. The transition to Phase III, with two thick films and one thin film, occurs at the stage shown in Fig. 6.23 (we denote the values of variables at the second transition with a subscript 's'). At this point, and throughout Phase III, the arcs subtend π radians so that

$$\theta_s = \pi/2 - \arctan\left[\frac{\sqrt{3}\beta}{2+\beta}\right] \tag{6.75}$$

and at the transition point $\psi_s = \theta_s$. Thus the film length f is equal to the difference between the lengths b and c, which can be determined from θ_s and the requirement that the a line is still aligned as it was initially. This gives us

$$f_s = \sqrt{3}\frac{(\gamma - \beta)(1 + \beta + \beta^2)^{1/2}}{2+\beta} \tag{6.76}$$

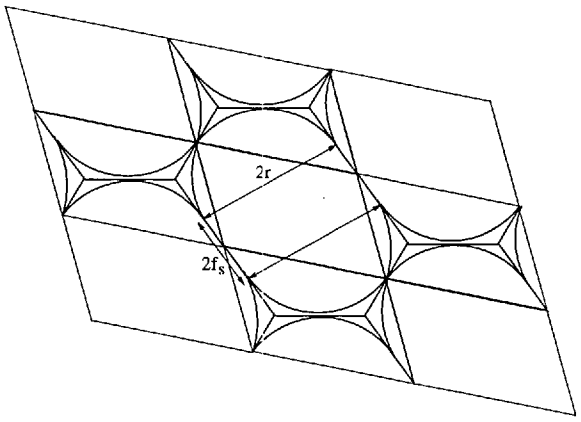

Figure 6.23: Foam at Phase II → Phase III

and thus

$$\Phi_s = \frac{(1+\beta+\beta^2)}{\sqrt{3}(\beta+\beta\gamma+\gamma)}\left(\frac{\pi}{2}+\frac{2\sqrt{3}(\gamma-\beta)}{2+\beta}\right) \tag{6.77}$$

At Φ_d the foam disintegrates, and the cells become circular bubbles, so that

$$R^2 = \frac{(1+\beta+\beta^2)a_0^2}{\Phi} \tag{6.78}$$

and we know that $\pi R^2 = u_g$, so

$$\Phi_d = \frac{\pi}{2\sqrt{3}}\frac{(1+\beta+\beta^2)}{(\beta+\beta\gamma+\gamma)} \tag{6.79}$$

We also know that the b film is perpendicular to the long diagonal of the box-cell, so

$$\psi_d = \pi/2 - \arctan\left[\frac{\sqrt{3}\gamma}{2+\gamma}\right] \tag{6.80}$$

All these expressions can be checked against Princen's result with $\beta = \gamma = 1$, and also with our previous results with $\beta = \gamma = \alpha$ for the previous case with $\alpha > 1$, and with $\beta = 1$ & $\gamma = \alpha^{-1}$ for the previous case with $\alpha < 1$.

Now we turn to the derivation of the equations determining the relation between Π and Φ. During Phase I the foam maintains its original geometry, with the addition of a Plateau border. This phase is governed by similar equations to those in the previous study, so that we skip the details (which can be found in Appendix D), and find

$$\Pi = -\frac{\sigma}{R}\frac{2}{\beta+\beta\gamma+\gamma}\left(\frac{\beta+\beta\gamma+\gamma-\sqrt{3}Q}{2\pi\sqrt{3}}\right)\left(\frac{\Phi}{\Phi_c}\right)^{\frac{1}{2}}\left[\beta+\gamma+1-(\beta+\beta\gamma+\gamma)\left(\frac{1-\Phi_c}{1-\Phi}\right)^{\frac{1}{2}}\right] \tag{6.81}$$

During Phase II the foam has ψ & θ equal, so that we can proceed as before, and leaving the details to Appendix D, we find

$$u_l = \frac{a_0^2(8\sin\theta\cos\theta-\pi)}{\Phi}\left(\frac{(2+\gamma\sqrt{3})\tan\theta-\gamma\sqrt{3}}{2(1+\tan(\theta/2)\tan\theta-2\cos\theta)}\right) \tag{6.82}$$

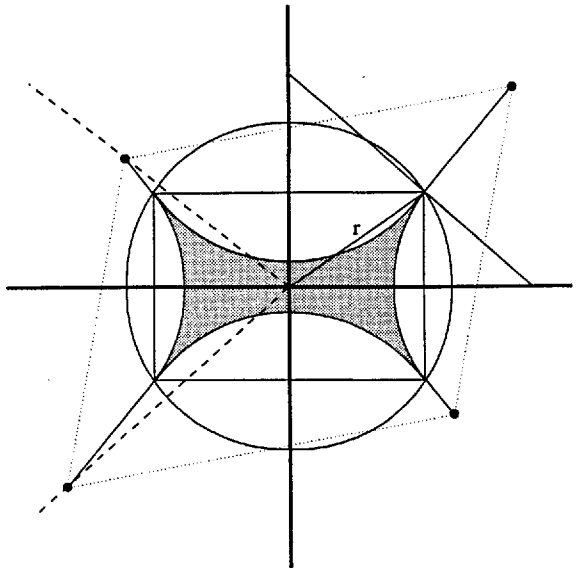

Figure 6.24: Border diagram for Phase II

and

$$l = \left(\frac{a_0}{\Phi^{1/2}}\right)\left(\frac{4\sqrt{3}(\gamma+\beta)}{2\sin\theta} + \frac{(\pi - 4\cot\theta)\left((2+\gamma\sqrt{3})\tan\theta - \gamma\sqrt{3}\right)}{1+\tan(\theta/2)\tan\theta - 2\cos\theta}\right) \tag{6.83}$$

so that we can calculate Π as before. This enables us to obtain both Π and Φ as functions of θ for $\theta_c > \theta > \theta_s$. We have one more detail to concern us in Phase II, we can have T1 flips brought on by the strain stored in the foam. We can treat this in the same way as in the previous case, by using the border diagram. Such a diagram is shown in Fig. 6.24. It shows the border with its four neighbouring thin films. The dotted line is the box-cell for the foam, note that it is skewed by the difference in the film lengths. The inner-box is however the same as before, because the alignment of the a film is kept in Phase II. The corners of the box-cells move along the dashed lines, but now there are two separate constraints.

In Phase III we have Eq. 6.78, so that the only changing feature is the length of the thin film f which runs between $f_s > f > f_d = 0$, where

$$f_s = \frac{(\gamma-\beta)\sqrt{3}}{2+\beta}(1+\beta+\beta^2)^{1/2} \tag{6.84}$$

This enables us to evaluate this stage explicitly, see Appendix D, obtaining

$$\Pi = \frac{\sigma}{2R}\left(\frac{\Phi}{\Phi_d}\right)^{\frac{1}{2}}(\Phi - \Phi_d) \tag{6.85}$$

6.3 VEM for Osmotic Pressure

Now that we have the dependency of the osmotic pressure Π on the volume fraction Φ for an ordered foam with three different film lengths we can use the VEM to make a prediction

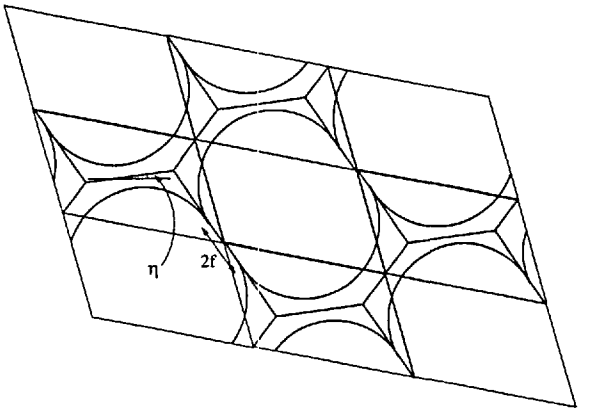

Figure 6.25: Foam in Phase III

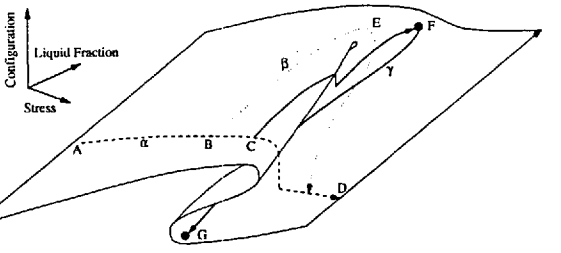

Figure 6.26: Π against Φ for a few $\beta\&\gamma$

for disordered foams. This is done by numerically integrating the results over the vertex distribution, which we extract from our relaxed Voronoi creator. The total Π curve is shown in Fig. 6.27 for a disordered foam, and can be compared to the simulation result shown in Fig. 2.47. Clearly the model shows the same kind of deviations from the Princen result as are found in the simulations, although the deviations we find are much larger and our Π is non-zero over a much larger range.

These results require some discussion. There are shortcomings in both approaches, simulation and theory. The simulation can only be carried out for a very small foam sample, and therefore the results are noisy and also may not be representative. A small sample may not support large levels of cell shape disorder for example. The theory on the other hand errs in the opposite direction. Whilst the calculations we made for the irregular hexagonal foams are correct, they hold for highly constrained systems. Such vertices arising in the context of a disordered foam would not explore their whole range of configurations but would be perturbed by their neighbours. However in our model even the most highly irregular vertices explore their whole range of configurations, which leads to non-zero contributions to Π even down to $\Phi = 0+$. This leads to an unrealistically long tail for our result. Nevertheless the spirit of the calculation seems correct, and the form of the curve is close to that found by Weaire. Weaire et al. used a simple argument citing the linear variation of the bulk modulus which can be supported on a

If we assume that the osmotic pressure is the main force acting in the equilibrium foam, which effectively means that the capillary pressure is much larger than the hydrostatic pressure variation over one bubble diameter

$$2\sigma/R >> 2R\Delta\rho g \tag{6.86}$$

where $\Delta\rho$ appears because it is the excess mass of the liquid fraction which pulls it down. Then the gradient of the osmotic pressure must support the fluid fraction in the foam relative to the bulk of the foam. This assumption holds in the foams we are interested in. First we consider a regular ordered foam, then we examine the tail of the curve for the 3 distinct film lengths case, the other cases are simple extensions of the argument.

We have

$$\Pi = \frac{\sigma}{R\sqrt{1-\Phi_l^c}}(1-\Phi_l)^{1/2}\left[\left(\frac{\Phi_l^c}{\Phi_l}\right)^{1/2} - 1\right] \tag{6.87}$$

where $\Phi_l = u_l/u_t$, u_t is the total volume per unit cell, u_l is again the liquid volume per unit cell, σ the surface tension and R the bubble radius. We model the form of a foam on a liquid reservoir in a gravitational field g. The similar case of an emulsion with either buoyancy or centrifugal forces acting can be modelled by changing parameters. The lowest layer of foam is in the close packing configuration with $\Pi = 0$ and $\Phi = \Phi_l^c$. We call this plane $z = 0$ with the z-axis pointing upwards.

Force balance gives us

$$\frac{d\Pi}{dz} = u_l\Delta\rho g = \frac{d\Pi}{du_l}\frac{du_l}{dz} \tag{6.88}$$

or

$$\frac{du_l}{dz} = u_l\Delta\rho g\left(\frac{d\Pi}{du_l}\right)^{-1} \tag{6.89}$$

Now we take it that the cells are of constant size throughout the foam stack, as is the case with well controlled foam production and without coarsening. This means that u_g is constant throughout the foam. So with

$$\Pi(u_t) = \frac{\sigma u_g^{1/2}}{R\sqrt{1-\Phi_l^c}}\left[\left(\frac{\Phi_l^c}{u_g}\right)^{1/2} - u_t^{-1/2}\right] \tag{6.90}$$

so that

$$\frac{d\Pi}{du_l} = \frac{d\Pi}{du_t} = \frac{\sigma u_g^{1/2}}{2u_t^{3/2}R\sqrt{1-\Phi_l^c}} \tag{6.91}$$

so we now have

$$\frac{du_l}{dz} = \frac{2u_t^{3/2}(u_t-u_g)\Delta\rho g R\sqrt{1-\Phi_l^c}}{\sigma u_g^{1/2}} \tag{6.92}$$

Now if we transform using $x^2 = u_g$ and $2u_g^{1/2}dx = du$ we have

$$\frac{dx}{dz} = \alpha x^2(x^2 - u_g) \tag{6.93}$$

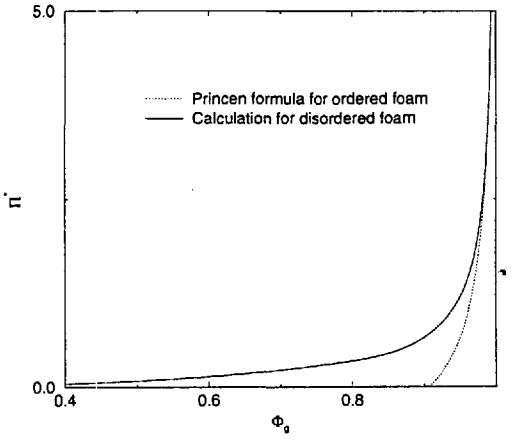

Figure 6.27: Π for ordered & disordered foams

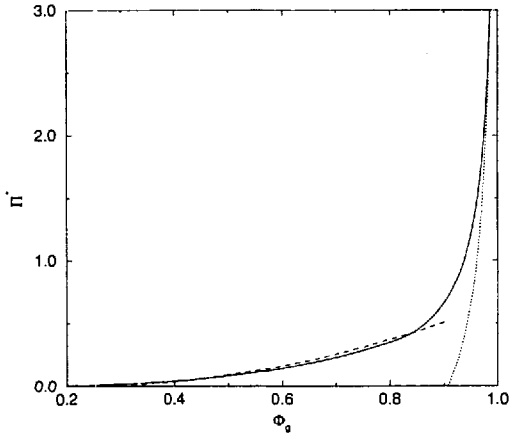

Figure 6.28: Fitted tail of Π

rigidity percolation basis, and the fact that the bulk modulus is the first derivative with respect to Φ of Π. This leads us to expect a quadratic tail for Π, and indeed they found that their data could be fitted in this manner. We, see Fig. 6.28, find that our data also fits a quadratic though with considerably different parameters. Thus our data also roughly fits into the rigidity percolation picture.

6.4 Stationary State of Drained Foam

In Section 2.9 we briefly introduced the topic of foam drainage. Now that we have a form for the osmotic pressure of foam as a function of liquid fraction we can make a prediction for the equilibrium form of a drained foam.

Again we use

$$\frac{du_l}{dz} = u_l \Delta\rho g \left(\frac{d\Pi}{du_l}\right)^{-1} \tag{6.100}$$

with

$$\frac{d\Pi}{du_l} = \frac{d\Pi}{du_t} = \frac{\sigma u_g^{3/2}}{2u_t R\Phi_d^{1/2}} \left(-\frac{3u_t^{-3/2}}{2} + \frac{\Phi_d u_t^{-1/2}}{2u_g}\right) \tag{6.101}$$

so we now have

$$\frac{du_l}{dz} = \frac{4\Delta\rho g R\Phi_d^{1/2}}{\sigma u_g^{3/2}} \frac{(u_t - u_g)u_t^{3/2}}{\frac{\Phi_d u_t}{u_g} - 3} \tag{6.102}$$

Finally this gives us

$$\Phi_l(z) = 1 - 2\left(1 + \tanh\left[\frac{u_g}{2}\left(\kappa - \frac{\Delta\rho g R\sqrt{1-\Phi_l^c}}{\sigma u_g^{1/2}} z\right)\right]\right)^{-1} \tag{6.103}$$

Here κ must be fixed so that $\Phi_l(0) = \pi/2\sqrt{3} = 0.093$, which means that $\kappa = 2.56$. $\Phi_l(z)$ is plotted in Fig. 6.29. As expected the longer tail of the osmotic pressure curve for the irregular hexagonal foam gives rise to a changed profile, with a less rapid drop in liquid fraction.

Similar arguments can be applied to the other cases with very similar results. We can also numerically evaluate the expression for the case of the disordered foam, using our expressions for Π obtained above. To handle this case we need to use a slightly different approach. We look at the osmotic pressure as balancing the net upwards force of the buoyancy of all the bubbles below the liquid surface [126]. Thus

$$\Pi(\Phi) = \Delta\rho g \int_0^z \Phi(x)dx \tag{6.104}$$

This forms a constraint on Π and Φ. Clearly if $\Pi = \Pi(\Phi)$ alone then Φ must be a unique function of $\Delta\rho g z = \tilde{z}$. Thus

$$\Pi(\Phi) = \int_0^{\tilde{z}} \Phi(x)dx \tag{6.105}$$

which implies that

$$\tilde{z}(\Phi) = \int_0^{\Pi} \frac{d\Pi(\Phi)}{\Phi} \tag{6.106}$$

This final equation allows us to obtain numerical results for $\Phi(z)$ from numerical results for $\Pi(\Phi)$. Such results are shown in Fig. 6.30, and are evidently close to those for the ordered case. This is due to the bulk of the films being close to the average length. The slight tail of the disordered osmotic pressure curve compared to the Princen result does give a slight increase in the liquid fraction at small z.

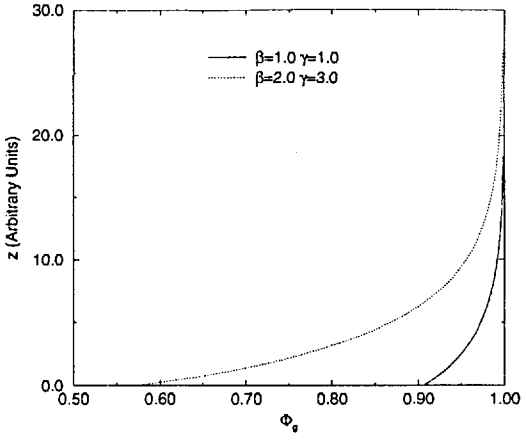

Figure 6.29: z against $\Phi_l(z)$ for regular and irregular foams

where

$$\alpha = \frac{\Delta\rho g R\sqrt{1-\Phi_l^c}}{\sigma u_g^{1/2}} \tag{6.94}$$

Now transforming again with $y = x^2 - u_g/2$ we have

$$\frac{dy}{dz} = \alpha\left(y^2 - \frac{u_g^2}{4}\right) \tag{6.95}$$

which yields

$$y = \frac{u_g}{2}\tanh\left[\frac{u_g}{2}(\kappa - \alpha z)\right] \tag{6.96}$$

where κ is an arbitrary constant. Finally this gives us

$$\Phi_l(z) = 1 - 2\left(1 + \tanh\left[\frac{u_g}{2}\left(\kappa - \frac{\Delta\rho g R\sqrt{1-\Phi_l^c}}{\sigma u_g^{1/2}}z\right)\right]\right)^{-1} \tag{6.97}$$

Here κ must be fixed so that $\Phi_l(0) = \pi/2\sqrt{3} = 0.093$, which means that $\kappa = 8.79$. $\Phi_l(z)$ is plotted in Fig. 6.29.

We now briefly show the result for the case of an irregular hexagonal foam with 3 distinct film lengths. We are interested here in the start of the curve, at small z where the osmotic pressure dependence is more markedly different from the Princen result. We expect some modification of the equilibrium foam profile.

We have now that

$$\Pi = \frac{\sigma}{2R}\left(\frac{\Phi}{\Phi_d}\right)^{1/2}(\Phi - \Phi_d) \tag{6.98}$$

Again the lowest layer of foam is in the close packing configuration with $\Pi = 0$ and $\Phi = \Phi_l^c$, and we call this plane $z = 0$ with the z-axis pointing upwards. Now we rewrite Π in terms of u_t, the total volume per unit cell, recalling that u_g is constant.

$$\Pi(u_t) = \frac{\sigma}{2R}\frac{u_g^{3/2}}{\Phi_d^{1/2}}\left(u_t^{-3/2} - \frac{\Phi_d}{u_g}u_t^{-1/2}\right) \tag{6.99}$$

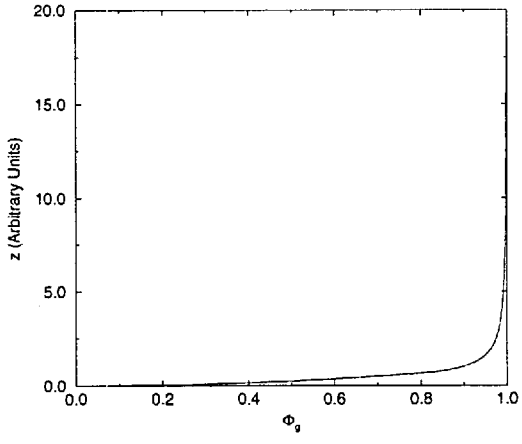

Figure 6.30: $\Phi_l(z)$ against z for a disordered foam

can lead to yield stress.

By using a simple probabilistic model we can attack on both these fronts. We can directly study disordered foams, which are the systems of experimental interest, and we can abstract the structure of the foam so as to eliminate irrelevant features. Furthermore, because of the focus on important elements, we can carry out calculations on a scale which is beyond the more literal simulation. We chose to use the vertices of the foam as the primitive element, thus directly incorporating the methodology already used by Princen et al. [73, 81] into our model. The use of a probability distribution over the vertex configuration space generalized the model to cope with disorder. By choosing this element, and discarding long range structural information we freed ourselves from an exact representation of the foam, so that we could concentrate on those features deemed to be essential. The results have clearly shown that the main features of foam flow and deformation can be explained using only local, vertex, properties.

When seeking to evaluate our results we have mostly used simulation results from the work of Kawasaki et al. and Weaire et al., because of the lack of detailed experimental results available. However, where possible we used these experimental results. We found that our model compares very favourably with the work of both these groups. The model was used both in simple shear and extensional shear. In both cases the model predicted a yield stress of the right order of magnitude, and in the simple shear case the results were then compared with the experimental results of Khan [76] and found to agree closely. Furthermore the shape of the stress-strain curves in both simulations were closely reproduced.

The resulting picture of foam rheology can be easily stated. Foams are fairly closely modelled by the Bingham fluid picture. They have an initial elastic reaction to strain, with the stress increasing more or less linearly up to a yield stress. At the yield stress the foam begins to plastically deform, and the stress is then constant to within a range of around 10% of the yield stress value. Further investigations, summarized below, have confirmed the Bingham fluid dependance of the yield stress on strain rate. Further features which are apparent in the simulations have been reproduced, which are not clearly experimentally supported as yet. The foremost of these is the linear decrease in yield stress of around 30% which is seen as the strain increases just after yield in simple shear.

The model offers simple explanations for these features, and the close match to results clearly singles out the important features of foam. The origin of the yield behaviour is the T1 event which occurs when vertices have one film with length zero, which is the crucial feature in the otherwise simple 'vertex map', Chap. 4. This map is evidently sufficient to encapsulate the behaviour of the deforming foam, without the addition of interactions between vertices or more complex (and accurate) vertex dynamics. The difference between the results of Kraynik et al. [81] and those of our model arise simply from the distribution of vertices, not from any cooperative phenomena. Nevertheless, as discussed below and in Chap 4, this map has a very

Chapter 7

Conclusions

In this chapter we briefly summarise the conclusions which this work has led to, and discuss shortly some possible extensions of the work.

7.1 Conclusions

7.1.1 Rheological Behaviour

In this thesis we have developed a model of disordered foam built upon a simple probabilistic basis. We have identified one class of elements of the foam which are in some sense 'atomic', so that the whole foam can be constructed from these elements alone. The foam is then modelled by studying the behaviour of a distribution over the configuration space of these elements, as it is perturbed by external actions. This is the first time such an approach has been used to attack the problems of foam rheology and osmosis. It contrasts with the previous work done in this area, which is collected into two classes; simulation and exact modelling of ordered foam. Simulations were initially used to see what processes were going on inside foams, during cell growth, flow and fluid fraction changes. They were effective but can not offer a simple model as they represent the whole system at some level of approximation, and therefore offer limited insight into which are the most important features of foam. The exact modelling approach explains some features (e.g. yield stress) in terms of processes in a physical model (T1 events), and thus gives more insight into the important features. However the structures which are amenable to modelling are highly symmetric, and thus quite unlike the disordered foams which we come across in experiments. Furthermore the symmetry leads to very strong artefacts in the results (e.g. discontinuities in curves where all cells in the foam undergo the same events), which mean that they must be interpreted as giving order of magnitude estimates of important quantities, which can be obtained by far easier routes [69]. The results do not give any useful qualitative information about disordered foams either, only support a mechanism which clearly

local map appears to be adequate to the task, producing qualitatively and quantitatively close matching results. The model also uncovered some interesting behaviour in the behaviour of 'irregular ordered foams'. Princen's work considered only the foam formed by regular hexagonal cells, but to formulate the VEM model the work needed to be extended to the more general ordered foam, with irregular hexagonal cells. Such a foam can be created by deforming a regular hexagonal foam, and stores stress. The behaviour of these foams is much richer than that of the ordered example, with some retaining a positive osmotic pressure (in principle) until $\phi_l = 1.0$. The mechanism of stress release also illuminates the ordering of foams by fluid content cycling, and the complexities of wet foam rheology.

The success of this approach enabled us to calculate some additional characteristics, which have not previously been studied. The equilibrium liquid profile of a foam which has drained in a gravitational field (or indeed a centrifuge) can be calculated, for both the ordered and disordered cases. As yet there are no experimental results for comparison, but with the renewed interest in drainage this should soon be resolved.

7.2 Future Work

This work suggests several further interesting tasks we can set ourselves, both in terms of further using the VEM, of extending the VEM to cover other types of foam, using the VEM with other methods to do more accurate calculations, and studying the vertex map and relatives to understand the links between it and the SOC-like spectrum.

7.2.1 Further Use of the VEM

Firstly it would be interesting to use the VEM on a set of different initial distributions. In addition to using the Voronoi diagram it should be possible to check the predictions of the model further by starting with an ensemble derived from a foam simulation such as that of Weaire or Kawasaki. It would also be interesting to try using ensembles of varying disorder; the model will not effectively represent a highly ordered foam but there is a large variation in the μ_2 of initial distributions which should be accessible. Likewise with the osmotic behaviour of foams, it would be instructive to run the VEM with semi-ordered foams, if comparison to experimental results is possible.

Secondly it would be of interest to study in more detail the effects of strain history on foams. We know from preliminary work that the previous history of a foam has a large effect on its reaction to new strains, but that this history wears off quite rapidly under the new strain. However we haven't systematically studied this effect, varying angles between strains and magnitudes of strain applied.

Finally it would be instructive to carry out calculations for more experimental situations.

novel behaviour which produces some astounding effects.

The most surprising conclusion this work has uncovered is that this simple model, consisting of independent vertices governed by a simple dynamic map, can reproduce behaviour which is interpreted in simulations and experiments as arising from self-organized criticality (SOC). This is shocking because SOC behaviour is generally supposed to arise from cooperative dynamics. Somehow the discontinuous nature of VEM map gives rise to vertex orbits, which when combined to give a bulk sample result have the same spectra as seen in simulations exhibiting SOC. This gives rise to several questions.

Firstly, what is the feature of the map which gives rise to this spectrum. Investigation has shown that the answer is that the orbits of 'almost all' vertices are scale invariant. This self-similarity of the orbits gives rise to the classic SOC spectrum. However, exactly which features of the map give rise to the self-similarity is yet to be understood. It clearly relates to the discontinuities at the T1 events, but not the physical discontinuity (the jump) because similar effects are observed with viscous foams which do not have this jump; the discontinuity referred to is the sudden change in the the region of configuration space available to the vertex.

Secondly, has this been observed in other models or systems. To the best of the author's knowledge it has not, at least not within the available literature. This is a somewhat novel means of producing 'fractal' objects. Rather than being defined recursively, or built up by sectioning another orbit, these orbits are themselves generated piece-wise, and yet are self-similar. It should be possible to find a more general class of maps which have this property.

Thirdly, can a similar approach be used to describe other SOC systems, or is this a unique case? If possible this would enable us to model systems such as the sandpile of Bak et al. using a non-cooperative model, using only local interactions. It seems this should be within reach, as (see Chap. 5) the sandpile and stressed foam have a clear correspondence.

7.1.2 Osmotic Behaviour

We discussed earlier the limitations of the simulational and ordered foam approaches to modelling foam rheology. Similar limitations apply when studying the osmotic behaviour of foams. Simulation has led to some very nice results for the osmotic behaviour of 2 dimensional foams, which are not possible to obtain in real experiments. However, once again, it can only give us ideas about which are the important features of the foam causing this behaviour. Princen [126] did however go a long way towards modelling this behaviour using the hexagonal model of foam, the only significant deviation from his calculations being in the tail of the curve, as disproportionation approaches. To attempt to model this regime we clearly need a more flexible approach.

The same model was proposed for this purpose, with the 'vertex map' now determining the behaviour of the vertices as the fluid content of the sample is altered. Once again a purely

do calculations for more general deformation fields, and if possible for self-consistent flow fields. This is clearly not possible at present in the VEM, but we noted in Chap. 5 that improvements in predictions can be made by applying the VEM to smaller regions of the foam, large enough to consist of many vertices (and cells) but small enough to feel a homogeneous deformation. Likewise it seems that flow calculations could be done, using the VEM on small regions in the flowing sample. This should be possible immediately, but much more interesting would be to attack the self-consistent flow problem.

There are a variety of instruments used to measure rheological quantities, several of which are used with foams and emulsions, of which we have considered only one. It is time to compare our model to experiment, rather than to simulation.

7.2.2 Extending the VEM

Primarily the VEM needs to be extended so as to be able to cope fully with calculations for wet foams, both quasistatically and with higher strain rates. This requires some work on the maps used in wet vertex calculations, at present they do not perform well enough to give convincing results. Preliminary results suggest that wet foams behave in much the same way as dry foams, however the effects of strain on the osmotic behaviour have yet to be explored. The form of the orbits of single vertices under the wet vertex map will also be of interest.

The modelling of different initial distributions enables us to study the effects of disorder on stress-strain history. However another interesting and as yet under-developed area is that of creep and the effects of stress history on the order of the foam sample. Both of these effects arise from the action of coarsening on the vertex distribution through its actions on the cell distribution. To fully model creep, the effects of stress on order and the behaviour of slowly strained foam samples (where the coarsening and deformation timescales are comparable) we need to incorporate coarsening into the model. This requires a major change in the model, but seems possible in the general framework of a probabilistic model without detailed geometric information, as this is the framework within which Beenakker constructed his model of coarsening. However joining the two aims will not be easy. The vertices carry no information about the cells they are connected to, and by just adding this information we can get into sticky problems when we consider T1 events. However to fully combine cells and vertices would involve a simulation of the foam, which is also undesirable. We seek a middle ground, which we have yet to find.

Probably the most important, and exciting, development of the VEM would be to study 3 dimensional foams. As yet the theoretical study of 3 dimensional foams has been somewhat lacking, as they are expensive to simulate, and analytically tougher to crack than 2 dimensional foams. There is no von Neumann's law, and no simple structure to start with. However the topology is known, so that the local structure of the vertices is established, which implies that it may be easier to start with the VEM.

7.2.3 Using the VEM

The VEM approach is useful because it enables quantitatively accurate calculations for the simple deformations considered, which clearly replicate foam behaviour and match experiment fairly well. Unfortunately the effects of simple shear are not the effects of everyday interest. As noted in Chap. 1 the situations of interest are generally flow situations, where we would like to

A.1 Algorithms for Voronoi Diagram Generation

Many different algorithms have been invented to construct the Voronoi diagram of a set of points, or equivalently the Delaunay triangulation. Ref. [127] gives a good background to these problems. The majority of algorithms have been developed for diagrams on 2-manifolds, some can be extended to higher dimensional manifolds. These algorithms fall broadly into three classes.

Divide and Conquer

It has been shown, Ref. [128] that a divide-and-conquer algorithm is asymptotically optimal. Many have been developed [127, 129, 130], however they are commonly perceived as complex to code, so that they have not been heavily utilised. Such algorithms partition the point set recursively, until a level is reached at which the resulting point sub-sets are small enough to have a canonical solution. Then the resulting local solutions are merged in a bottom-up breadth-first manner, back up the tree to result in the final solution.

The complexity of such algorithms generally lies in the data structures used, which store all elements of the diagram and their adjacency. This makes them unsuitable for higher dimensional work, where the structures rapidly proliferate.

Growth

Green and Sibson [131] implemented a recursive growth algorithm in 1978, since which time many more have been developed [132, 114, 133, 12, 134]. Such algorithms proceed by picking one point, checking its nearest neighbours to find those who are linked by Delaunay triangles, and thus making the first set of triangles. The set subsequently grows by finding those triangles formed along the perimeter, until the whole set is found.

Such methods once again require sizeable data structures containing all geometric elements of the triangulation, and are also somewhat inefficient.

Incremental Insertion

Incremental insertion algorithms are popular because they are fairly simple to implement, and many have been developed [128, 135, 136, 137, 138, 139, 140, 141, 142, 143, 144, 145]. These algorithms work by sequentially introducing new points into triangulations, and correcting the triangulation. The initial triangulation is either that of the convex hull or some imposed structure.

The advantage of such algorithms are the simplicity of the data structures required, which makes them simple to code and improves their generalisation to higher dimensions.

A.2 Convex Hull Insertion Algorithm

Our algorithm is a modification of the Convex Hull Insertion Algorithm (CHIA) of Tsai and Vonderohe [141, 145]. We will briefly outline the CHIA here, before going on to describe our

Appendix A

Voronoi Insertion Deletion Algorithm

Voronoi diagrams are discussed in detail in Section 3, of Chapter 3. They are also known as Theissen or Dirichlet tesselations. The Voronoi diagram of a set of sites $\mathcal{P}$ is the collection of the Wigner-Seitz cells of all the sites $p \in \mathcal{P}$, we also call these cells Voronoi cells, and of all their sub-simplices. The Wigner-Seitz cell of a site p is defined as the polygon containing those points x which are closer to p than to any other site. The corresponding collection of simplices consists of polygons, edges and points (where edges meet). These points lie at the centers of circles passing through the sites whose cells converge at the point; as three points are sufficient to define a circle the probability P of having more than three cells (or edges) converging at a point is $P = 0$. Thus Voronoi cells share the property of being 3-valent graphs with foams. As a result we can define a geometric dual to the Voronoi diagram, known as the Delaunay triangulation. This triangulation has the property that each triangle has a circumcircle containing no sites, other than the three lying on it. The Delaunay triangle is generally easier to work with, the Voronoi diagram may then be obtained through the duality.

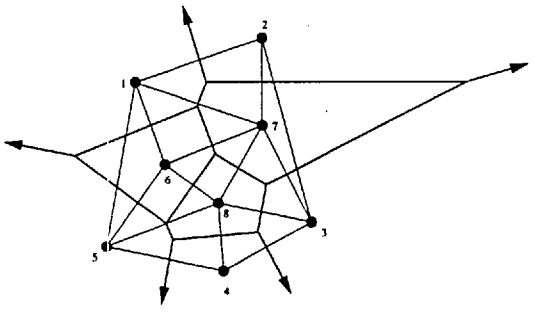

Figure A.1: Voronoi diagram of sites in the plane

Partitioning is necessary to speed up the performance of the convex hull determination, and similar partitioning is used to store the triangles' circumcenters. The partitions are cells covering the area in which the sites lie. The sites are then stored by storing one point per cell directly, with the others indexed from this one. The partitioning is average $\mathcal{O}(\mathcal{N})$, but has worst case $\mathcal{O}(\mathcal{N}^2)$.

Convex hull Evidently the convex hull forms the outer part of the Delaunay triangulation of the sites. The convex hull is found by finding 4 sites which are known to lie on it, say the sites with maximum and minimum x, and y coordinates. Then it is completed by scanning between these points. Again this procedure is average $\mathcal{O}(\mathcal{N})$, but has worst case $\mathcal{O}(\mathcal{N}^2)$.

Triangulation of the convex hull is performed in the same way as the IDA, as shown in Section A.3, using the Delaunay criterion. This process is $\mathcal{O}(\mathcal{N})$.

Insertion and triangulation of other sites is again done as in Section A.3, and is average $\mathcal{O}(\mathcal{N})$, but worst case $\mathcal{O}(\mathcal{N}^2)$.

Finding the dual is also shown below and is $\mathcal{O}(\mathcal{N})$.

A.3 Insertion Deletion Algorithm

There are two reasons for adapting the CHIA for our use. Firstly we would like to improve the performance of the algorithm, and secondly to allow it to be used on a more general class of surfaces, ie spheres and tori. The basic idea of the IDA is that the convex hull is slow to find, and that it is easier to drop this part of the CHIA; the convex hull is also irrelevant to Voronoi diagrams on other (closed) surfaces.

The IDA works by imposing 'extra' sites in addition to those whose Voronoi diagram we wish to find. We add these 'extra' sites in a particular arrangement, whose symmetry enables us to immediately know their triangulation. Then we proceed to add the 'real' sites in one by one, incrementally correcting the Delaunay triangulation. Finally, when all the 'real' sites have been added, we go on to remove the 'extra' sites one by one, leaving us with the Delaunay triangulation of the 'real' sites. Then we use duality to obtain the Voronoi diagram. The only constraint on the 'extra' sites we add is that, if we are working on a space other than the plane, we should add enough sites to avoid any effects due to non-simply-connectedness. In other words we should add enough sites so that no site is its own neighbour.

So the IDA operates as follows

1. Impose 'extra' sites with triangulation : $\mathcal{O}(1)$
2. Insert 'real' sites one by one and triangulate : $\mathcal{O}(\mathcal{N})$

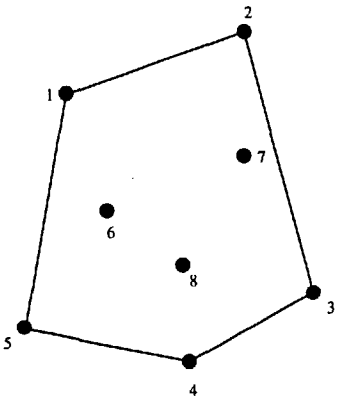

Figure A.2: Convex hull of sites in the plane

algorithm, the Insertion Deletion Algorithm (IDA), in the next section.

Both algorithms rely on the following property of Delaunay triangulations: that the circumcircle of any triangle contains no other sites other than those forming the triangle. This is shown in Section 3. This is used in the CHIA when adding new sites, and in the IDA when adding or removing new sites, The upshot of this fact, known as the Delaunay criterion, is that

1. If the circumcircle of a triangle contains another site it is no longer a Delaunay triangle

2. If a triangle contains no site in its circumcircle then it is a Delaunay triangle

Thus a site which is added only affects those regions of the diagram having triangles containing this site in their circumcircles, and the removal of a site only affects those triangles it was part of.

The CHIA works by finding the convex hull of the set of sites involved. The convex hull is defined as being the 'natural extreme perimeter' of a set of sites. What this means practically is that if we start with a straight line a large distance from the set of sites, aligned along some direction, and then move it towards the set of sites, the first points it touches are members of the convex hull. Alternatively if we surround the set of sites with a noose, and then pull it tight, those points at which it is held constitute the convex hull. The convex hull of our sites in the plane is shown in Fig. A.2.

The CHIA operates as follows

1. Partition the sites into cells

2. Determine the convex hull of the sites

3. Triangulate the convex hull

4. Insert other sites one by one and triangulate

5. Use duality to find Voronoi diagram

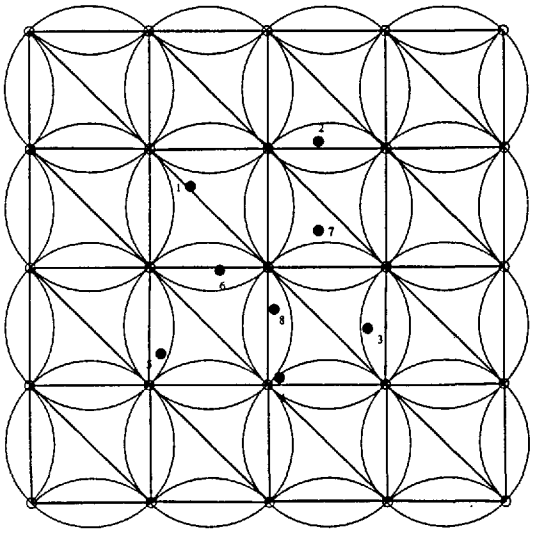

Figure A.4: Triangulated basic set of sites

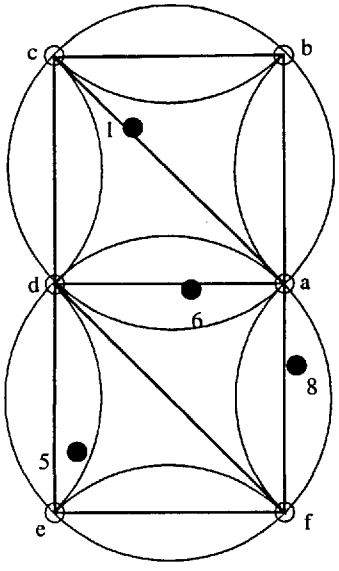

Figure A.5: Environs of sites 1 & 6

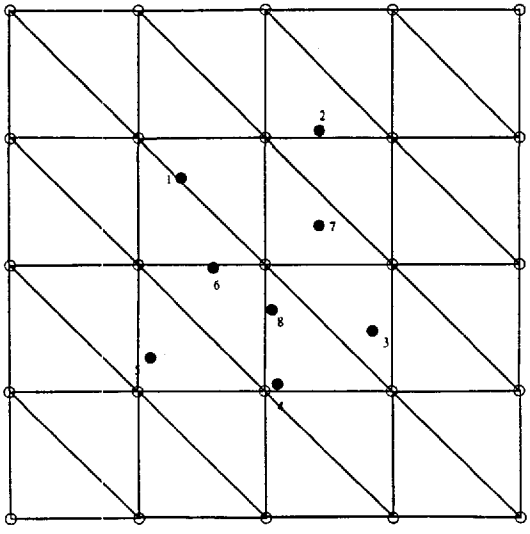

Figure A.3: Extra sites for torus

3. Delete 'extra' sites and correct triangulation : $\mathcal{O}(N)$

4. Use duality to find Voronoi diagram : $\mathcal{O}(\mathcal{N})$

so that the algorithm is $\mathcal{O}(\mathcal{N})$.

A brief explanation of these expectations may be in order. First of all the imposition of the 'extra' sites and their triangulation is $\mathcal{O}(\mathcal{M})$, where $\mathcal{M}$ is the number of 'extra' sites. This is because the triangulation is known through symmetry. Now we can effectively use the 'extra' sites by linking them with the imposed partitioning cells. If the cells and the 'extra' sites are combined effectively we know from the outset that no new site can have nearest neighbours in more than the nearest four cells. Thus we can improve the performance of the algorithm by increasing the number of cells, this leads to no increase in the execution time but does increase the memory requirement. Because for these diagrams the average number of neighbours is fixed at six, and only neighbouring triangles are affected by the removal of a site, we know that on average only six triangles are involved in each site removal, of which there are $\mathcal{M}$, so that this stage is $\mathcal{O}(\mathcal{M}) \sim \mathcal{O}(\mathcal{N})$. Duality implies, as above, that constructing the Voronoi diagram from the Delaunay triangulation is $\mathcal{O}(\mathcal{N})$. Thus the entire algorithm is $\mathcal{O}(\mathcal{N})$.

We show how the IDA works by running through an example of constructing the Voronoi diagram of a set of sites lying on a torus. The 'real' sites are denoted by • and the 'extra' sites are denoted by ∘. The the uppermost row of sites are identical to the lowest row, and the rightmost column to the leftmost column. In Fig. A.3 are shown the full set of sites.

We know the triangulation of the 'extra' sites from the symmetry of their arrangement. Again the edges and sites on the extremities of the area are identified with those on the opposite extremity. The circumcircles of the triangles have also been shown, in Fig. A.4.

Now, in Fig. A.5, we focus on the area around sites 1 and 6. We now need to insert the

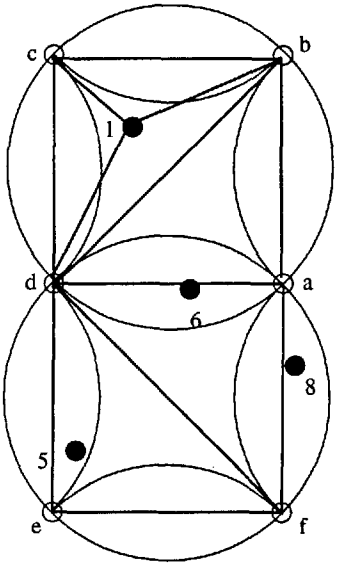

Figure A.7: An incorrect re-triangulation

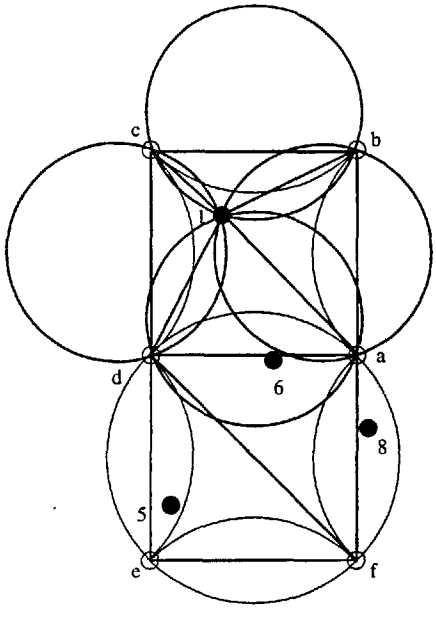

Figure A.8: Insertion of site 1

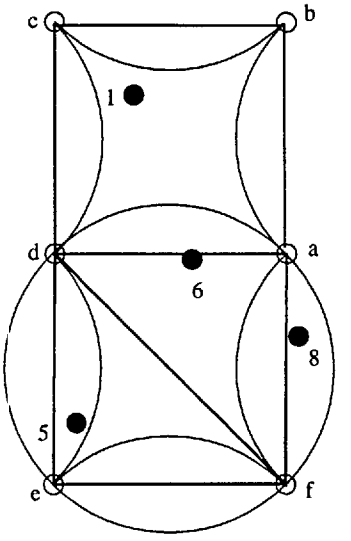

Figure A.6: Remove triangles *abc* and *acd*

'real' sites into the triangulation. We start by inserting site 1. We note that site 1 only falls in two circumcircles, those belonging to triangles *abc* and *acd* (which are not distinct on the diagram). Thus these are the only triangles which no longer satisfy the Delaunay criterion. So we start by removing these triangles, see Fig. A.6, which implies the removal of any edges lying between two of these triangles.

Next we must re-triangulate the 'hole' left in Fig. A.6, which is in fact very easy. We know that as the only triangles that site 1 affected have been removed, no other triangles can be changed. The sites surrounding site 1 are already connected together along the perimeter of the 'hole', ie *abcd*. The only way in which we can triangulate the 'hole' is by linking site 1 to each of $\{a, b, c, d\}$ by an edge. Otherwise some two sites lying on the perimeter, but not being neighbours, would have to be connected, as in Fig. A.7. However this must violate the Delaunay criterion for the following reasons

- If the edge connecting these two had been part of the previous triangulation, Fig. A.5, then its circumcircle would contain site 1, thus it can no longer be part of the Delaunay triangulation.

- On the other hand if the triangle was not part of the previous triangulation then that implies that its circumcircle must have contained some other site in the set of sites, so it cannot be part of the triangulation.

This reasoning is better demonstrated by the insertion of site 6, in Figs. A.8, A.9 & A.10.

We thus conclude that site 1 must be joined to all the sites on the perimeter of the 'hole', as in Fig. A.8, and likewise with site 6 in Fig. A.10.

Finally, when we have inserted all the 'real' sites and correctly triangulated them, we have

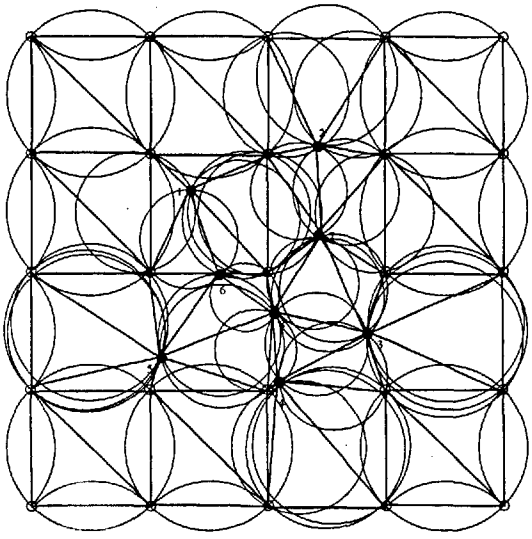

Figure A.11: All inserted

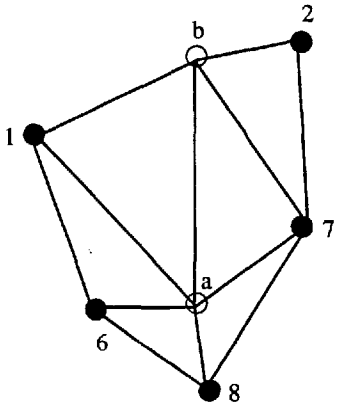

Figure A.12: Environs of extra site a

the situation in Fig. A.11. The next task is to remove the 'extra' sites, one by one, whilst keeping the triangulation correct.

Again this task is quite easily performed because of the Delaunay criterion. For instance we consider site a. The triangles which have site a as a vertex form a polygon around a. Only these triangles can be affected by the removal of a, as before and after the removal of a no other triangles have any change in the contents of their circumcircles. Triangles $ab1$, $a16$, $a68$, $a87$ and $a7b$ must be removed, leaving a 'hole', see Fig. A.13, which we must re-triangulate.

We re-triangulate the 'hole' by making a list of the edges and sites on the perimeter; we take an edge off the head of the list and then go through the sites in the list until we find one which makes a Delaunay triangle with this edge. This appears to be the most efficient technique. The technique is shown in Figs. A.13 & A.14.

When we have completed the removal of the 'extra' sites we have obtained the complete

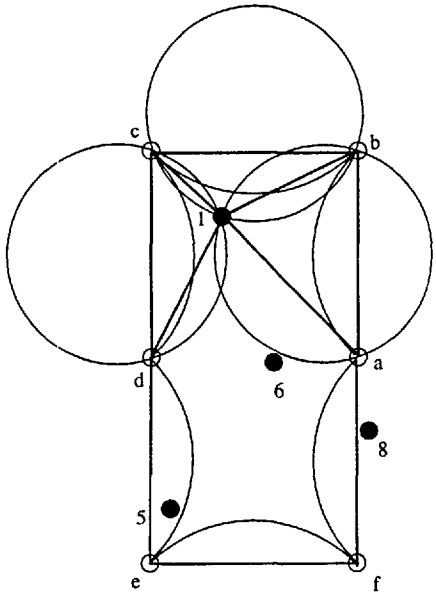

Figure A.9: Remove triangles $a1d$, adf and def

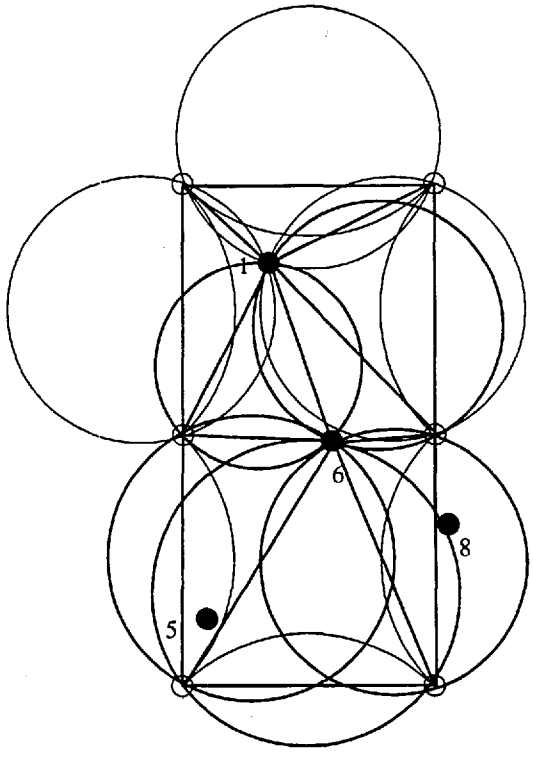

Figure A.10: Insertion of site 6

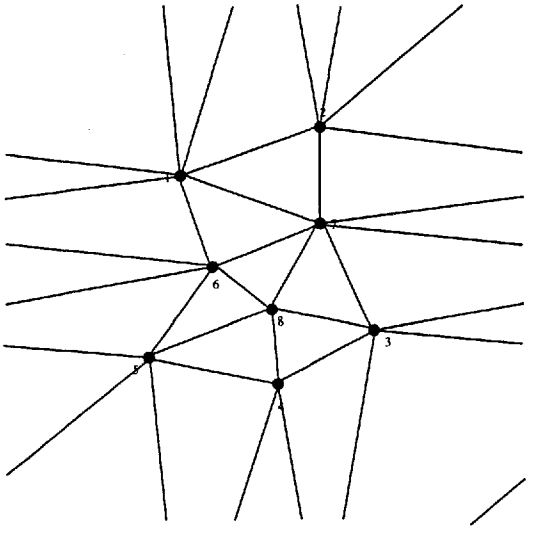

Figure A.15: Finished Delaunay triangulation on torus

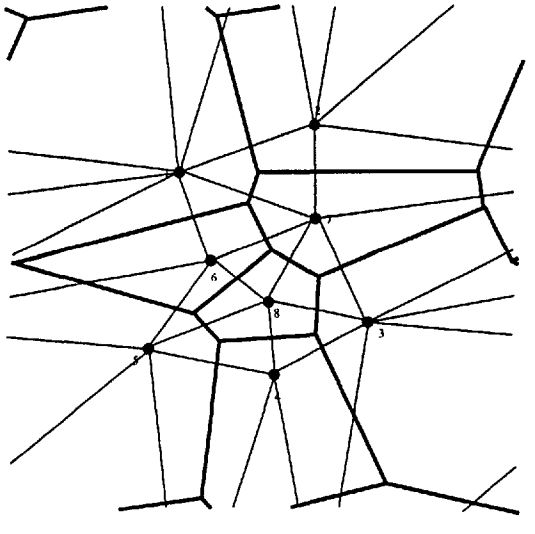

Figure A.16: Voronoi diagram on torus — from duality

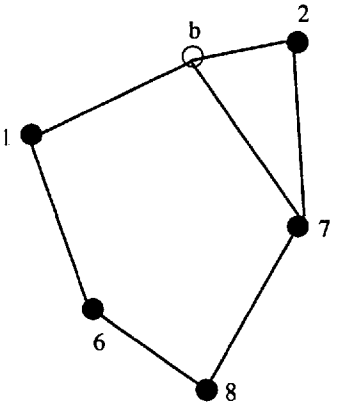

Figure A.13: Deletion of extra site a

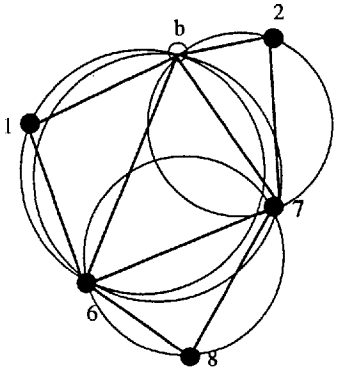

Figure A.14: Triangulation of 'hole'

Delaunay triangulation of the 'real' sites, as shown in Fig. A.15.

The final step of the IDA is to obtain the Voronoi diagram from the Delaunay triangulation by using the duality of the two. The relation is straightforward. Every vertex of the triangulation corresponds to a cell of the Voronòi diagram, every triangle corresponds to a vertex of the Voronoi diagram, which is positioned at the circumcenter of the triangle, and every edge of the triangulation corresponds to a perpendicular edge of the Voronoi diagram. The final diagram is shown in Fig. A.16

A.4 Generalisation to n-manifolds

This algorithm can be easily generalised to n-manifolds, and specifically to the three-dimensional torus which is of interest in modelling three-dimensional foams. The algorithm generalises directly; the triangles become n-simplices and the circumcircles become n-circumspheres. The method for determining circumcentres in higher dimensional manifolds is given in Ref. [145].

Now we know that

$$\frac{\vec{r_1} \times \vec{r_2}}{\vec{r_1} \cdot \vec{r_2}} = -\frac{\vec{r_1} \times \vec{r_3}}{\vec{r_1} \cdot \vec{r_3}} = \sqrt{3}\vec{e_z} \tag{B.3}$$

where $\vec{e_z}$ is the unit vector along the z-axis, so that the three films vectors meet at $2\pi/3$ radians, then by inserting Eq.s B.1 and B.2, we obtain

$$x^2 + y^2 + B_3 x + C_3 y = 0 \tag{B.4}$$

and

$$x^2 + y^2 + B_2 x + C_2 y = 0 \tag{B.5}$$

where we have

$$B_3 = \frac{1}{\sqrt{3}} b_{3y} - b_{3x} , \tag{B.6}$$

$$B_2 = -b_{2x} - \frac{1}{\sqrt{3}} b_{2y} , \tag{B.7}$$

$$C_3 = -\frac{1}{\sqrt{3}} b_{3x} - b_{3y} , \text{ and} \tag{B.8}$$

$$C_2 = \frac{1}{\sqrt{3}} b_{2x} - b_{2y} . \tag{B.9}$$

$$\tag{B.10}$$

These equations have several solutions.

1. The degenerate solution $\vec{X} = \vec{0}$, which is not physically consistent.

2. Solutions where the vertex lies outside the triangular cell, these solutions are also physically meaningless.

3. Solutions where the vertex lies inside the trianglular cell. These are the solutions we are interested in and represent normal Plateau borders. Then $\vec{X}$ has components

$$x = -\frac{B_2(C_2 - C_3)^2 + C_2(B_2 - B_3)(C_2 - C_3)}{(B_2 - B_3)^2 + (C_2 - C_3)^2} \tag{B.11}$$

$$y = -\frac{C_2(B_2 - B_3)^2 + B_2(C_2 - C_3)(B_2 - B_3)}{(C_2 - C_3)^2 + (B_2 - B_3)^2} \tag{B.12}$$

$$\tag{B.13}$$

4. Solutions where the vertex coincides with one of the film mid-points (that is a corner of the triangular cell). These represent the limits of the class 3 solutions, and the onset of a T1 event. Thus these solutions are where

$$\vec{X} = \vec{0} \tag{B.14}$$

$$\vec{X} = \vec{b_3} \tag{B.15}$$

$$\vec{X} = \vec{b_2} \tag{B.16}$$

At this point we need to invoke the T1 event rules which are developed below, see Section B.2.

Appendix B

2D VEM details

B.1 Equilibrium Vertex Configuration

In this section we will derive the formulae for the coordinates giving the position of a vertex (Plateau border) such that three films meet there at common angles of $2\pi/3$ radians, given the positions of the mid-points of the films.

In Fig. B.1 we have the initial vectors b_2 and b_3 giving the positions of the mid-points A_2 and A_3 respectively, or alternatively the vectors $\vec{r_1}$, $\vec{r_2}$ and $\vec{r_3}$ which give the positions of A_1, A_2 and A_3 from some point. We use $\vec{X}$ to denote the position of the vertex, with coordinates x and y.

First we have

$$\vec{b_2} = \vec{r_1} + \vec{r_2} \tag{B.1}$$

and

$$\vec{b_3} = \vec{r_1} + \vec{r_3} \tag{B.2}$$

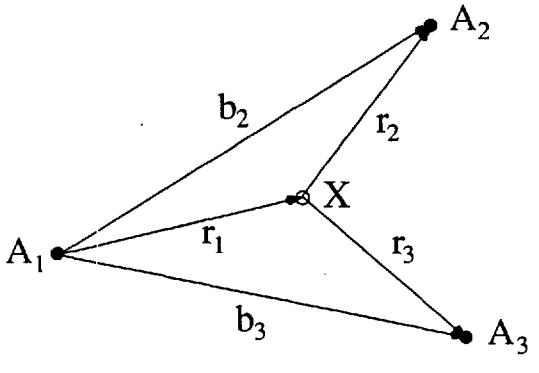

Figure B.1: Vertex and cell

The calculation proceeds by assuming that the elastic limit is not exceeded, so that the Reynolds number for film fluid flow is vanishingly small. Further more the motion is assumed slow enough that quasistatic equations can be used. Finally the creation of film area is assumed to take place only in the Plateau border. With these assumptions Princen and Schwartz were able to obtain expressions for the dissipation of energy in stretching and contracting films. The resulting rate of dissipation of energy is

$$\Phi = \frac{6\mu U^2 I}{(3\mathrm{Ca})^{1/3}} \tag{B.17}$$

where I is a numerical constant which takes two values, one (I_e) for film extension and one (I_c) for contraction,

$$I_e = 1.2215 \tag{B.18}$$

$$I_c = 1.1866 \tag{B.19}$$

and Ca is the capillary number

$$\mathrm{Ca} = \frac{\mu|U|}{\sigma} \tag{B.20}$$

We can now use this expression to obtain a formula for the force acting on a vertex due to a stretching/contracting film incident to it. We have

$$FU = \Phi \tag{B.21}$$

so that

$$F = \frac{6\mu U I(U)}{(3\mathrm{Ca})^{1/3}} \tag{B.22}$$

where

$$I(U) = I_e\Theta(U) - I_c\Theta(-U) \tag{B.23}$$

so that the force opposes the motion and the constant I is correct. For use in our model each vertex is affected by three half-films. The velocity U of vertex movement is given by the rate of change of half-film length, $U = \dot{L}$.

Thus the final expression for the extra force due to viscous flow in the films is

$$F = \frac{6\mu\dot{L}I(\dot{L})}{(3\mathrm{Ca})^{1/3}} = 6\mu\dot{L}I(\dot{L})\left(\frac{\sigma}{3\mu|\dot{L}|}\right)^{1/3} \tag{B.24}$$

The rules for the equilibrium configuration of vertices when there are viscous forces acting in the films are identical to those above, except that the forces are given by Eq. B.25.

$$F = \sigma + 6\mu\dot{L}I(\dot{L})\left(\frac{\sigma}{3\mu|\dot{L}|}\right)^{1/3} \tag{B.25}$$

The three forces acting on a vertex are not necessarily all equal so that the forces balance at angles other than $2\pi/3$ radians. The balanced vertex is shown in Fig. B.2; the angles are

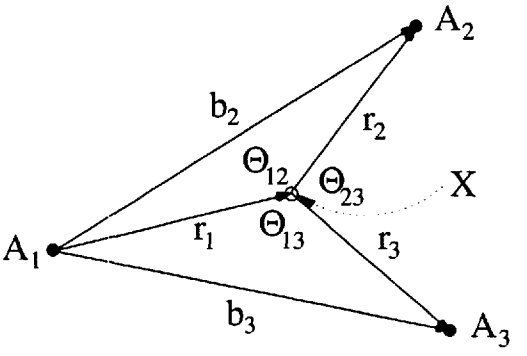

Figure B.2: Vertex and cell

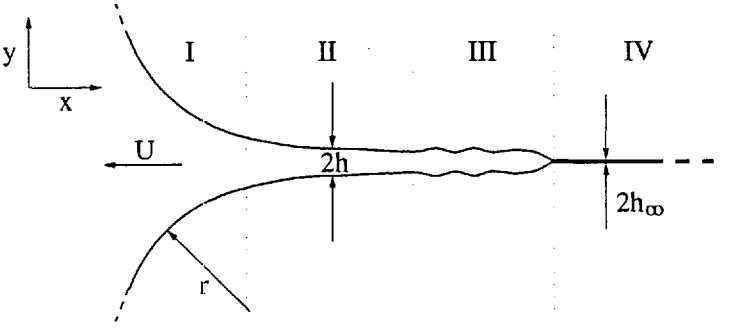

Figure B.3: Viscous flow geometry

B.1.1 Equilibrium Configuration with Viscous Forces

Two separate methods have been used in the literature for calculating the viscous forces acting in thin films as they stretch or shrink. Khan [57] uses a simple estimate based on the idea that the volume of fluid in each film is fixed so that the fluid in the film undergoes extensional shear as the film changes length. This gives a simple flow pattern and enables a calculation of the resulting viscous force, but it does not give particularly realistic behaviour.

The approach of Princen et al. [86, 93] is based on a much longer and more careful examination of the dynamics of the film, but pays dividends. We will not go into details here, the work is well explained in [86]. The geometry of a stretching or shrinking film is shown in Fig. B.3; it consists of four regions to a good approximation. Region I is the Plateau border which maintains a constant shape during film deformation, it is moving with some velocity U. Region II is termed the transitional area, and is the one where most viscous forces appear. The shape of the film and the flows in region II are determined by the film deformation. Region III is termed the laid-down film area; here the shape of the film is determined mainly by the history of the film, and there is little flow, we assume that the flow doesn't interact with the deformational flow to dissipate energy here. Region IV is the thin film area where the film width is determined by its equilibrium properties, this region is unaffected by the film deformation.

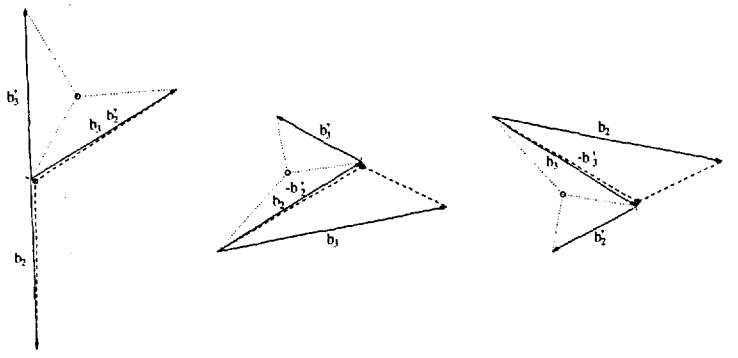

Figure B.4: Rules for T1 events

B.2 T1 rules

The sets of equations in the above sections tell us how a vertex evolves under the continuous part of the vertex map. However at some stage the vertex may undergo a T1 event, and at the instant that the T1 occurs these equations break down. To continue we need to redefine b_2 and b_3 and then use the equations.

We know that a T1 replaces an infinitesimal film with a finite film perpendicular to it, which makes the redefinitions needed quite evident. The rules we apply are very similar to those of Kraynik and Hansen [81, 84] and are shown in Fig. B.4. The actual replacements are

$$\vec{X} = \vec{0} \rightarrow \begin{cases} \vec{b_1} = \vec{b_2} \\ \vec{b_2} = -\vec{b_1} \end{cases} \tag{B.43}$$

$$\vec{X} = \vec{b_1} \rightarrow \begin{cases} \vec{b_1} = \vec{b_1} \\ \vec{b_2} = \vec{b_2} - \vec{b_1} \end{cases} \tag{B.44}$$

$$\vec{X} = \vec{b_2} \rightarrow \begin{cases} \vec{b_1} = \vec{b_1} - \vec{b_2} \\ \vec{b_2} = -\vec{b_2} \end{cases} \tag{B.45}$$

B.3 Bulk Stress Tensor Calculations

The variables in which we are interested are the osmotic pressure, the bulk stress tensor and the viscosity of the disordered foam. The method used to calculate the osmotic pressure is outlined in Chapter 6. Here we outline the means used to calculate the stress tensor and the viscosity.

For calculations involving different deformations different aspects of the stress tensor are of interest. For simple shear work we are interested primarily in the shear stress τ_{xy}, and thus in the corresponding viscosity $\mu = \tau_{xy}/\dot{\gamma}$. When dealing with extensional shear we are interested in the first and second normal stress differences, defined as $N_1 = \tau_{xx} - \tau_{yy}$ and $N_2 = \tau_{xx} - \tau_{zz}$ (where the xy-plane is the shear plane), as the shear stress τ_{xy} must be zero. We are also

determined by the forces in the films in the following way. The forces pulling the vertex along each film vector are F_1,F_2 and F_3. Balancing these forces we have

$$\cos(\pi - \theta_{12}) = \sin(\theta_{12}) = \frac{F_1^2 + F_2^2 - F_3^2}{2F_1F_2} \tag{B.26}$$

$$\cos(\pi - \theta_{13}) = \sin(\theta_{13}) = \frac{F_1^2 + F_3^2 - F_2^2}{2F_1F_3} \tag{B.27}$$

so that

$$\tan(\theta_{12}) = \frac{F_1^2 + F_2^2 - F_3^2}{\sqrt{(F_2^2 - (F_1 - F_3)^2)\,((F_1 + F_3)^2 - F_2^2)}} \tag{B.28}$$

$$\tan(\theta_{13}) = \frac{F_1^2 + F_3^2 - F_2^2}{\sqrt{(F_3^2 - (F_1 - F_2)^2)\,((F_1 + F_2)^2 - F_3^2)}} \tag{B.29}$$

which we shall use below.

Now we have a similar problem to that above, only with unequal angles between films, given by Eq. B.28. Again we use the film midpoint A_1 as the coordinate origin, so that we have the vectors representing the vertex X, and the films r_1, r_2 and r_3.

$$\vec{X} = -\vec{r_1} \tag{B.30}$$

$$\vec{r_2} = \vec{b_2} - \vec{X} \tag{B.31}$$

$$\vec{r_3} = \vec{b_3} - \vec{X} \tag{B.32}$$

Now we introduce the angular constraints,

$$\frac{\vec{r_1} \wedge \vec{r_2}}{\vec{r_1} \cdot \vec{r_2}} = \tan(\theta_{12}) = \kappa_{12} \tag{B.33}$$

$$\frac{\vec{r_1} \wedge \vec{r_3}}{\vec{r_1} \cdot \vec{r_3}} = \tan(\theta_{13}) = \kappa_{13} \tag{B.34}$$

and solve the resulting equations,

$$x^2 + y^2 + B_1x + C_1y = 0 \tag{B.35}$$

$$x^2 + y^2 + B_2x + C_2y = 0 \tag{B.36}$$

to obtain,

$$B_2 = \frac{\vec{b_{2y}}}{\kappa_{12}} - \vec{b_{2x}} \tag{B.37}$$

$$B_3 = \frac{\vec{b_{3y}}}{\kappa_{13}} - \vec{b_{3x}} \tag{B.38}$$

$$C_2 = \frac{\vec{b_{2x}}}{\kappa_{12}} - \vec{b_{2y}} \tag{B.39}$$

$$C_3 = \frac{\vec{b_{3x}}}{\kappa_{13}} - \vec{b_{3y}} \tag{B.40}$$

Now finally we have,

$$x = -\frac{C_2(B_2 - B_3)^2 + B_2(B_2 - B_3)(C_2 - C_3)}{(B_2 - B_3)^2 + (C_2 - C_3)^2} \tag{B.41}$$

$$y = -\frac{B_2(C_2 - C_3)^2 + C_2(B_2 - B_3)(C_2 - C_3)}{(B_2 - B_3)^2 + (C_2 - C_3)^2} \tag{B.42}$$

Using these expressions we can calculate the bulk stress tensor as an expectation over our distributions, and arrive at concrete predictions. These expressions are used in Chapters 4 and 6.

interested in the planar extensional viscosity $\mu_e = (\tau_{xx} - \tau_{yy})/\dot{\epsilon}$ where ϵ is the Hencky strain, see Section 2.7.1. Thus in order to obtain all parameters of interest we require only the bulk stress tensor.

The bulk stress tensor $\boldsymbol{\tau}$ of a foam sample is given [146, 147] by

$$\boldsymbol{\tau} = \frac{1}{V}\int_V \hat{\boldsymbol{\tau}}\, dv \tag{B.46}$$

where $\hat{\boldsymbol{\tau}}$ is the local stress tensor, and V is the volume of the sample. In our models we make use of a distribution $P(x)$ over the vertex configuration space $\mathcal{V}$, therefore we obtain $\boldsymbol{\tau}$ as an expectation value over this distribution. This corresponds in the ensemble picture to summing over all vertices in the ensemble, and dividing by the sample volume. So

$$\boldsymbol{\tau} = \frac{1}{U}\int_{\mathcal{V}}\int_{V(x)} P(x)\hat{\boldsymbol{\tau}}_x\, dx\, dv \tag{B.47}$$

$$= \int_{\mathcal{V}} P(x)\left[\int_{\text{fluid}(x)} (p_l\boldsymbol{\delta} - \mu\dot{\boldsymbol{\gamma}})\, dv + \int_{\text{film}(x)} \hat{\boldsymbol{\tau}}_x\, dv + \int_{\text{gas}(x)} p_g\boldsymbol{\delta}\right] dv \tag{B.48}$$

where $\hat{\boldsymbol{\tau}}_x$ is the local stress tensor for a particular vertex configuration x, $\dot{\boldsymbol{\gamma}}_x$ is the local rate of strain tensor, U is the average cell area ($U = \int_{\mathcal{V}} P(x)V(x)dx$) and $V(x)$ is the volume associated with the vertex - divided into film, fluid and gas parts. The gas contribution is simple, arising only from the pressure (this is a good approximation in emulsions also).

The film contribution is further split up into the contributions of the three films which meet at the vertex, so

$$\int_{\text{film}(x)} \hat{\boldsymbol{\tau}}_x\, dv = \sum_i \int_{\text{film}(x,i)} \hat{\boldsymbol{\tau}}_{xi}\, dv \tag{B.49}$$

where i ranges from 1 to 3. Each film gives a contribution

$$\int_{\text{film}(x,i)} \hat{\boldsymbol{\tau}}_{xi}\, dv = -\int_{\text{film}(x,i)} \sigma(\boldsymbol{\delta} - \boldsymbol{nn}_i)\, dS \tag{B.50}$$

$$= -\int_{\text{film}(x,i)} \sigma\boldsymbol{tt}_i\, dS \tag{B.51}$$

where $\boldsymbol{nn}_i$ & $\boldsymbol{tt}_i$ are dyadics which are normal and tangential to the film, and dS is an element of the film surface area.

The first liquid term arises from the pressure in this phase. The second liquid contribution splits up into 3 separate contributions,

$$\int_{\text{fluid}(x)} \mu\dot{\boldsymbol{\gamma}}_x\, dv = \mu\sum_i \int_{\text{fluid}(x,i)} \dot{\boldsymbol{\gamma}}_{xi}\, dv \tag{B.52}$$

where i ranges from 1 to 3. Each fluid region gives a contribution

$$\int_{\text{fluid}(x,i)} \dot{\boldsymbol{\gamma}}_{xi}\, dv = -\int_{\text{fluid}(x,i)} 6\mu\dot{L}I(\dot{L})\left(\frac{\sigma}{3\mu|\dot{L}|}\right)^{1/3} \boldsymbol{tt}_i\, dS \tag{B.53}$$

where we have used the expression for the viscous force in the fluid region derived in Section B.1.1.

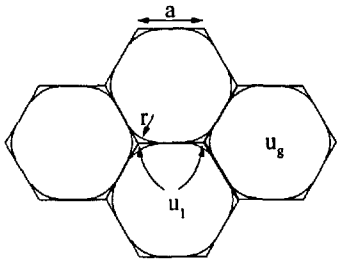

Figure C.2: Regular hexagonal foam as fluid fraction increases

is $V_g = \mathcal{N} u_g$ where u_g is the volume of one gas cell, so that the total volume of the cell and surrounds is $u = u_l + u_g$. The total length of all films in the foam is $L = 3\mathcal{N} a_0 = \mathcal{N} l$ initially.

Now we begin to admit fluid into the foam, as in Fig. C.2. We can see that the fluid volume u_l is the area of the two triangles in the corner minus the area of the circular wedge, see Fig. C.3.

$$u_l = 2r^2 \left(\sqrt{3} - \pi/2\right) \tag{C.2}$$

so that the total volume of the cell and surrounds is

$$u = H(a) = u_g + 2r^2 \left(\sqrt{3} - \pi/2\right) \tag{C.3}$$

The total length of film is the perimeter length of the hexagon minus the corner lengths plus the arc lengths, giving

$$l = 6a + 4r \left(\pi/2 - \sqrt{3}\right) \tag{C.4}$$

Φ is given by the ratio of gas volume to total volume, which is the ratio of the initial dry hexagon's area to that of the new hexagon.

$$\Phi = \frac{H(a_0)}{H(a)} = \left(\frac{a_0}{a}\right)^2 \tag{C.5}$$

So now we have that, with u_g fixed and thus $du_g = 0$,

$$du = 4r \left(\sqrt{3} - \pi/2\right) dr \tag{C.6}$$

$$dH(a) = 3\sqrt{3} a \, da \tag{C.7}$$

$$\tag{C.8}$$

and

$$dl = 6\frac{4}{3\sqrt{3}} \left(\sqrt{3} - \pi/2\right) \frac{r}{a} dr - 4 \left(\sqrt{3} - \pi/2\right) dr \tag{C.9}$$

Finally we obtain Φ as the ratio of σdl and du.

$$\Pi = -\sigma \left(\frac{\partial L}{\partial A}\right)_{A_g} \tag{C.10}$$

$$= -\sigma \left(\frac{\partial l}{\partial u}\right)_{u_g} \tag{C.11}$$

$$= -\frac{\sigma}{a} \left[\frac{2}{\sqrt{3}} - \frac{a}{r}\right] \tag{C.12}$$

Appendix C

3 Equal Films Osmotic Pressure Calculation

We start with a perfectly ordered hexagonal dry foam as shown in Fig. C.1. The initial foam has all films with the same length a_0. The foam is entirely dry so $\Phi = 0$, and it is formed of $\mathcal{N}$ bubbles. Now we will expand the foam, allowing it to suck up fluid; this fluid will accumulate at the Plateau borders as discussed in Chapter 2. As we do this gently there is nothing to break the symmetry of the foam and we expect it will maintain its perfect order.

First we define a function $H(a)$ which tells us the area of a regular hexagon formed by six sides of length a.

$$H(a) = \frac{3\sqrt{3}}{2}a^2 \tag{C.1}$$

We can split the foam up into constituent cells and consider only one cell, all the others being exactly the same. Each cell is attached to three films and two vertices, as each cell has six films adjacent to it and each film touches two cells, and again each cell has six vertices adjacent to it and each vertex touches three cells. Thus the total liquid volume of the foam $V_l = \mathcal{N}u_l$ where u_l is the liquid content of two vertices, and the total gas volume of the foam

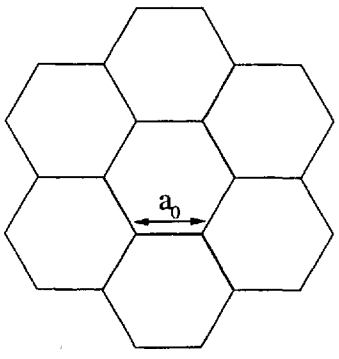

Figure C.1: Regular hexagonal dry foam

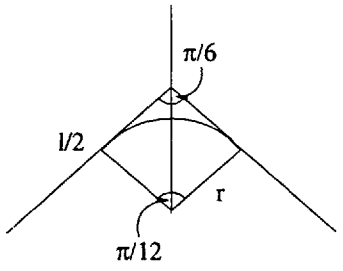

Figure C.3: Cell corner containing fluid

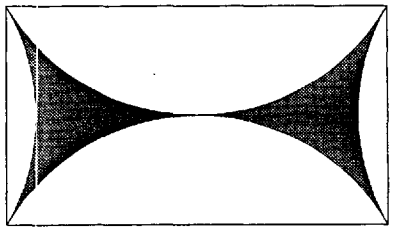

Figure C.4: Border coalescence in hexagonal ordered foam

Now we can use

$$\Phi = 1 - \frac{u_l}{u} \tag{C.13}$$

$$= 1 - 2\left(\frac{r}{a}\right)^2 \left(\sqrt{3} - \pi/2\right) \frac{2}{3\sqrt{3}} \tag{C.14}$$

$$\tag{C.15}$$

so that

$$\frac{r}{a} = \left(\frac{\sqrt{3}}{2}\right) \left(\frac{1-\Phi}{1-\pi/2\sqrt{3}}\right)^{1/2} \tag{C.16}$$

$$= \left(\frac{\sqrt{3}}{2}\right) \left(\frac{1-\Phi}{1-\Phi_c^h}\right)^{1/2} \tag{C.17}$$

and Eq. C.5 so that

$$a = \frac{a_0}{\Phi^{1/2}} \tag{C.18}$$

$$= \frac{2R}{\sqrt{3}} \left(\frac{\Phi_c^h}{\Phi}\right)^{1/2} \tag{C.19}$$

$$\tag{C.20}$$

in order to rewrite this in the form of Princen's result

$$\Pi = \frac{\sigma}{R} \left(\frac{\Phi}{\Phi_c^h}\right)^{1/2} \left[\left(\frac{1-\Phi_c^h}{1-\Phi}\right)^{1/2} - 1\right] \tag{C.21}$$

and

$$dl = 2(1+\beta+\gamma)a_0\frac{\Phi^{1/2}}{u_g}du - \frac{du}{r} \tag{D.4}$$

Also we have that

$$\Phi = 1 - \frac{2Qr^2\Phi}{u_g} \tag{D.5}$$

so that

$$r = \left(\frac{u_g(1-\Phi)}{2Q\Phi}\right)^{1/2} \tag{D.6}$$

This results in

$$\Pi = -\sigma\left(2(1+\beta+\gamma)a_0\frac{\Phi^{1/2}}{u_g} - \left(\frac{2Q\Phi}{u_g(1-\Phi)}\right)^{\frac{1}{2}}\right) \tag{D.7}$$

which we can tidy up using Φ_c (see Section 6.2.2), Q and u_g to obtain

$$\Pi = -\frac{\sigma}{R}\frac{2}{\beta+\beta\gamma+\gamma}\left(\frac{\beta+\beta\gamma+\gamma-\sqrt{3}Q}{2\pi\sqrt{3}}\right)\left(\frac{\Phi}{\Phi_c}\right)^{\frac{1}{2}}\left[\beta+\gamma+1-(\beta+\beta\gamma+\gamma)\left(\frac{1-\Phi_c}{1-\Phi}\right)^{\frac{1}{2}}\right] \tag{D.8}$$

D.2 Phase II

We use a similar technique to that used in Chapter 6, finding the equations for the case with a box-cell of specific size, $a_0 = 1$, and then scaling up. We have

$$b\sin\theta = \frac{\beta\sqrt{3}}{2} \quad \Rightarrow \quad b = \frac{\beta\sqrt{3}}{2\sin\theta} \tag{D.9}$$

$$c\sin\theta = \frac{\gamma\sqrt{3}}{2} \quad \Rightarrow \quad c = \frac{\gamma\sqrt{3}}{2\sin\theta} \tag{D.10}$$

and also

$$2a + 2c\cos\theta = 2 + \gamma\sqrt{3} \tag{D.11}$$

so that

$$a = \frac{2+\gamma\sqrt{3}}{2} - \frac{\gamma\sqrt{3}}{2}\cot\theta \tag{D.12}$$

so that we also know

$$r = \frac{(2+\gamma\sqrt{3})\tan\theta - \gamma\sqrt{3}}{2(1+\tan(\theta/2)\tan\theta - 2\cos\theta)} \tag{D.13}$$

and as before

$$u_l = (8\sin\theta\cos\theta - \pi)r^2 \tag{D.14}$$

so that

$$\Phi = 1 - \frac{u_l}{2\sqrt{3}(\beta+\beta\gamma+\gamma)} \tag{D.15}$$

We also have

$$l = \frac{4\sqrt{3}}{2\sin\theta}(\gamma+\beta) + (\pi - 4\cot\theta)\frac{(2+\gamma\sqrt{3})\tan\theta - \gamma\sqrt{3}}{2(1+\tan(\theta/2)\tan\theta - 2\cos\theta)} \tag{D.16}$$

Appendix D

3 Film Osmotic Pressure Calculations

D.1 Phase I

We use a similar argument to that in Chapter 6. The basic geometry of the foam is unchanging, with only the film lengths and the radius of curvature varying. The liquid volume is given by

$$u_l = 2Qr^2 \tag{D.1}$$

with Q defined as before,

$$Q = \sqrt{3} - \frac{\pi}{2} \tag{D.2}$$

We know that the geometry of the foam is unchanged throughout this phase so that

$$da = -\frac{a_0}{2}\frac{\Phi^{1/2}}{u_g}du = \frac{db}{\beta} = \frac{dc}{\gamma} \tag{D.3}$$

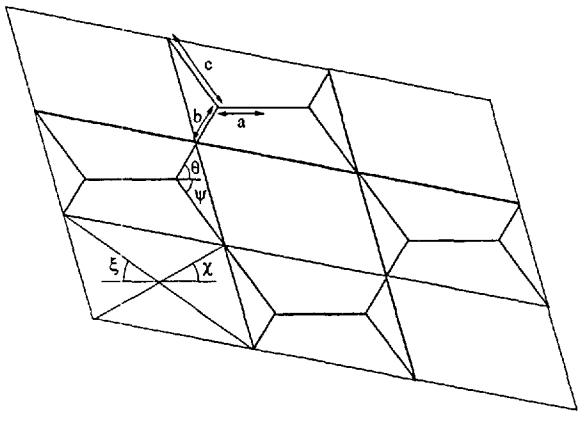

Figure D.1: Ordered foam with three film lengths

Now we scale up by $a_0/\Phi^{1/2}$, and using

$$\Pi = -\sigma\left(\frac{dl}{d\theta}\frac{d\theta}{du_l}\right) \tag{D.17}$$

we can obtain both Π and Φ as functions of θ in the range $\pi/3 > \theta > \theta_c$, where θ_c is as shown in Section 6.2.2.

D.3 Phase III

This region of the Π against Φ curve is derived in a slightly different way to that followed in Section 6.2.1. For $\Phi_s > \Phi > \Phi_d$ we know that, using a box-cell of a specific size, the radius of curvature is fixed, and the arcs form two semi-circles joined by the remaining thin film segment. Thus we only need to know the length f of this segment in order to obtain the gas volume u_g and the interface length l so that we can get Φ and Π. However we know that f ranges between f_s and $f_d = 0$, where

$$f_s = \frac{(\gamma-\beta)\sqrt{3}}{2+\beta}(1+\beta+\beta^2)^{1/2} \tag{D.18}$$

so that we can get $\Phi(f)$ and $\Pi(f)$ for $f_s > f > f_d$ and thus obtain $\Pi(\Phi)$ for $\Phi_s > \Phi > \Phi_d$.

So, again using a box-cell for $a_0 = 1$, we have a total periodic cell volume of

$$U = 2\sqrt{3}(\beta+\beta\gamma+\gamma) \tag{D.19}$$

and for some f

$$u_g = \pi(1+\beta+\beta^2) + 4f(1+\beta+\beta^2)^{1/2} \tag{D.20}$$

which leads us to

$$\Phi = \frac{\pi(1+\beta+\beta^2) + 4f(1+\beta+\beta^2)^{1/2}}{2\sqrt{3}(\beta+\beta\gamma+\gamma)} \tag{D.21}$$

Also we have the scaled-up interface length

$$l = \left(\frac{a_0}{\Phi^{1/2}}\right)\left(4f + 2\pi(1+\beta+\beta^2)^{1/2}\right) \tag{D.22}$$

Now using

$$\Pi = -\sigma\left(\frac{dl}{d\theta}\frac{d\theta}{du_l}\right) \tag{D.23}$$

and tidying up using Φ_d we obtain the same formula as for the two-distinct-film-length case

$$\Pi = \frac{\sigma}{2R}\left(\frac{\Phi}{\Phi_d}\right)^{\frac{1}{2}}(\Phi - \Phi_d) \tag{D.24}$$

[16] E C Zeeman. *Catastrophe Theory.* Academic Press, 1977.

[17] T Poston and I Stewart. *Catastrophe Theory and its Applications.* Pitman, 1978.

[18] P T Saunders. *An Introduction to Catastrophe Theory.* Cambridge, 1980.

[19] R Thom. *Morphogenesis.* Pitman, 1971.

[20] M O Magnasco. Correlations in cellular patterns. *Philosophical Magazine B*, 69(3):397–429, 1994.

[21] G Venkataraman and D Sahoo. Curved space and amorphous structures. Part I geometric models. *Contemporary Physics*, 26(6):579–615, 1985.

[22] G Venkataraman and D Sahoo. Curved space and amorphous structures. Part II gauge theories. *Contemporary Physics*, 27(1):3–35, 1986.

[23] M O Magnasco. Two-dimensional bubble rafts. *Philosophical Magazine B*, 65(5):895–920, 1992.

[24] C Nash and S Sen. *Topology.* Academic Press, 1980.

[25] H Flyvbjerg. Model for coarsening froths and foams. *Physical Review E*, 47(6):4037–4054, 1993.

[26] V E Fradkov, M O Magnasco, D Udler, and D Weaire. Determinism and stochasticity in ideal two-dimensional soap froths. *Philosophical Magazine Letters*, 67(3):203–211, 1993.

[27] D Aboav. Cell topology correlations in foams. *Metallography*, 13:43, 1980.

[28] F Bolton and D Weaire. The effects of Plateau borders in the two-dimensional soap froth. i decoration lemma and diffusion theorem. *Philosophical Magazine B*, 63(4):795–809, 1991.

[29] D Weaire and R Phelan. *Philosophical Magazine Letters*, 69:107, 1994.

[30] K Brakke. *Journal of Experimental Mathematics*, 1:141, 1992.

[31] A Kraynik. Aqueous foams. *Scientific American*, 254(5):58–67, May 1986.

[32] H V Atkinson. Theories of normal grain growth in pure single phase systems. *Acta Metallurgica*, 36(3):469–491, 1988.

[33] J A Glazier, M P Anderson, and G S Grest. Coarsening in the two-dimensional soap froth and the large-Q Potts model : a detailed comparison. *Philosophical Magazine B*, 62(6):615–645, 1990.

[34] Michael P Anderson, David J Srolovitz, Gary S Grest, and Paramdeep S Sahni. Computer simulation of grain growth—I kinetics. *Acta Metallurgica*, 32(5):783–791, 1984.

Bibliography

[1] P A Mulheran. On the statistical properties of the two-dimensional random Voronoi network. *Philosophical Magazine Letters*, 66(5):219–224, 1992.

[2] H M Princen. Highly concentrated emulsions : I cylindrical systems. *Journal of Colloid and Interface Science*, 71(1):55–66, 1979.

[3] W (Lord Kelvin) Thomson. *Philosophical Magazine*, 24:503, 1887.

[4] W (Lord Kelvin) Thomson. *Philosophical Magazine*, 26:414, 1888.

[5] D'Arcy Thompson. *On Growth and Form*. Cambridge, 1917.

[6] D Weaire and N Rivier. Soap, cells and statistics—random patterns in two dimensions. *Contemporary Physics*, 25(1):59–99, 1984.

[7] C S Smith. *Metal Interfaces*, page 65, 1952.

[8] J von Neumann. *Metal Interfaces*, page 108, 1952.

[9] N Rivier. Order and disorder in packings and froths. In D Bideau and A Hansen, editors, *Disorder and Granular Media*, pages 55–102. Elsevier Science, 1993.

[10] N Rivier. Continuous random networks, from graphs to glasses. *Advances in Physics*, 36(1):95–134, 1987.

[11] J A Glazier and F Graner. Simulation of the differential adhesion driven rearrangement of biological cells. *Physical Review E*, 47(3):2128–2153, 1992.

[12] R van de Weygaert. Fragmenting the universe III. *Philosophical Magazine Letters*.

[13] W Rossen. Foam flow in porous media. *Foams EuroConference — Arcachon, France*, 1996.

[14] J A Glazier and J Stavans. *Physical Review A*, 40:7398, 1989.

[15] D Lovett. *Demonstrating Science with Soap Films*. IOP Publishing, 1994.

[51] Paul A Mulheran. Mean field simulations of normal grain growth. *Acta Metallurgica et Materiala*, 40(8):1827–1833, 1992.

[52] Paul A Mulheran. The scaling state in two-dimensional grain growth. *Acta Metallurgica et Materiala*, 42(11):3589–3593, 1994.

[53] C W J Beenakker. Evolution of two-dimensional soap-film networks. *Physical Review Letters*, 57(19):2454–2457, 1986.

[54] M Marder. Soap-bubble growth. *Physical Review A*, 36(1):438–440, 1987.

[55] C W J Beenakker. Numerical simulation of a coarsening two-dimensional network. *Physical Review A*, 37(5):1697–1701, 1988.

[56] D Weaire and M A Fortes. Stress and strain in liquid and solid foams. *Advances in Physics*, 43(6):685–738, 1995.

[57] S A Khan and R C Armstrong. Rheology of foams : I theory for dry foams. *Journal of Non-Newtonian Fluid Mechanics*, 22:1–22, 1986.

[58] A David. PhD thesis, Stanford, 1968.

[59] A David and Jr Marsden. *Society of Petrochemical Engineers Journal*, 2544, 1969.

[60] M Mooney. *Journal of Rheology*, page 210, 1931.

[61] H G Wenzel and J P Brungraber. *ASCE : EM6*, page 153, 1967

[62] J T Patton, Jr Patton, M Kuntamukkula, and S Holbrook. *Polymer Preprints*, 22(1):396, 1981.

[63] H G Wenzel and J P Brungraber. *Journal of Materials*, 5(2):396, 1970.

[64] A H Boyer, R S Millhone, and R W Foote. Polymer preprints. *Society of Petrochemical Engineers Journal*, 3986, 1972.

[65] H M Princen. PhD thesis, University of Utrecht, 1965.

[66] A S Yoshimura and R K Prud'homme. Response of an elastic bingham fluid to oscillatory shear. *Rheologica Acta*, 26:428–436, 1987.

[67] A S Yoshimura, R K Prud'homme, H M Princen, and A D Kiss. A compa[illegible] of techniques for measuring yield stresses. *Journal of Rheology*, 31(8):699–710, 1987.

[68] B Derjaguin. *Kolloid-Z*, 64(1), 1933.

[69] D Stamenovic and T A Wilson. The shear modulus of liquid foam. *Journal of Applied Mechanics*, 51:229–231, 1984.

[35] J M Turner. Froth and foam modelling. *Internal Report*, 1994.

[36] D Weaire and J P Kermode. Computer simulation of a two-dimensional soap froth : I method and motivation. *Philosophical Magazine B*, 48(3):245–259, 1983.

[37] D Weaire and J P Kermode. Computer simulation of a two-dimensional soap froth : II analysis of results. *Philosophical Magazine B*, 50(3):379–395, 1984.

[38] D Weaire and J P Kermode. The evolution of the structure of a two-dimensional soap froth. *Philosophical Magazine B*, 47(3):L29–L31, 1983.

[39] J P Kermode and D Weaire. 2D-FROTH: a program for the investigation of 2-dimensional froths. *Computer Physics Communications*, 60:75–109, 1990.

[40] J Wejchert, D Weaire, and J P Kermode. Monte Carlo simulation of the evolution of a two-dimensional soap froth. *Philosophical Magazine B*, 53(1):15–24, 1986.

[41] T Herdtle and H Aref. Relaxation of fractal foam. *Philosophical Magazine Letters*, 64(5):335–340, 1991.

[42] T Herdtle and H Aref. Numerical experiments on two-dimensional foam. *Fluid Mechanics*, 241:233–260, 1992.

[43] K Kawasaki, T Nagai, and K Nakashima. Vertex models for two dimensional grain growth. *Philosophical Magazine B*, 60:399–421, 1989.

[44] K Nakashima, T Nagai, and K Kawasaki. Scaling behaviour of two dimensional domain growth: Computer simulation of vertex models. *Journal of Statistical Physics*, 57:759–787, 1989.

[45] V E Fradkov and D Udler. Two-dimensional normal grain growth : Topological aspects. *Advances in Physics*, 43(6):739–789, 1994.

[46] C S Smith. *Transactions of the American Institute of Mineral and Metallurgical Engineers*, 175:15, 1948.

[47] W W Mullins. Two-dimensional motion of idealized grain boundaries. *Journal of Applied Physics*, 27(8):900–904, 1956.

[48] M Hillert. *Acta Metallurgica*, 13:227, 1965.

[49] Paul A Mulheran. The scaling theory of normal grain growth : Beyond the mean-field approximation. *Philosophical Magazine Letters*, 65(3):141–145, 1992.

[50] N P Louat. *Acta Metallurgica*, 22:721, 1974.

[87] D A Reinelt and A M Kraynik. On the shearing flow of foams and concentrated emulsions. *Journal of Fluid Mechanics*, 215:431–455, 1990.

[88] D Weaire and T-L Fu. The mechanical behaviour of foams and emulsions. *Journal of Rheology*, 32(3):271–283, 1988.

[89] D Weaire, T-L Fu, and J P Kermode. On the shear elastic constant of a two-dimensional froth. *Philosophical Magazine B*, 54(2):L39–L43, 1986.

[90] D Weaire, F Bolton, T Herdtle, and H Aref. The effect of strain upon the topology of a soap froth. *Philosophical Magazine Letters*, 66(6):293–299, 1992.

[91] T Herdtle. PhD thesis, University of California, San Diego, 1991.

[92] K Kawasaki, T Okuzono, and T Nagai. Mechanical and flow behaviour of two-dimensional foams. *Journal of the Mechanical Behaviour of Materials*, 4(1):51–60, 1992.

[93] T Okuzono and K Kawasaki. Rheology of random foams. *Journal of Rheology*, 37(4):571–586, 1993.

[94] K Kawasaki and T Okuzono. Intermittent flow behaviour of random foams: A computer experiment on foam rheology. *Physical Review E*, 51(2):1246–1253, 1995.

[95] P Bak, C Tang, and K Wiesenfeld. Self-organized criticality. *Physical Review A*, 38(1):364–373, 1988.

[96] C Tang and P Bak. Sandpile dynamics. *Physical Review Letters*, 60:2347–2351, 1988.

[97] Per Bak and Henrik Flyvbjerg. Self-organization of magnetic domain patterns. *Physica A*, 185:3–10, 1992.

[98] Per Bak and Henrik Flyvbjerg. Self-organization of cellular magnetic-domain patterns. *Physical Review A*, 45(4):2192–2200, 1992.

[99] X F Yuan and S F Edwards. Flow behaviour of two-dimensional random foams. *Journal of Non-Newtonian Fluid Mechanics*, 60:335–348, 1995.

[100] D J Durian. Foam mechanics at the bubble scale. *Physical Review Letters*, 75(26):4780–4783, 1995.

[101] S Hutzler, D Weaire, and F Bolton. The effects of Plateau borders in the 2-dimensional soap froth. iii further results. *Philosophical Magazine B*, 71(3):277–289, 1995.

[102] F Bolton and D Weaire. Rigidity loss transition in a disordered 2d froth. *Physical Review Letters*, 65(27):3449–3451, 1990.

[70] A M Kraynik and D A Reinelt.

[71] E W Billington and A Tate. *The Physics of Deformation and Flow.* McGraw Hill, 1981.

[72] K D Pithia and S F Edwards. Rheology of liquid foams. *Physica A*, 205:565–576, 1994.

[73] H M Princen. Rheology of foams and highly concentrated emulsions. *Journal of Colloid and Interface Science*, 91(1):160–175, 1983.

[74] H M Princen. *Journal of Colloid and Interface Science*, 20:156, 1965.

[75] H M Princen, M P Aronson, and J C Moser. Highly concentrated emulsions : II real systems; the effect of film thickness and contact angle on the volume fraction in creamed emulsions. *Journal of Colloid and Interface Science*, 75(1):246–270, 1980.

[76] S A Khan. *The Rheology of Large Gas Fraction Liquid Foams.* PhD thesis, Massachusetts Institute of Technology, 1985.

[77] M P Aronson and H M Princen. Contact angles associated with thin liquid films in emulsions. *Nature*, 286:370–372, 1980.

[78] R K Prud'homme. Rheology of ordered foam. *53rd Annual Society of Rheology Meeting — Louisville, KY*, 1981.

[79] D Weaire. A note on the elastic behaviour of ordered hexagonal froth. *Philosophical Magazine Letters*, 60(1):27–30, 1989.

[80] L Schiff. *Theory of Tensors.* Springer Verlag, 1952.

[81] A M Kraynik and M G Hansen. Foam and emulsion rheology : A quasistatic model for large deformations of spatially periodic cells. *Journal of Rheology*, 30(3):409–439, 1986.

[82] A M Kraynik and D A Reinelt. Extensional motions of spatially periodic lattices. *International Journal of Multiphase Flow*, 30(3):409–439, 1986.

[83] S A Khan and R C Armstrong. Rheology of foams : II effects of polydispersity and liquid viscosity for foams having gas fraction approaching unity. *Journal of Non-Newtonian Fluid Mechanics*, 25:61–92, 1987.

[84] A M Kraynik and M G Hansen. Foam rheology : A model of viscous phenomena. *Journal of Rheology*, 31(0):175–205, 1987.

[85] K J Mysels, K Shinoda, and S Frankel. *Soap Films, Studies of their Thinning and a Bibliography.* Pergamon, 1959.

[86] L W Schwartz and H M Princen. A theory of extensional viscosity for flowing foams and concentrated emulsions. *Journal of Colloid and Interface Science*, 118(1):201–211, 1986.

[120] E N Gilbert. Random subdivisions of space into crystals. *Annals of Mathematical Statistics*, 33:958, 1962.

[121] T Kiang. Random fragmentation in two and three dimensions. *Zeitschrift fur Astrophysik*, 64:433–439, 1966.

[122] D Weaire. *Metallurgica*, 7:157, 1974.

[123] R E Miles. *Mathematics in the Biosciences*, 6:85, 1970.

[124] G Le Caer and J S Ho. The voronoi tessellation generated from eigenvalues of complex random matrices. *Physics A Mathematical and General*, 23:3279–3295, 1990.

[125] S A Khan, C A Schnepper, and R C Armstrong. Foam rheology : III measurement of shear flow properties. *Journal of Rheology*, 32(1):69–92, 1988.

[126] H M Princen. Osmotic pressure of foams and highly concentrated emulsions. 1 theoretical considerations. *Langmuir*, 2:519–524, 1986.

[127] F P Preparata and M I Shamos. *Computational Geometry.* Springer-Verlag, 1990.

[128] D T Lee and B J Schachter. Two algorithms for constructing a delaunay triangulation. *International Journal of Computer and Information Sciences*, 9(3):219–242, 1980.

[129] F Aurenhammer and H Edelsbrunner. An optimal algorithm for constructing the weighted Voronoi diagram in the plane. *Pattern Recognition*, 17(2):251–257, 1983.

[130] F Aurenhammer. Power Diagrams : Properties, algorithms and applications. *SIAM Journal of Computing*, 16(1):78–96, 1987.

[131] P J Green and R Sibson. Computing dirichlet tessellations in the plane. *Computer Journal*, 21(2):168–173, 1978.

[132] M Tanemura, T Ogawa, and N Ogita. A new algorithm for three-dimensional Voronoi tesselation. *Journal of Computational Physics*, 51:191–207, 1983.

[133] R Riedinger, M Habar, P Oelhafen, and Güntherodt. About the Delaunay-Voronoi tesselation. *Journal of Computational Physics*, 74:61–72, 1988.

[134] M J McCullagh and C G Ross. Delaunay triangulation of a random data set for isarithmic mapping. *Cartographic Journal*, 12(2):93–99, 1980.

[135] A Bowyer. Computing dirichlet tessellations. *Computer Journal*, 24(2):162–166, 1981.

[136] D F Watson. Computing the n-dimensional delaunay tessellation with application to voronoi polytopes. *Computer Journal*, 24(2):167–172, 1981.

[103] F Bolton and D Weaire. The effects of Plateau borders in the two-dimensional soap froth. ii general simulation and analysis of rigidity loss transition. *Philosophical Magazine B*, 65(3):473–487, 1992.

[104] S Hutzler and D Weaire. The osmotic pressure of a two-dimensional disordered foam. *Journal of Physics Condensed Matter*, 7:L657–L662, 1995.

[105] S Feng and M F Thorpe. *Physical Review B*, 31:276, 1985.

[106] E J Garboczi and M F Thorpe. *Physical Review B*, 31:7276, 1985.

[107] C A Bennett. *Journal of Applied Physics*, 43:2727, 1972.

[108] D Weaire, N Pittet, S Hutzler, and D Pardal. *Physical Review Letters*, 71(3):2670, 1993.

[109] G Verbist and D Weaire. *Europhysics Letters*, 26(8):631–634, 1994.

[110] M A Fortes and S Coughlan. Simple model of foam drainage. *Journal of Applied Physics*, 76(7):4029–4035, 1994.

[111] S Kumar and S K Kurtz. Properties of a two-dimensional Poisson-Voronoi tesselation : A Monte-Carlo study. *Materials Characterization*, 31:55–68, 1993.

[112] S Kumar, S K Kurtz, and D Weaire. Average number of sides for the neighbours in a Poisson-Voronoi tesselation. *Philosophical Magazine B*, 69(3):431–435, 1994.

[113] K B Lauritsen, C Moukarzel, and H J Herrmann. Statistical laws and mechanics of Voronoi random lattices. *Journal de Physique I*, 3:1941–1951, 1993.

[114] T Ogawa. Problems in a digital description of atoms and some other geometrical topics in physics. In F Yonezawa and T Ninomiya, editors, *Topological Disorder in Condensed Matter*, page 60. Springer, 1983.

[115] H Telley. *Modelisation et Simulation Bidimensionelle de la Croissance des Polycristaux.* PhD thesis, EFPL, Lausanne, 1989.

[116] F Righetti. *Modelisation 3-D d'Amas Polycrystallins et Methodologie d'Analyse de leurs Images Microscopiques.* PhD thesis, EPFL, Lausanne, 1992.

[117] I Yekutieli. *Figures de Souffle et Structures Cellulaires : Aspects Géométriques de la Croissance.* PhD thesis, Paris, 1992.

[118] D Weaire, J P Kermode, and J Wejchert. On the distribution of cell areas in a Voronoi network. *Philosophical Magazine Letters*, 53(5):L101–L105, 1986.

[119] J L Meijering. Interface area, edge length, and number of vertices in crystal aggregates with random nucleations. *Philips Research Reports*, 8:270–290, 1953.

[137] S W Sloan. A fast algorithm for constructing delaunay triangulations in the plane. *Advanced Engineering Software*, 9(1):34–55, 1987.

[138] C L Lawson. Software for C^1 surface interpolation. In J Rice, editor, *Mathematical Software III*, pages 161–194. Academic Press, 1977.

[139] T Kao, D Mount, and A Saalfeld. Dynamic maintenance of delaunay triangulations. *Information Proc. Letters*, 34:219–233, 1990.

[140] L Guibas, D Knuth, and M Sharir. Randomized incremental construction of delaunay and voronoi diagrams. In *Proceedings of ICALP*. 1990.

[141] V J D Tsai. Fast topological construction of Delaunay triangulations and Voronoi diagrams. *Computers and Geosciences*, 19(10):1463–1474, 1993.

[142] N N Medvedev. The algorithm for three-dimensional Voronoi polyhedra. *Journal of Computational Physics*, 67:223–229, 1986.

[143] J H Friedman, J L Bentley, and R A Finkel. An algorithm for finding best matches in logarithmic expected time. *ACM Transactions on Mathematical Software*, 3(3):209–226, 1977.

[144] D-Z Du. Voronoi diagrams and delaunay triangulations. In D-Z Du and F Hwang, editors, *Computing in Euclidean Geometry*. Academic Press, 1992.

[145] V J D Tsai and A P Vonderohe. A generalized algorithm for the construction of Delaunay triangulations in Euclidean n-space. *Computers and Geosciences*.

[146] L D Landau and E M Lifshitz. *Fluid Mechanics*. Pergamon Press, 1959.

[147] G K Batchelor. *Journal of Fluid Mechanics*, 41:545–570, 1970.